Measurement and Application of Topological Information in Physically and Virtually Segmented Scintillators

by

Andrew Wilhelm

A dissertation submitted in partial fulfillment
of the requirements for the degree of
Doctor of Philosophy
(Nuclear Engineering and Radiological Sciences)
in The University of Michigan
2024

Doctoral Committee:

Professor Igor Jovanovic, Chair
Professor Doug Cowen
Professor Bjoern Penning
Professor Sara Pozzi

Andrew Wilhelm

andhelm@umich.edu

ORCID iD: 0000-0002-0664-0477

For my family.

ACKNOWLEDGEMENTS

As with any large undertaking, this work was supported by a wonderful network of colleagues, friends, mentors, and family.

I'm grateful to my committee for their excellent advice and probing questions, and for my ANSG friends, past and present, who were willing to pay attention to my presentations during group meetings and point out my blunders. And especially my advisor, Professor Igor Jovanovic, who contributed immeasurably to all the work in this thesis, and more importantly, to my development as a scientist, engineer, and academic. The patience, generosity, and exceptional engagement you provide your students are traits I hope to emulate in the future.

I'm grateful for my colleagues at the various national laboratories and collaborations, especially Minfang Yeh and Richard Rosero at Brookhaven, Jason Nattress and Mike Febbraro at Oak Ridge, Doug Cowen, Anatael Cabrera, Jeff Hartnell, and Mark Chen from LiquidO, and all of Young CLOUD. And for Garrett Wendel, who patiently explained to me how HITMAN works no fewer than four dozen times.

I'm grateful for the support I received from the team at West Point, including the NSERC (especially LTC Nick Duncan, MAJ Dave Fobar, and MAJ Josh Frey), and the whole PANE crew. And to all my mentors, past and present, of various specialties: MG Scott Naumann, COL James Modlin, COL John Hartke, and COL Pete Chapman.

I'm grateful to my kids, for always being patient when I sat in my home office

and muttered angrily at an indecipherable feature on a plot for hours on a Saturday. And to my wife, who in addition to being an absolute rock not just during the past three years, but for the past 19, also came up with the idea to use regular old milk for the experiments in Chapter IV. Thanks, honey!

TABLE OF CONTENTS

DEDICATION . . . . . **ii**

ACKNOWLEDGEMENTS . . . . . **iii**

LIST OF FIGURES . . . . . **viii**

LIST OF TABLES . . . . . **xvi**

LIST OF ABBREVIATIONS . . . . . **xvii**

ABSTRACT . . . . . **xviii**

CHAPTER

I. Introduction 1

1.1 Fundamentals of radiation detection 1
1.2 Detectors based on scintillation 2
1.2.1 Applications of event topological information in scintillation detectors 3
1.2.1.1 Imaging 3
1.2.1.2 Particle type identification 5
1.2.1.3 Charged particle tracking 6
1.2.2 Reconstruction of interaction position in traditional scintillators . . 6
1.2.2.1 Unsegmented scintillator detector designs 7
1.2.2.2 Segmented scintillator detector designs 8
1.2.2.3 Virtual segmentation (opaque scintillators) 10
1.3 Research question and organization of following chapters 11

II. Gamma-Ray Spectroscopy Using Angular Distribution of Compton Scattering 13

2.1 Introduction 14
2.2 Theory 15
2.2.1 Klein-Nishina differential cross-section 15
2.2.2 Detector array response 17
2.2.3 Solution algorithms 17
2.3 Simulation 18
2.3.1 Response matrix 18
2.4 Experiment 19
2.4.1 Array design 19
2.4.2 Experimental setup 21
2.4.3 Data 22
2.5 Results 24
2.5.1 Monoenergetic experimental spectrum 24

2.5.1.1 MLEM Reconstruction . . . 25
2.5.1.2 ANN Reconstruction . . . 26
2.5.2 ICS spectral reconstruction from synthetic data . . . 27
2.6 Conclusion . . . 31
2.7 Future Work . . . 31

III. Light Transport and Collection in Highly Scattering Media . . . 33

3.1 Light transport in turbid media . . . 33
3.1.1 Scattering . . . 34
3.1.2 Wavelength-shifters in the bulk media . . . 39
3.1.3 Bulk absorption . . . 40
3.1.4 Reflection . . . 41
3.2 Light collection into WLS fibers from a liquid scintillator . . . 42
3.2.1 Reflection at the fiber-scintillator boundary . . . 42
3.2.2 Absorption and re-emission . . . 43
3.2.3 Light trapping and transport . . . 43
3.3 Readout . . . 47
3.4 Theoretical maximum efficiency . . . 48

IV. Evaluation of Light Collection From Highly Scattering Media Using Wavelength-Shifting Fibers . . . 50

4.1 Introduction . . . 50
4.2 Experiment . . . 52
4.2.1 Apparatus . . . 53
4.2.1.1 Calibration . . . 57
4.2.2 Results . . . 57
4.3 Modeling . . . 61
4.3.1 Monte Carlo . . . 61
4.3.2 Diffusion Approximation . . . 68
4.4 Extension of model to low-absorption medium . . . 71
4.5 Conclusion . . . 73

V. Design and Fabrication of an Opaque Scintillator Prototype Based on NoWASH-20 . . . 74

5.1 Design considerations . . . 74
5.1.1 Constraints . . . 74
5.1.2 Geometry . . . 76
5.1.3 Materials . . . 76
5.1.3.1 Fiber . . . 76
5.1.3.2 Body . . . 77
5.1.3.3 Glue . . . 78
5.1.3.4 Scintillation liquids . . . 78
5.2 Assembly . . . 80
5.2.1 Detector body and fibers . . . 80
5.2.2 NoWASH-20 . . . 81
5.2.3 Volume collapse . . . 83
5.3 Gamma-ray response . . . 86
5.3.1 Event building . . . 86
5.3.2 Response with PPO as the sole wavelength-shifter . . . 86
5.3.3 Addition of POPOP . . . 88
5.3.4 Response with PPO and POPOP . . . 89

5.3.4.1 Source localization via event topology 90
5.4 Conclusion 93

VI. Characterization of an Opaque Scintillator Prototype Detector Based on oWbLS 94

6.1 Introduction 94
6.2 Apparatus and material 95
6.2.1 Detector design and construction 96
6.2.2 WLS fibers and MAPMT 96
6.2.3 Opaque water-based liquid scintillator 98
6.2.4 Data acquisition and analysis 100
6.3 Results 100
6.3.1 oWbLS light yield 100
6.3.2 oWbLS absorption and scattering length 102
6.3.3 Gamma-ray response 106
6.3.4 Comparison to simulation 106
6.3.5 Topological reconstruction 108
6.3.5.1 Center of mass 108
6.3.5.2 Machine learning 112
6.3.6 Energy Resolution 121
6.4 Conclusion 123
6.4.1 Discussion 123
6.4.2 Future work 124

VII. Conclusion 126

7.1 Review of objectives 126
7.2 Major results 127
7.3 Future work 128
7.4 Summary 130

BIBLIOGRAPHY **131**

LIST OF FIGURES

Figure

1.1 A sketch of a simple Compton camera for determining the incident direction of gamma rays, from Phillips [11]. If the energy and location of the scattering event (here shown as E_1) and the energy and location of the capture event (E_2) are known, the possible incident direction of the gamma ray is constrained to a cone. . 4

1.2 A sketch of a monolithic plastic scintillator with a photomultiplier tube at each corner from Tang *et al.* [17]. The position of interaction is reconstructed from the relative trigger times of each PMT. 8

1.3 A rendering of the SANDD prototype design from Ref. [20]. All of the component scintillator bars are a ^{6}Li-doped plastic but vary in size and shape. 9

2.1 The Klein-Nishina differential cross-section shapes for photons of various energies scattered off a hydrogen atom. The photon is incident at $\theta = 0$ and the cross-section is measured in m^2. For heavier atoms, the magnitude of the KNDCS changes, but the shape is invariant for a given photon energy. Higher energy photons are much less likely to undergo a high-angle scattering than lower energy photons. 16

2.2 Simulated response matrices of (left) 14 and (right) 500 energy bins for a 14-detector array with 4×10^{10} incident photons in the range of 0–2000 keV. Detector 1 is located at a scattering angle of 12° with respect to the incident direction, and detector 14 is at a scattering angle of 168°, with detectors spaced at 12°. 20

2.3 (left) A schematic of the experimental setup with an EJ-309 scattering target and 14 detector positions for a NaI(Tl) array detector. A photon is scattered from the target detector to detector 3. The source is inside a lead housing to shield the array detectors from direct exposure, and the detectors are shielded to prevent crosstalk. A coincidence is required between the target and a single array detector for the event to be counted. The light output of the array detector was integrated across the entire measurement time to simulate pileup. (right) A photograph of the experimental setup, with the array detector in position 1. 21

2.4 The light output spectrum for the array detector at a scattering angle of 36° as a function of the delay between the trigger in the scattering detector and the target detector. The photopeak of scattered photons can be seen as the area of high density within the integration region at 530 keV. The delay does not represent the time of flight of the scattered photon between detectors, but instead a constant time offset between the channels. The regions used to calculate the background and integrated light output of the array detector are marked in red. 23

2.5 The experimental and simulated integrated light output for a 14-detector array exposed to a scattered beam of monoenergetic 661.7-keV photons from a 62-µCi ^{137}Cs source for 6 hours. 24

2.6 The results of spectral reconstruction using MLEM after 2.5×10^5 iterations with a variety of sizes of response matrices. The true incident spectrum consists of monoenergetic 661.7-keV gamma rays from ^{137}Cs. While the reconstruction of spectral shape is poor, the average energy was within 3% of the true value for 14-250 energy bins and 9% for 500 and 1000 energy bins. 26

2.7 The results of spectral reconstruction using ANNs trained with data constructed using responses matrices of (a) 14, (b) 50, (c) 100, (d) 250, (e) 500, and (f) 1000 energy bins. The true incident spectrum was monoenergetic 661.7 keV photons from ^{137}Cs. The cosine similarities and energy weighted averages are tabulated in Table 2.1. 28

2.8 The results of spectral reconstruction using ANNs trained with simulated ICS pulses. A 1000 energy bin response matrix was used to train the network. ICS pulses were simulated with (a) 10^8 photons (cosine similarity: 0.9749), (b) 5×10^7 photons (cosine similarity: 0.9197) and (c) 10^7 photons (cosine similarity: 0.9537). The error bars are the standard deviation from the reconstruction of five pulses. . . 30

3.1 Example photon paths through a bulk medium with a reduced scattering length of 5 mm and an absorption length of 16 cm. The left panel shows the propagation of five photons for the case in which the anisotropy parameter $g = 0.9$, and the right panel shows the case in which $g = 0.1$. The lower anisotropy results in less frequent, but higher-angle scatters. The vertical red lines in each panel are WLS fibers at a 2 cm pitch. 36

3.2 The distributions of photoelectrons generated by photon captures in the WLS fiber nearest to the origin of the photons for three different anisotropy factors. The reduced scattering length in each case is the same. For each event, 1000 photons were generated isotropically 1 mm from the fiber. 37

3.3 The total signal across all channels for photons transported through a highly scattering liquid with the same reduced scattering length, but different anisotropy factors. As expected, the distributions are very similar, demonstrating that the reduced scattering coefficient is an adequate approximation in modeling photon propagation for this context. 38

3.4 A sketch of reflection and refraction of a ray of light according to Snell's Law. The left panel shows a ray of light partially refracting from a medium with a higher index of refraction to a medium with a lower index of refraction. The right panel shows light incident on medium 2 at an angle greater than the critical angle; the light is reflected and not refracted. 44

3.5 A sketch of the geometry of the path of a photon that originates on the optical axis of a fiber. The green region represents the fractional solid angle that results in total internal reflection. 45

4.1 A sketch of the experimental apparatus. The dashed interfaces are electrical, and the solid ones are optical. The data acquisition system is triggered by the pulse generator during calibration and by the laser controller during experiments with laser pulses. 54

4.2 The experimental apparatus inside a dark box. The yellow-jacketed fiber carries the light from the pulsed laser to the center of the fiber array, which is submerged in 7500 ml of opaque liquid. The fibers emerge from the liquid and terminate at individual pixels of the MAPMT. 54

4.3 Views of the fiber holder with WLS fibers from (a) bottom and (c) side. The end of the laser-coupled single-mode fiber is shown in (b). A 0.2 mm diameter nylon monofilament is suspended vertically in the center of the array. The single-mode fiber (ThorLabs SM300) is secured to the nylon monofilament by a small knot, made of more nylon monofilament, to maintain the central positioning of the light source. 56

4.4 The pulse integral spectra from an example channel of the MAPMT during calibration are shown on a semi-log scale. A constant pedestal charge of 1024 ADC channels was added to aid the fitting process. (a) is the background, while (b)–(d) shows the response to increasing light intensity from a pulsed LED. In each plot, the red line is the overall fit, while the other colors show the contributions from a single photoelectron (green), two photoelectrons (blue), *etc* (see text for details). The value μ shown in each plot is the average photoelectrons per pulse, which was a fitted parameter. 58

4.5 Experimental data from the same channel as in Fig. 4.4, fit with the parameters found during calibration. The red line is the overall fit, while the other colors show the contributions from events in which an increasing number of photoelectrons was produced. While the events of up to 12 photoelectrons are included in the fitting function, only 8 are shown for clarity. The parameter μ represents the average number of photoelectrons per pulse. 58

4.6 Photoelectrons detected per pulse from photons collected in a WLS fiber closest to the location of light injection. The first iteration of the experiment was done with 100% cow skim milk, and then the liquid was replaced with distilled water to dilute the milk. The uncertainty in the reconstructed number of photoelectrons per pulse is derived from the uncertainty of the fitting algorithm described in Sec. 4.2.1.1. . 60

4.7 Photoelectrons per pulse from photons collected in WLS fibers at various distances from the light source for a variety of dilutions of commercial, 2% fat cow milk. Each pulse of light contained 17,900±900 photons. 61

4.8 Kuraray Y-11 WLS absorption (purple squares) and emission (green circles) spectra used in the Geant4 model. WLS absorption results in a new optical photon with a wavelength sampled from the emission distribution and a randomized direction. . . 62

4.9 Quantum efficiency (black circles) of the Hamamatsu H12700A and the bulk absorption length of the Kuraray Y-11 fiber (red squares) used in the Geant4 model. Bulk absorption is a separate process from WLS absorption in Geant4 and cannot result in the emission of a new optical photon. The dip in the absorption length around 610 nm is due to a resonance in the absorption cross-section characteristic to WLS fibers with a polystyrene core [89] 62

4.10 A flowchart of the parameter search process to determine the optical parameters of pure milk. 65

4.11 The total WSSE values for combinations of scattering and absorption parameters for simulation and experimental data. The total WSSE is the individual WSSEs from the 25%, 20%, 10%, and 5% dilutions of 2% milkfat commercial milk datasets, added in quadrature. The minimum error was 31.7, at a reduced scattering length of 0.75 mm and an absorption length of 8 mm. 66

4.12 Comparison of simulated and experimental results for (a) 25% milk, (b) 20% milk, (c) 10% milk, and (d) 5% milk. All simulated values agree with the experiment within uncertainty. The optical parameters used for pure milk were optimized as shown in Fig. 4.11. Note that the vertical scale for (a) and (b) differs from the scale for (c) and (d). 67

4.13 The comparison of simulated and experimental results for 15% milk dilution. The optical parameters for milk used were the same as shown in Fig. 4.12. 68

4.14 Photon absorption probabilities for a square grid array of WLS fibers with a fiber pitch of 15 mm simulated using the diffusion approximation and Monte Carlo. The inset shows a visualization of the geometry in Geant4. The two simulation methods perform within 15% of each other at each fiber. 71

4.15 Simulated efficiency of light collection possible in an opaque liquid with a 5 m absorption length and a 0.5 mm reduced scattering length. The plot shows the number of photoelectrons detected per photon injected into the system and includes losses in transport in the bulk medium, collection in the WLS fiber, and conversion at the photocathode. 72

5.1 A CAD rendering of the final cube design. The capacity is 1 L, and the fiber pitch is 2 cm. The fibers are shown as green lines. 77

5.2 An image taken through a jeweler's glass of the end of a WLS fiber before (left) and after (right) polishing with a series of fine grit sandpaper. All fibers were similarly prepared and inspected before loading into the prototype detector body. 80

5.3 An image of the fiber-MAPMT interface. The fibers are held in place within the interface with silicon o-rings and are coupled to the face of the MAPMT with optical grease. Both ends of each fiber are routed to the same MAPMT pixel. . . . 81

5.4 The detector body prototype (a) and installation of fibers (b-d). The fibers were 1 m long and arranged such that the bending radius was minimized when coupled to the MAPMT interface (d). 82

5.5 A schematic of the experimental apparatus, including the 1 L aluminum cube prototype. The dark box, calibration LED, MAPMT, and readout electronics are the same as were described in Ch. IV. 82

5.6 An image of the NoWASH-20 melting process. A 20% weight fraction of paraffin wax was added to a mixture of LAB and 3 g/L PPO, then slowly heated to 60° C on a hotplate. The melting process took about 15 minutes, after which the liquid appeared completely clear. 83

5.7 The change in appearance of the NoWASH-20 scintillating liquid as it cools. The temperatures were (a) 49° C, (b) 34° C, (c) 32° C, (d) 31° C, (e) 30° C, and (f) 19° C, after cooling to room temperature overnight. As can be seen in panel (f), the reduction in density as the liquid-cooled resulted in a small depression in the center of the surface. 84

5.8 An image of the volume collapse on top of the detector. The left panel shows the volume collapse of the first iteration of the prototype, in which the liquid was poured at approximately 60° C. The center panel shows a close-up of the volume collapse in this iteration. The top layer of fibers can be seen, indicating that the light collection efficiency of these fibers is impacted by the depression. The right panel shows the reduced volume collapse from allowing the liquid to cool to approximately 41° C before pouring. 85

5.9 The measured integral gamma-ray spectra from the decays of ^{137}Cs and ^{60}Co. As expected, the higher energy gamma rays from ^{60}Co have a higher spectral endpoint, indicating that they created more light in the volume. However, no Compton features are readily identifiable. 87

5.10 The emission and absorption spectrum for several components in the NoWASH-20 blend. The PPO and POPOP emission and absorption spectra are taken from Ref [101], and the WLS absorption spectrum is for Kuraray Y-11(200) fiber and is taken from Ref. [69]. 88

5.11 The process of adding POPOP to NoWASH-20. (a) The POPOP can be seen as undissolved flakes in the heated (60° C) NoWASH-20. (b) After 90 minutes of vigorous stirring, the POPOP was fully dissolved. (c) The appearance of the NoWASH-20 under UV illumination before and (d) after the addition of POPOP. The color has changed from violet to blue. (e) The NoWASH-20 with POPOP under UV illumination after being cooling in the cube to 33° C and (f) 18° C. The change in opacity is apparent. 89

5.12 The measured emission spectrum of NoWASH-20 after the addition of 10 mg/L of the wavelength shifter POPOP. The peak absorption wavelength of the Y-11 fibers is shown as a vertical red line. 90

5.13 The measured integral gamma-ray spectra from the decays of ^{137}Cs and ^{60}Co before and after the addition of POPOP to the NoWASH-20. The first 1.5×10^5 events are shown for each dataset. As expected, the addition of POPOP resulted in a larger integral signal for both radioisotopes. However, Compton features are still difficult to discern, probably due to the high opacity of the NoWASH-20. 91

5.14 A demonstration of source localization from average event topology. The top row of histograms corresponds to a 100 sec. measurement of a 1 µCi ^{60}Co gamma-ray position 1 (as annotated on the sketch to the right), and the bottom row of histograms corresponds to the measurement with the source at position 2. The cells indicate the normalized number of photoelectrons generated in that channel, and 2D Gaussian fits are included as eye guides. The approximate location of the source in the xy plane is readily discernible in each case. 92

6.1 (a) Detector body made of VeroWhite with 32 WLS fibers glued in place. The fibers terminate at the MAPMT interface, shown from the front in (b). (c) Exterior of the dark box, with a pulsed LED mounted on top for calibration. The readout electronics are on the left. (d) Interior of the dark box with the detector mounted to the MAPMT. The top of the detector body is closed with a lid, also made of VeroWhite. 97

6.2 From left to right: oWbLS1, oWbLS2, oWbLS3, and NoWASH-20. oWbLS1 has the longest scattering length of the three oWbLS samples and appears relatively transparent, and oWbLS2 has the shortest scattering length. The waxy consistency of NoWASH-20 at room temperature (∼18° C) can be observed. 99

6.3 A flowchart of the data acquisition and analysis process. The primary input for a data run is the s.p.e response for each channel, and the output is a list of events, each of which contains pulses from multiple channels that have been correlated by their timestamps and calibrated to be in units of p.e. 101

6.4 Relationship between the number of triggered channels and total event signal for the three formulations of oWbLS. The data shown is from the ^{60}Co datasets. Linear fits are shown to guide the eye and highlight the difference in confinement for scintillation photons in each liquid. 103

6.5 An image of the measurement described in Sec. 6.3.2. A fiber-coupled laser is used to inject photons into the center of the detector, and the response for each channel is measured. The laser fiber is held by an apparatus mounted on a linear translation stage so that the measurement can be repeated at various distances from the center of the detector. 103

6.6 A comparison of the average signal in each channel for laser pulses with 20000±2000 photons at a location near the center of the detector. A genetic algorithm was used to find optimal values for six unknown parameters. 105

6.7 Response to gamma rays from three radioisotopes for (a) oWbLS1, (b) oWbLS2, and (c) oWbLS3. Among these, oWbLS1 had the longest scattering length, leading to the sharpest Compton features, while oWbLS2, with the shortest scattering length, provided optimal light collection. (d) Response of the three formulations of oWbLS to gamma rays from ^{60}Co for ease of comparison. It is evident that the light collection efficiency increases as the scattering length decreases. The response of NoWASH-20 is shown for reference; however, a different detector body and set of fibers were used to make this measurement, making it a point of interest rather than a direct comparison. 107

6.8 The comparison of experimental and simulated detector response for gamma rays from three radioisotopes. The simulation results are shown as a shaded region. The simulation parameters are those described in Table 6.2. More details about the simulation methodology are available in Ref. [74]. 108

6.9 Mapping of CoM and true positions of events for the (left) x and y dimensions and (right) the z dimension. The histogram shows true and reconstructed positions for 3×10^6 simulated events that varied in the range of 5000–30000 photons/pulse. The black dots show the centroids of Gaussian distributions fit to slices of the histogram. The red line shows the polynomial fit (9^{th} order for x and y, and 3^{rd} order for z) to the Gaussian centroids. 110

6.10 Distribution of position reconstruction errors from the CoM method in each dimension for pulses of approximately 20000 photons/pulse at a nominal position of $(0, 0, 0)$. As expected, the distributions of errors in x and y have similar widths, and the distribution of errors in z is narrower due to the increased fiber density in this direction. 111

6.11 Distribution of position reconstruction errors using the CoM method for a point-like event comprising approximately 20000 initial photons near the center of the detector, with a mean of 4.35 mm and a standard deviation of 2.15 mm. 111

6.12 Position reconstruction errors for the detector positions listed in Table 6.3. The large pulses had an intensity of 20000 ± 2000 photons/pulse, and the small pulses were 10000 ± 1000 photons/pulse. The average reconstruction error (shown as dotted horizontal lines) for the large pulses was 4.4 mm and for the small pulses was 7.4 mm. The horizontal error bars represent the uncertainty in offset from the center of the detector, and the vertical error bars show the standard deviation of the reconstruction position errors. 112

6.13 The reconstruction results from HITMAN. The reconstructions are of 10^5 spatially homogenous simulated events with 20000 photons using the MLE method. The top left panel shows the reconstructions in the x dimension, the top right shows the y dimension, and the bottom left shows the z dimension. A perfect set of reconstructions would show a horizontal line, corresponding to a perfect correlation between the true and reconstructed values. The bottom right panel shows reconstructions of intensity. 115

6.14 Additional reconstruction results from HITMAN. The reconstructions are of 10^5 spatially homogenous simulated events with 20000 photons using the MMSE. Similarly to Fig. 6.13, the top left panel shows the reconstructions in the x dimension, the top right shows the y dimension, and the bottom left shows the z dimension. The bottom right panel shows reconstructions of intensity. 116

6.15 A comparison of the reconstruction quality within the fiducial region of the detector using simulated events comprising 20000 photons. The top left panel shows the x direction, the top right panel shows y, and the bottom left shows z. The bottom right panel shows the total reconstruction error. The mean reconstruction error of the corrected CoM method was 5.5 ± 2.9 mm whereas the HITMAN MLE method had a mean error of 4.9 ± 3.3 mm. 118

6.16 Machine learning (HITMAN) and CoM reconstructions on experimental data from pulses of 20000 ± 2000 photons. The nominal true event positions were $(0, 0, 0)$ mm, with a 5 mm uncertainty in each direction. The top left panel shows the x direction, the top right panel shows y, and the bottom left shows z. The bottom right panel shows the total reconstruction error. The mean error for HITMAN was 4.1 ± 2.3 mm and 4.3 ± 2.1 mm for the corrected CoM method. The machine learning algorithm outperformed the CoM analysis. 119

6.17 Machine learning (HITMAN) and CoM reconstructions on experimental data from pulses of 20000±2000 photons. The nominal true event positions were $(0, -20, 0)$ mm, with a 5 mm uncertainty in each direction. The top left panel shows the x direction, the top right panel shows y, and the bottom left shows z. The bottom right panel shows the total reconstruction error. The mean error for HITMAN was 5.0±4.1 mm and 3.9 ± 1.9 mm for the corrected CoM method. The machine learning algorithm failed to outperform the CoM analysis, primarily due to the bimodality of reconstructions in the y direction. 120

6.18 (Left) Distribution of p.e. per pulse for light injected into the center of the detector. Each distribution is fit with a Gaussian, shown as a dotted line. (Right) Energy resolution as a function of distance from the center of the detector. The energy resolution values are calculated from the Gaussian fitting of the individual total signal distributions. The mean energy resolution values for large (20000 ± 2000 photons/pulse) and small (10000±1000 photons/pulse) pulses are shown as a dotted line. 122

LIST OF TABLES

Table

2.1 The performance of MLEM and ANN reconstruction of the spectrum of a monoenergetic ^{137}Cs source. 25

2.2 The ANN settings used to reconstruct the monoenergetic experimental spectrum. . 27

2.3 The ANN settings used to reconstruct the ICS pulse spectra. 29

4.1 The material properties used to construct the Geant4 model. 61

6.1 Measured light yields of opaque scintillation liquids used in experiments 102

6.2 The parameters found by genetic algorithm and comparison to simulation for oWbLS3. The experimental dataset was generated by pulsed light from a 407 nm fiber-coupled laser near the center of the detector. 104

6.3 Positions used for light injection experiments to assess variations in reconstruction precision. 112

LIST OF ABBREVIATIONS

ANN Artificial neural network

bis-MSB 1,4-Bis(2-methylstyryl)benzene

CAS Chemical abstracts service

CoMPASS CAEN multi-parameter spectroscopy software

DAQ Data acquisition system

DPP-PSD Digital pulse-processing, pulse-shape discrimination

HDPE High-density polyethylene

ICS Inverse Compton scattering

KNDCS Klein-Nishina differential cross section

MAPMT Multi-anode photomultiplier tube

MLEM Maximum-likelihood expectation-maximization

NoWASH New opaque Wax Scintillator, Heidelberg

oWbLS Opaque water-based liquid scintillator

PMT Photomultiplier tube

POPOP 1,4-bis(5-phenyloxazol-2-yl)benzene

PPO 2,5-Diphenyloxazole

SiPM Silicon photomultiplier

SNR Signal-to-noise ratio

WbLS Water-based liquid scintillator

WLS Wavelength-shifting

WSSE Weighted sum of squared errors

ABSTRACT

Spatial information about the interaction of radiation and matter within a scintillation detector, also known as event topology, can be obtained from various detector designs. This work explores a new application of event topology for spectroscopy in extreme pileup environments, and a novel technique for measuring event topology through stochastic confinement of scintillation photons.

The determination of the spectral characteristics of a polyenergetic beam of radiation traditionally depends upon resolving the interactions of individual particles, and then correlating features of the resulting distribution of energy deposition to the energy of the incident particles. In environments in which many particles arrive at the detector simultaneously, it can be very difficult to discern the interactions of individual particles. A study detailing a new technique to address this problem is presented, wherein an incident beam of gamma rays is first Compton scattered, and then a physically segmented scintillation detector system is used to measure the topology of scattered gamma rays. The distribution of scattered gamma rays carries information about the incident beam, from which the spectral characteristics can be reconstructed. This technique could be applied to characterize laser-driven inverse-Compton scattering sources, which produce a short but intense burst of collimated, quasi-monoenergetic photons.

In a typical scintillation detector, the scintillation light may reflect many times within the volume before being collected and converted to an electronic signal, usu-

ally with a single photosensor. A consequence of this is that the detailed location of interaction is often difficult to reconstruct. Measuring the event topology in scintillation detectors can be accomplished by physically segmenting the volume into voxels, or by recording the spatial and/or temporal distribution of light arriving at multiple photosensors surrounding an un-voxelized scintillator volume. The first method generally requires many channels and can be difficult to fabricate, while the second method can be inefficient and suffer from poor spatial resolution. This thesis investigates a new method for measuring event topology based on opaque scintillators. In opaque scintillation detectors, virtual voxelization can be achieved by repeatedly scattering the scintillation photons, such that they are effectively confined to a small lightball around their origin. Then the photons can be collected by a lattice of wavelength-shifting fibers. The theory and simulation of light transport and collection in such a system are presented, and an experiment is described that measured the absolute efficiency of light collection from an opaque liquid to validate the simulation. Two prototypes are described and characterized, based on the wax-based opaque scintillator and the opaque water-based liquid scintillator. The key result is the demonstration of reconstruction of the position of point-like events with a precision of 4.4 mm, corresponding to approximately 25% of the fiber spacing. The resulting fine voxelization could benefit applications that require topological reconstruction and scaling to large volumes, including antineutrino detection, gamma-ray, neutron, and muon imaging, and positron-emission tomography.

CHAPTER I

Introduction

This chapter lays the groundwork for the research questions explored in this thesis. Initially, it explains the operating principles of scintillation detectors, highlighting how many traditional designs fail to capture the spatial distribution of energy deposited by interacting particles. Subsequently, it delves into the potential applications of this topological data and examines existing technologies that effectively measure or reconstruct it. Finally, it outlines the major themes of this study and the structure of the subsequent chapters.

1.1 Fundamentals of radiation detection

The detection and measurement of ionizing radiation has many applications, from healthcare [1] and the nuclear power industry [2] to astronomy [3]. The detection of gamma rays and neutrons is of particular interest to defense nonproliferation, as they comprise important signals from the special nuclear material (SNM) necessary to construct nuclear weapons [4].

The detection of radiation requires an interaction between the incident particle and the detector. The nature of this interaction can vary by the type and energy of incident radiation and the composition of the detector, but in all cases – for the interaction to be detectable – there must be an energy deposition, which then must

be converted to a measurable signal. One such method is to construct a detector from material that can convert the energy deposited by the incident radiation to visible light. These detectors are referred to as scintillators.

It should be mentioned that a similar but distinct type of detector relies on the generation of light by a different mechanism: the Cherenkov effect. Charged particles emit Cherenkov light when they have speeds greater than the speed of light in the medium in which they are traveling. This can occur, for instance, for a Compton electron following a high-energy gamma-ray scatter in water. This is the origin of the famous blue glow in the cores of nuclear reactors. Cherenkov detectors have several useful properties but are not discussed further in this thesis.

1.2 Detectors based on scintillation

The idea of using scintillation for radiation detection dates back at least to Röntgen's discovery in 1895, in which he surmised the existence of X rays by observing the scintillation light on a screen composed of barium platinocyanide [5].

In a scintillation detector, the energy deposited in the interaction causes material excitation, which then de-excites via the emission of light, usually in the UV or visible range. The amount of light emitted for a given amount of energy deposited is called the "light yield" of the detector and is usually quoted in units of photons/MeV of energy deposited. The emission is generally isotropic. The scintillation light is then collected by a photosensor, *e.g.*, a photomultiplier tube (PMT) or silicon photomultiplier (SiPM). Radiation detectors based on scintillation are normally designed to be as transparent as possible to maximize light collection at the photosensor. A scintillation photon may be reflected inside the detector volume several times before it is collected. In other words, the design of traditional scintillation detectors aims

for all photons, regardless of their position of origin, to have an equal chance of being read out by the photosensor. A downside of this technique is that the information about the location of energy deposition of the incident radiation is often obscured or lost entirely.

1.2.1 Applications of event topological information in scintillation detectors

Spatial information on how an incident particle deposits energy in a detector volume is known as event topology. Once determined, this information is useful in a variety of ways.

1.2.1.1 Imaging

Perhaps the most common application of topological information in radiation detection is source localization and imaging. The physics applied depends on the nature of the incident particle.

If a detector or detector array is sufficiently large (on the order of a mean free path of the incident radiation), the self-shielding effect of the detector material will cause more events to occur on the side of the detector facing the source. From this self-shielding or occlusion effect, crude source localization can be achieved [6].

A related technique uses a passive, absorbing mask to project an image onto the detector or array that depends on the angular position of the source. This technique can range in complexity from a pinhole camera [7], to Anger cameras [8] and coded apertures [9].

For gamma-ray detection, a more sophisticated technique is known as the Compton camera. When a high-energy photon undergoes a Compton scattering event, the angle of scatter depends on the incident direction, the initial energy, and the deposited energy. If the photon is detected again at another location, possible di-

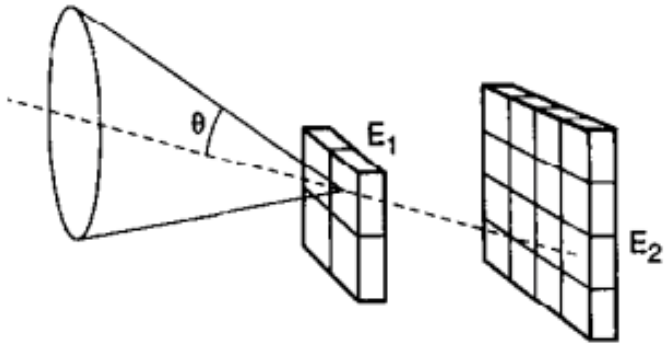

Figure 1.1: A sketch of a simple Compton camera for determining the incident direction of gamma rays, from Phillips [11]. If the energy and location of the scattering event (here shown as E_1) and the energy and location of the capture event (E_2) are known, the possible incident direction of the gamma ray is constrained to a cone.

rections of the original photon are constrained to a cone [10]. Figure 1.1 shows a simple illustration of this technique. Overlapping multiple Compton cones yields a most probable source direction (assuming a point source). The ultimate resolution of such a system, as well as the convergence speed, depends upon the energy and spatial resolution of the measurement of each interaction. A neutron scatter camera operates on a different but related principle. The energy of a fast neutron is a function of its speed, so if a neutron interacts twice in a detector system, the time difference along with the distance traveled between the two events can be related to the energy of the scattered neutron. The brightness of the first event can be related to the energy deposited in that interaction, with the sum of the two equal to the energy of the incident neutron [12]. The energy deposited in the first scatter, along with the incident energy of the neutron, can be used to calculate the scattering angle. Similar to the Compton camera, the possible vectors that point back to the source from the detector are once again constrained to a cone. The incident direction of a neutron that interacts only once in the detector system cannot be reconstructed in

this way, and likewise, the incident direction of neutrons that scatter many times in the detector system may be difficult to reconstruct in practice. Detectors of this type rely on fast timing to achieve good energy resolution.

1.2.1.2 Particle type identification

Particle-type identification in scintillation detectors can be achieved in a variety of ways, depending on the specific particle or particles that must be identified or discriminated between. For instance, a common method of discriminating between neutrons and gamma rays in scintillation detectors uses the difference in pulse shape arising from either the recoil proton in a neutron scatter or the Compton electron in a gamma-ray scatter event [13]. A proton deposits energy over a shorter track than an electron, but in either case molecules can be excited into singlet or triplet states. These two states often have different decay times, generally with the triplet states taking longer to decay. After the singlet states have decayed away, the molecules excited into triplet states can interact with one another, sometimes resulting in a molecule that occupies a singlet state. That molecule then decays to the ground state, emitting a scintillation photon in a process known as delayed fluorescence [14]. The interaction of two molecules excited to the triplet state depends, among other factors, on the volumetric density of such molecules. The density is higher along the track of an energetic proton than that of an energetic electron because of the higher density of energy deposition. The net effect is that the tail of a voltage pulse arising from a neutron scatter is contains more signal than that of a gamma ray scatter. This method does not depend on the event topology.

An alternative method is to use the event topology to differentiate between interactions. Using the example above, if the position of origin of all scintillation photons is known, the neutron event will appear approximately point-like, but the gamma-ray

scatter event will look like a track. For gamma-ray energies $\lesssim$MeV in non-gaseous detectors, the track of an electron is often shorter than the position resolution of the detector, and neutron-gamma discrimination using this technique becomes difficult. However, discrimination between e^- and e^+ has been demonstrated using this method in the JUNO experiment [15] to reject background events.

1.2.1.3 Charged particle tracking

Charged particles deposit energy in scintillation detectors along the path they travel. In the case of very energetic charged particles, the tracks can be long and can contain information about the particle type or direction of travel.

An example of the usefulness of this information is in muon scattering tomography. Muons originating from cosmic rays travel at speeds close to the speed of light and are ideal for some tomographic applications because they are naturally abundant, highly penetrating, and unlike neutrinos, always deposit energy when passing through matter. Muon scattering tomography relies on the measurement of the angular deviation of a muon as it passes through an object. In order to determine this deviation, the initial and final trajectories of the muon must be known, which requires tracking. A typical solution is to use four planar scintillation detectors (two above the object and two below), which together provide the necessary information. Position resolution for detector arrays of this type is generally on the order of several mm to several cm [16].

1.2.2 Reconstruction of interaction position in traditional scintillators

The previous section described various applications of knowledge of event topology in scintillation detectors but did not detail methods for obtaining that information. There are several methods to reconstruct the position of the interaction in a scin-

tillation detector, but I will categorize them broadly into unsegmented, physically segmented, and virtually segmented designs.

1.2.2.1 Unsegmented scintillator detector designs

Reconstruction of event topology in unsegmented detectors generally relies upon placing multiple, sometimes many, photosensors around the boundary of the scintillation volume, and then using differences between the time and intensity of resulting signals to deduce the nature of the interaction.

Tang *et al.* demonstrated position reconstruction of muon interactions in a 760 mm × 760 mm × 30 mm EJ-200 plastic scintillation panel [17], a schematic of which is shown in Fig. 1.2. The position reconstruction depends on the difference in travel time for the scintillation photons to reach each PMT. The resolution achieved in the x-y plane was 45 mm. Other similar designs use the relative intensity of signal between the photosensors to calculate something analogous to a signal center-of-mass, which is correlated with the position of interaction.

The Single Volume Scatter Camera (SVSC) collaboration developed a monolithic prototype at Oak Ridge, Sandia, and Lawrence Berkeley National Laboratories (among other institutions). Their $50 \times 56 \times 60$ mm^3 plastic scintillator cube is read out by two 64-channel silicon photomultiplier (SiPM) arrays at opposite ends of the detector volume. The nonactive sides are painted black to reduce reflections. The operating principle is that the spatial distribution of hits on the SiPM array as well as the time of arrival of each scintillation photon can be used to deduce the position, energy, and timing of a neutron scatter so that double-scatter events can be used to image the source. So far, no experimental data on reconstructions are available, but they hope to achieve an angular resolution of approximately 0.1 radians [18].

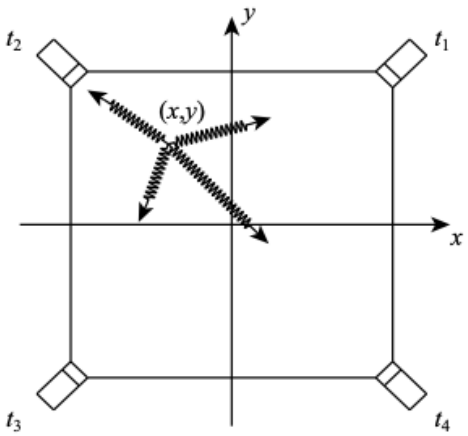

Figure 1.2: A sketch of a monolithic plastic scintillator with a photomultiplier tube at each corner from Tang *et al.* [17]. The position of interaction is reconstructed from the relative trigger times of each PMT.

1.2.2.2 Segmented scintillator detector designs

Another method to reconstruct information about event topology is to optically segment a detector volume. Sometimes this is accomplished by wrapping long rectangular bars of scintillating material with a reflector, stacking them together, and reading out the bars with a photosensor at each end. One such design is the Segmented AntiNeutrino Directional Detector (SANDD) [19, 20], shown in Fig. 1.3. The location of the bars provides information about the position of interaction along two dimensions (x-y), where the bar that produced the most light is taken to be the location of interaction. The position of the interaction in the third dimension (z) is calculated from the difference in magnitude of the signal generated at each photosensor. The resolution of the position in the x-y plane depends on the cross-sectional size of the bars and was between 10 [19] and 25 mm [20] in the z-direction.

The SVSC Collaboration also developed an optically segmented prototype detector. It uses wrapped scintillator bars, similar to SANDD. The position resolution in the x and y directions is dictated by the size of the bars (50 mm on a side).

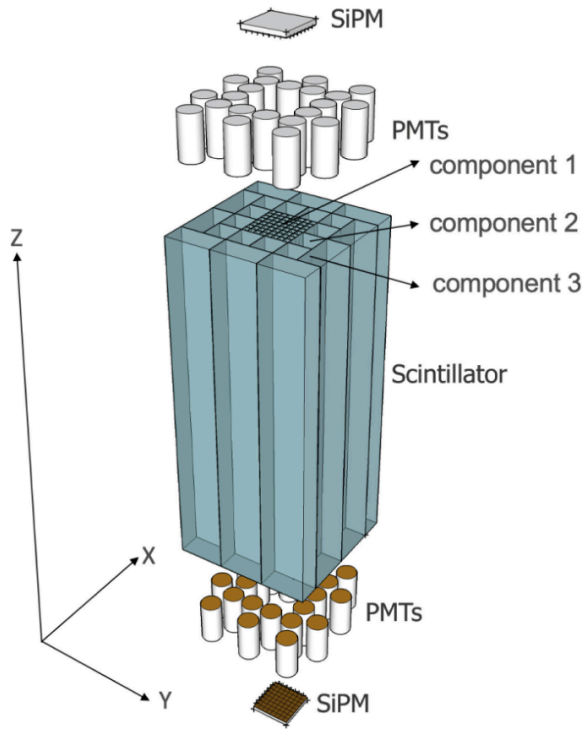

Figure 1.3: A rendering of the SANDD prototype design from Ref. [20]. All of the component scintillator bars are a ^{6}Li-doped plastic but vary in size and shape.

The z-position reconstruction ranges from about 15 mm to 25 mm depending on whether pulse amplitude, timing, or a combination of both is used to do the reconstruction [21].

A third example of physical segmentation are filter stack spectrometers. Filter stack spectrometers have layers of detectors separated by absorbers, usually lead or another high-z material. This results in a one-dimensional detector array. A common application of this type of detector is a spectral measurement of bremsstrahlung radiation. X-ray attenuation through dense materials has a strong energy dependence, so a given spectrum of incident X rays results in a unique distribution of energy deposition among the layers. Filter stack spectrometers are typically made with non-scintillating detectors, such as imaging plates or thermoluminescent detectors [22]. However, these have the disadvantage of slow readout. For high repetition

rate experiments, filter stack spectrometers have been proposed [23]. Notably, this type of detector does not provide event topology within a detector layer for individual interactions. Instead, the aggregate topology for many incident X rays is used to discern the distribution of initial X-ray energies.

1.2.2.3 Virtual segmentation (opaque scintillators)

Opaque scintillators are a novel technology that promises many unique advantages over existing designs, and the study of this nascent technology constitutes a major fraction of this thesis.

The idea of opaque scintillators was first published in 2021 by the LiquidO consortium [24]. LiquidO is a group dedicated to the investigation of opaque scintillators generally, and has several derived projects which aim to design and implement solutions to a variety of specific problems in radiation detection. These include CLOUD (a large detector that will provide insight into neutrino oscillation and other phenomena of interest to the particle physics community), AM-OTech (a reactor monitoring project), LPET-OTech (LiquidO for positron emission tomography), and others [25].

The Applied Nuclear Science Group at the University of Michigan is a member institution of LiquidO and CLOUD, and much of the following work was done in partnership with those collaborations.

In opaque scintillators, light confinement is achieved not by optical or mechanical segmentation but by the nature of the random walk taken by each photon in a highly scattering medium [26]. Thus, there is no "dead" material, and scaling up the size of such a detector is relatively simple. Because segmentation is achieved without introducing non-scintillating material, we refer to this effect as "virtual segmentation".

Wavelength-shifting (WLS) fibers can be used to collect the trapped light for readout. If the fiber array is sufficiently dense, then the topology of the energy

deposition inside a scintillation volume during a detection event can be reconstructed and potentially used for particle-type identification, or even, in the case of multiple scatters, to reconstruct the incident direction of the radiation.

Furthermore, because of the relaxation of the transparency constraint usually levied on scintillator material design, novel bright scintillator materials can be considered, and doping, (*e.g.*, with high-Z nanoparticles to increase photoelectric absorption of gamma rays) at unprecedented concentrations can be investigated.

1.3 Research question and organization of following chapters

The overarching goal of this thesis is to investigate some problems in radiation detection that can be addressed by resolving the spatial distribution of light following an "event" in scintillation detectors.

Here "event" usually means a discrete interaction of an incident quantum of radiation in a detector volume. However, in some cases there are many interactions within a very short time, and individual interactions cannot be distinguished. Chapter II presents a method to recover spectroscopic information for measurements subject to extreme pileup, as in the case of inverse Compton-scattered beams, through the use of a segmented scintillator array. This technique is analogous to filter stack spectrometers in that it seeks to use the spatial distribution of many events to reconstruct the characteristics of a group of incident particles. Each detector segment in the array is at a distinct angle from a target detector, such that the angular distribution of scattered gamma rays can be inferred and information about the incident energy spectrum can be reconstructed.

Chapter III provides background and theory for opaque scintillators. Topics addressed include scattering and absorption in bulk medium, reflection and refraction

into the WLS fibers, absorption by the WLS dye, and transport of the internally reflected photons to the photosensor. Chapter IV details the first quantitative study of light collection and transport from an inert opaque liquid into wavelength-shifting fibers. A Monte Carlo model was developed and validated using experimental data from a light injection system and compared with a diffusion model. The effect on the light collection of bulk medium scattering and absorption is examined.

Chapter V is a discussion of the design considerations for the LiquidO in Michigan Experiment (LiME), a 32-channel, 1-liter opaque scintillation detector system. Initial attempts at the production and implementation of a wax-based opaque scintillator called NoWASH-20 [27] are included, as well as the preliminary results from a cube detector made from welded aluminum.

Chapter VI describes the development of the second generation of LiME based on a 3D-printed acrylic cube. Experimental results from several fill liquids are shown, including several opaque formulations of water-based liquid scintillators (oWblS). The energy resolution and topological reconstruction precision are quantified.

Chapters II and III are based on peer-reviewed journal articles, whereas the remainder of the chapters feature previously unpublished work. Chapter VI is in the process of being published as an journal article.

Chapter VII provides context for the scope of work, summarizes the main results, and provides a roadmap for future studies.

CHAPTER II

Gamma-Ray Spectroscopy Using Angular Distribution of Compton Scattering

This chapter is based on an article published in 2022 in *Nuclear Instruments and Methods in Physics Research Section A* and co-authored by Prof. Igor Jovanovic [28].

The concept explored in this chapter differs from the remainder of the work in this thesis in several ways. First, the detector system is sparsely voxelized, meaning that only a portion of the space around the center of the experiment is instrumented. Secondly, voxelization is achieved by using an array of discrete detectors, instead of virtually segmenting a single detector. And thirdly, the detector system is designed not to reconstruct event topology, but rather the spectral characteristics of a beam of incident gamma rays. However, the underlying principle of the detection scheme is the same as for opaque scintillators: by designing a detector system to be able to measure the topology of an event in addition to simply quantifying energy deposition, much more information can be deduced about the exciting particle or particles. In this case, the topology of many scattering events is used to reconstruct information about the spectral characteristics of a polyenergetic beam of gamma rays.

2.1 Introduction

Intense pulsed sources of energetic electrons, such as those based on laser wake-field acceleration [29], hold promise for a number of applications in science, industry, medicine, and security [30]. One of the distinguishing features of those new sources is their short pulse duration, which produces a high peak radiation flux. These sources can be further used in conjunction with bremsstrahlung converter targets or inverse Compton scattering (ICS) [31] to produce high-energy X rays. In ICS, the X rays can be quasi-monochromatic, continuously tunable, and produced in a well-collimated beam [31]. Typical ICS pulses can contain $\mathcal{O}(10^8)$ or more photons within the span of a few ps or shorter [32]. No available single- or few-segment detector can resolve individual photons for pulse-height spectroscopy under those conditions while operating efficiently, *i.e.*, requiring a single or few pulses to determine the pulse spectrum. Instead, an efficient detector would record a single, large sum-pulse corresponding to the total energy deposited from many nearly simultaneous photon interactions. As a result, directly resolving the spectrum is not possible using a traditional method, where the energy deposited in each interaction event is measured separately. To date, ICS spectra have been calculated from the measured spectra of the electron beams used in ICS [33], by analyzing the beam transmission through a series of lead filters [32] and similarly a stacked calorimeter [34], by Compton-scattering the beam and performing magnetic spectroscopy on the Compton electrons [35], and by using an on-axis array of CsI scintillators, and comparing the resulting distribution of scintillation light to simulation [36, 37]. Additionally, a method of directly measuring Compton-scattered photons at a single angle of scatter has been demonstrated [38], but this approach relies on high detector segmentation

to prevent pileup and has low efficiency since scattering is measured only at a single angle. A new method that utilizes Compton scattering is demonstrated, which can reconstruct the photon energy spectral characteristics through analysis of the aggregate angular distribution of Compton-scattered photons measurable on a single shot and relating it to the known Klein-Nishina differential cross-section (KNDCS).

2.2 Theory

2.2.1 Klein-Nishina differential cross-section

The KNDCS, $\sigma(E,\theta)$, describes the probability for a photon of energy E to scatter into a differential solid angle and is dependent on the incident photon energy E and its scattering angle θ [39]:

(2.1)
$$\sigma(E,\theta) = Zr_0^2 \left[\frac{1}{1+\alpha(1-\cos\theta)}\right]^2 \left(\frac{1+\cos^2\theta}{2}\right)\left(1+\frac{\alpha^2(1-\cos\theta)^2}{(1+\cos^2\theta)[1+\alpha(1-\cos\theta)]}\right),$$

where Z is the atomic number of the scattering atom, r_0^2 is the classical electron radius, and $\alpha = E/m_0c^2$ is the photon energy normalized to electron rest mass equivalent energy. Representative shapes of the KNDCS for several incident photon energies ranging from 1 keV to 10 MeV are shown in Fig. 2.1.

A Compton-scattered polychromatic beam yields an angular distribution that is a superposition of the angular distributions from all spectral components that comprise the incident beam. For a continuous energy spectrum of incident photons collimated into a beam and described by $f(E) = dN/dE$, the number of photons scattered at an angle θ, $D(\theta) = dN/d\Omega$ is

(2.2)
$$D(\theta) = \int \sigma(E,\theta) f(E) dE,$$

neglecting photons that undergo multiple scattering. A photon with incident energy

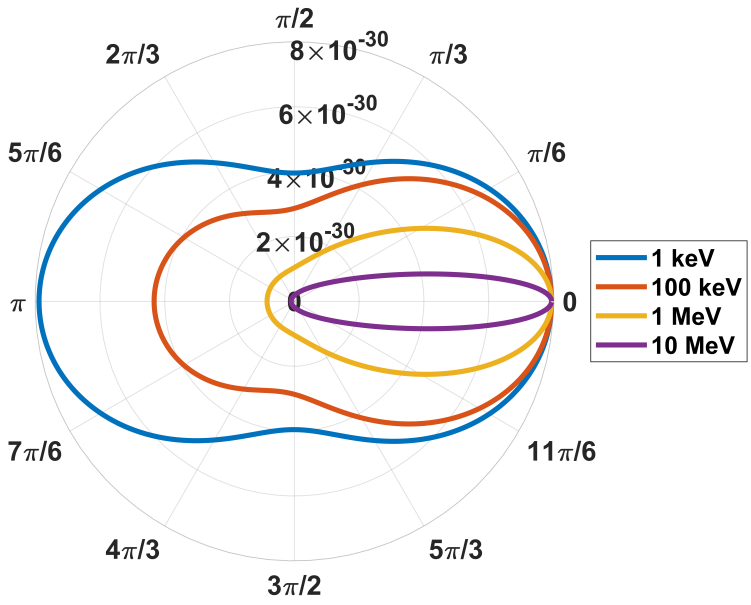

Figure 2.1: The Klein-Nishina differential cross-section shapes for photons of various energies scattered off a hydrogen atom. The photon is incident at $\theta = 0$ and the cross-section is measured in m^2. For heavier atoms, the magnitude of the KNDCS changes, but the shape is invariant for a given photon energy. Higher energy photons are much less likely to undergo a high-angle scattering than lower energy photons.

E scattered at angle θ has an energy

$$E'(E,\theta) = \frac{E}{(1+\alpha)(1-\cos\theta)}, \tag{2.3}$$

and thus the differential scattered photon energy flux $\Phi_E(\theta) = dW/d\Omega$ incident on a point detector placed at an angle θ is

$$\Phi_E(\theta) = \int \sigma(E,\theta)E'(E,\theta)f(E)dE. \tag{2.4}$$

The energy flux incident onto a detector placed at an angle θ is determined by an energy-integrated product of the angular distribution of scattered photons, the energy of scattered photons (which is also a function of angle and initial photon energy), and the incident beam energy spectrum $f(E)$. As a result, the shape of the angular distribution of Compton-scattered photons contains information about the energy spectrum of the incident beam.

2.2.2 Detector array response

The response of a detector depends not only on $\Phi_E(\theta)$, but also on its intrinsic efficiency and characteristic response function. The response of a 14-detector scintillation array exposed to a scattered polychromatic photon beam is considered. Once discretized, the array response can be modeled as

$$\begin{matrix} & \mathbf{A} & & & \mathbf{x} & & \mathbf{b} \end{matrix}$$

$$\begin{bmatrix} a_{1,1} & \cdots & a_{1,n} \\ \vdots & \ddots & \vdots \\ a_{14,1} & \cdots & a_{14,n} \end{bmatrix} \begin{bmatrix} x_1 \\ \vdots \\ x_n \end{bmatrix} = \begin{bmatrix} b_1 \\ \vdots \\ b_{14} \end{bmatrix} \tag{2.5}$$

where $\mathbf{A}$ is the detector array response matrix, in which $a_{i,j}$ is the light output in detector i per photon entering the system at energy j, x_n is the number of photons in energy bin n, and b_k is the total light output of the kth scintillation detector, which is assumed to be proportional to deposited energy. In this formulation, $\mathbf{A}$ is determined from modeling and simulation, while the light output $\mathbf{b}$ is measured experimentally. The objective is to reconstruct the binned energy distribution $\mathbf{x}$. The expected light output in detector i in terms of $\mathbf{A}$ and $\mathbf{x}$ is given by

$$b_i = a_{i,1}x_1 + a_{i,2}x_2 + ... + a_{i,n}x_n. \tag{2.6}$$

Note that the number of energy bins n in $\mathbf{A}$ and $\mathbf{x}$ must match but is not constrained by the number of detectors.

2.2.3 Solution algorithms

The response matrix, $\mathbf{A}$, has a high condition number ($\sim 10^4$ for 14 energy bins), rendering a direct and accurate solution through matrix inversion challenging [40]. Among the methods commonly applied to ill-conditioned inverse problems, least

squares, regularized least squares [41], singular value decomposition [42], and Tikhonov regularization [43] were considered. While several of the methods are effective in simulating a large (>60-detector) array, they all failed with an array of more practical size such as was employed in the experimental component of this study. Another method of solving inverse problems is the maximum likelihood expectation maximization (MLEM) algorithm [44, 45]:

$$x_j^{k+1} = \frac{x_j^k}{\sum_{i=1}^{m} A_{ij}} \sum_{i=1}^{m} \frac{A_{ij} b_i}{\sum_{l=1}^{n} A_{il} x_l^k}, \tag{2.7}$$

where x^0 is an initial guess, here chosen as a flat positive spectrum with 100 photons/bin. This method is desirable because it does not require *a priori* knowledge of the solution, making it capable of solving general problems. The MLEM algorithm achieved the most accurate spectral reconstruction of the linear solvers compared in this work, but it was sensitive to noise in the measurement vector b. Another tool that can be used to solve problems of this type is an artificial neural network (ANN). While the ANN functions as a "black box", its ability to recognize patterns in the pairings of x and b vectors still relies on the same physics described in Section 2.2. Furthermore, the ANN demonstrated more tolerance to noise in the measured light output of the array detectors than the MLEM algorithm and was more successful in correctly reconstructing spectral shapes. The performance of an ANN is compared to that of the MLEM in Section 2.5.1.

2.3 Simulation

2.3.1 Response matrix

A model was developed and the response matrix was simulated in the Geant4 framework [46]. Response matrices were generated for 14, 50,100, 250, 500 and 1000 energy bins. Two examples of the calculated response matrices are shown in Fig. 2.2.

The light measured in a scintillation detector was assumed to be proportional to energy deposited, since the detectors used in the experiment were previously found to exhibit a good linearity over the energy range considered [47]. Two sets of response matrices were generated. The first was made to simulate the monoenergetic experiment described in Section 2.4.2; 4×10^{10} photons with a flat energy spectrum in the range of 0–2000 keV were simulated. The incident photons were generated isotropically within a solid angle of 0.224 sr, such that the entire scattering target was illuminated. As described in Eq. (2.5), the response matrix was filled such that bin $a_{i,j}$ was the sum of all energy deposited in detector i by photons in energy bin x_j. Lastly, each bin was normalized to the number of photons within that energy range that were incident on the detector system. As expected from the shapes of the KNDCS at various energies (see Fig. 2.1), higher-energy photons preferentially deposit energy in detectors placed at shallower angles with respect to the incident photon direction (see Fig. 2.2). The second set of response matrices was generated under the same conditions described above, except the photons were emitted in a pencil beam instead of quasi-isotropically, which more accurately reflects the characteristics of an ICS beam. For the simulation to match the array response, it is necessary to include smearing and trigger thresholds. An event has a probability of triggering the detector that depends on the detector resolution and trigger threshold. For very low energy incident photons, this is impossible, which explains the empty bins in the low energy region of the 500-bin response matrix shown in Fig.2.2.

2.4 Experiment

2.4.1 Array design

An organic liquid scintillator (2"×2" cylindrical Eljen EJ-309) was chosen as the scattering target to strike a balance between scattering efficiency and minimizing

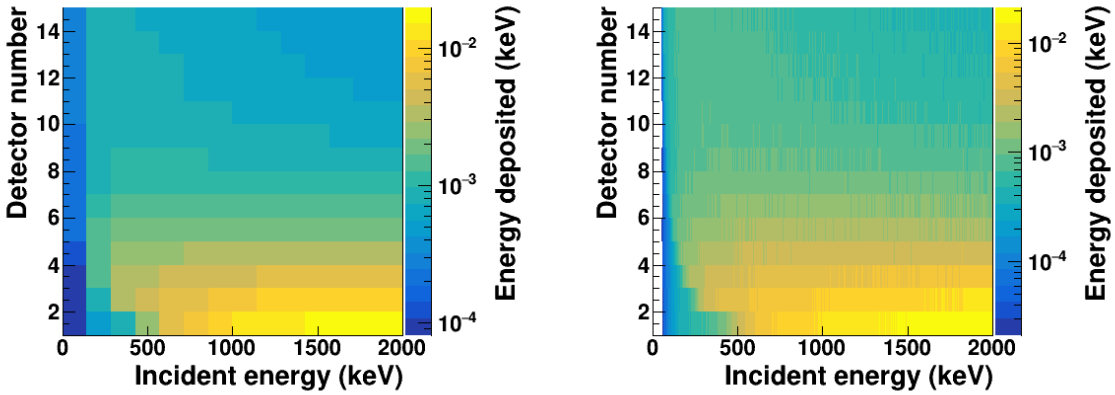

Figure 2.2: Simulated response matrices of (left) 14 and (right) 500 energy bins for a 14-detector array with 4×10^{10} incident photons in the range of 0–2000 keV. Detector 1 is located at a scattering angle of 12° with respect to the incident direction, and detector 14 is at a scattering angle of 168°, with detectors spaced at 12°.

the fraction of events that involve double scatters and photoelectric absorption [48]. The detector array comprises 14 positions for a 2"×4"×16" NaI(Tl) scintillator, with lead shielding placed between them to prevent crosstalk. The detector positions were arranged at 12° spacing with an uncertainty of ±2°, from 12° to 168° (see Fig. 2.3). The distance between the source and the target was 0.75±0.05 m, and the distance between the target and array detector face was 1 ±0.05 m. The fundamental tradeoff arising in an experimental design that employs a fixed number of independent detectors (pixels) is that between efficiency and fineness of angular sampling. A statistically significant number of photons must be detected at each detector position. Thus, the expected intensity of the incident signal informs the constraints of the experimental geometry [38]. At the cost of increasing complexity, additional array detector positions could be used. A three-dimensional array could be constructed, sampling much of the sphere surrounding the target. Increasing the number of detectors will likely improve the accuracy of spectral reconstruction by reducing the impact of noise in the signal of each individual detector, but this requires

an additional systematic study.

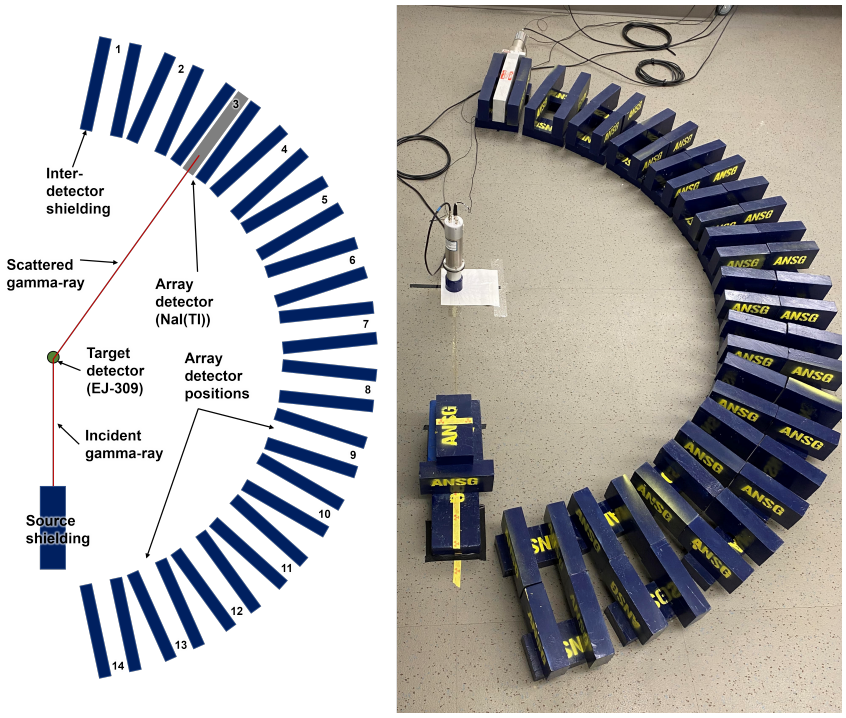

Figure 2.3: (left) A schematic of the experimental setup with an EJ-309 scattering target and 14 detector positions for a NaI(Tl) array detector. A photon is scattered from the target detector to detector 3. The source is inside a lead housing to shield the array detectors from direct exposure, and the detectors are shielded to prevent crosstalk. A coincidence is required between the target and a single array detector for the event to be counted. The light output of the array detector was integrated across the entire measurement time to simulate pileup. (right) A photograph of the experimental setup, with the array detector in position 1.

2.4.2 Experimental setup

For a single-shot measurement using this technique, careful calibration of the response of each array detector would be necessary. This proof-of-concept experiment used a single detector, and separate measurements were taken at each position. The primary difference between measuring a single detector position at a time and using the entire array simultaneously is the chance for a photon to scatter from one array detector to another, or crosstalk. Each detector position had two inches of lead shielding it from its neighbors to minimize crosstalk. In a full-array simulation

of 10^8 661.7-keV photons, no photons deposited energy in multiple array detectors; therefore, the effect of crosstalk is negligible for the energy range used in this experiment. The trigger threshold was set to 12 keV for the target detector and 18 keV for the array detector. These thresholds were chosen to minimize low-energy events from the background while still counting the lowest-energy true events. A 661.7 keV photon scattered from the target detector into the array detector at the shallowest angle (12°) deposits only 18.2 keV of energy into the target detector; however, a lower threshold was required to account for the low energy resolution of EJ-309. Similarly, a 661.7 keV photon scattered into the array detector at the largest angle of scatter (168°) deposits up to 185.8 keV of energy. The measurements were taken with the target detector operating in coincidence mode with the array detector, with a 96-ns coincidence window. Data acquisition was performed using a CAEN V1725 digitizer with DPP-PSD firmware and the CAEN CoMPASS software. Six-hour measurements were taken using a ^{137}Cs source with an activity of 62 ± 5 µCi. The source was collimated to minimize direct irradiation of the array detector (see Fig. 2.3). During a 6-hour measurement, approximately 5×10^7 gamma rays were incident on the scattering detector. This integrated fluence was chosen to be representative of an ICS shot, wherein estimates for photon yield in practical experiments range from 10^7 to 10^8 [49, 50].

2.4.3 Data

The total energy deposited in each detector was calculated by adding the contributions from each pulse and subtracting background (including chance coincidence). The background was estimated by averaging the number of counts in each energy bin within the background region shown in Fig. 2.4, then multiplying that number by the width, in ns, of the integration region for that energy bin. The integration region

boundaries were established by visual inspection, except for the high-energy limit, which is set to be 20% above the expected photopeak for each angle of scatter. The

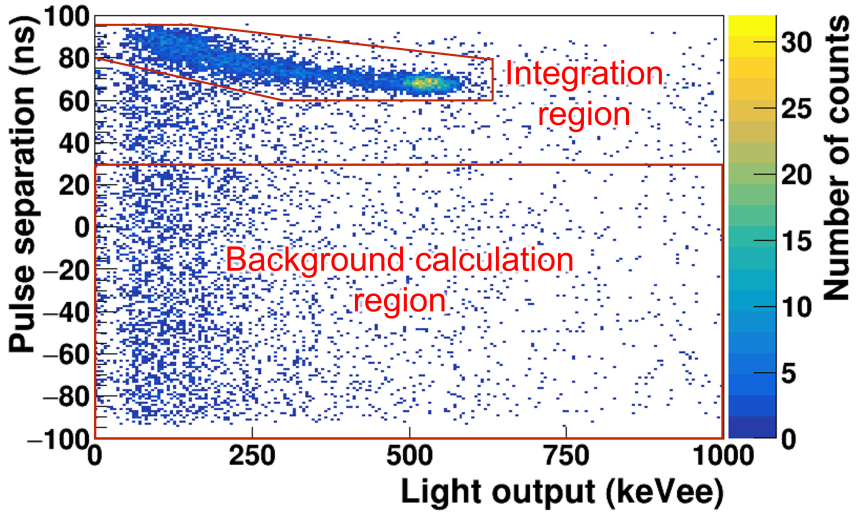

Figure 2.4: The light output spectrum for the array detector at a scattering angle of 36° as a function of the delay between the trigger in the scattering detector and the target detector. The photopeak of scattered photons can be seen as the area of high density within the integration region at 530 keV. The delay does not represent the time of flight of the scattered photon between detectors, but instead a constant time offset between the channels. The regions used to calculate the background and integrated light output of the array detector are marked in red.

integrated light output for each detector position is plotted along with the results of simulation in Fig. 2.5. The uncertainty of the angle of scatter is 2°. The uncertainty for simulated integrated light output was determined as the standard deviation of five repeated full-array simulations of 5×10^7 661.7-keV photons. The uncertainty for experimental integrated light output, b_i in detector i, is assumed to be determined by statistics, *i.e.*, proportional to the uncertainty in the number of counts N:

$$\delta b_i = b_i/\sqrt{N} \tag{2.8}$$

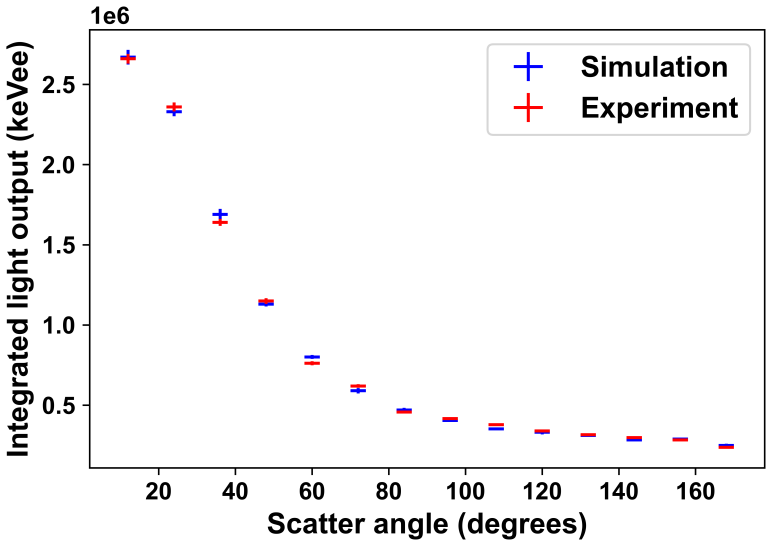

Figure 2.5: The experimental and simulated integrated light output for a 14-detector array exposed to a scattered beam of monoenergetic 661.7-keV photons from a 62-µCi ^{137}Cs source for 6 hours.

2.5 Results

2.5.1 Monoenergetic experimental spectrum

In order to quantify the quality of reconstruction, the cosine similarity between the discretized true and reconstructed energy spectra can be used. The cosine similarity of two vectors $\mathbf{A}$ and $\mathbf{B}$ is given by

$$\text{cosine similarity} = \frac{\mathbf{A} \cdot \mathbf{B}}{\|\mathbf{A}\|\|\mathbf{B}\|}, \tag{2.9}$$

where a score of 0 indicates perfect orthogonality, and 1 parallel vectors. Cosine similarity is a stringent metric of comparison for high-dimensionality vectors, as it can assume a value of 0 for solutions that are off by a single energy bin. To add context, the weighted average energy of each reconstruction vector is also provided. Weighted average energy is calculated as

$$\bar{E} = \frac{\sum_{i=1}^{n} E_i x_i}{\sum_{i=1}^{n} x_i}, \tag{2.10}$$

where n is the number of energy bins, x_i is the number of counts in the i^{th} energy bin, and E_i is the center of the bin in keV.

2.5.1.1 MLEM Reconstruction

The MLEM algorithm does not prioritize any particular spectral shape but rather seeks to minimize the error between experimental light output and the response matrix prediction. As such, the MLEM algorithm sometimes finds solutions with a large number of low-energy photons, such that the reconstruction is unrealistic. In order to prevent the MLEM algorithm from finding these solutions, the bottom 5% of energy bins were constrained to the value of 100.

Table 2.1: The performance of MLEM and ANN reconstruction of the spectrum of a monoenergetic ^{137}Cs source.

Energy bins	Cosine similarity		Weighted average (keV)	
	MLEM	ANN	MLEM	ANN
14	0.8008	1.0000	667.3	642.0
50	0.0000	1.0000	667.0	659.0
100	0.0000	1.0000	673.6	668.6
250	0.0000	0.8728	676.7	658.2
500	0.0000	0.0519	720.2	672.2
1000	0.0000	0.0000	711.4	644.4

The results of the MLEM reconstruction are shown in Fig. 2.6 and summarized in Table 2.1. In general, the MLEM algorithm fails to reconstruct a monoenergetic spectrum, with more finely-binned response matrices resulting in noisier reconstruction. However, all reconstructions with under 500 energy bins produced a weighted average energy within 3% of the true value after 2.5×10^5 iterations, and for 500 and 1000 energy bins, within 9%. Thus, this analysis technique is suitable for determining the energy centroid of a monoenergetic or quasi-monoenergetic spectrum.

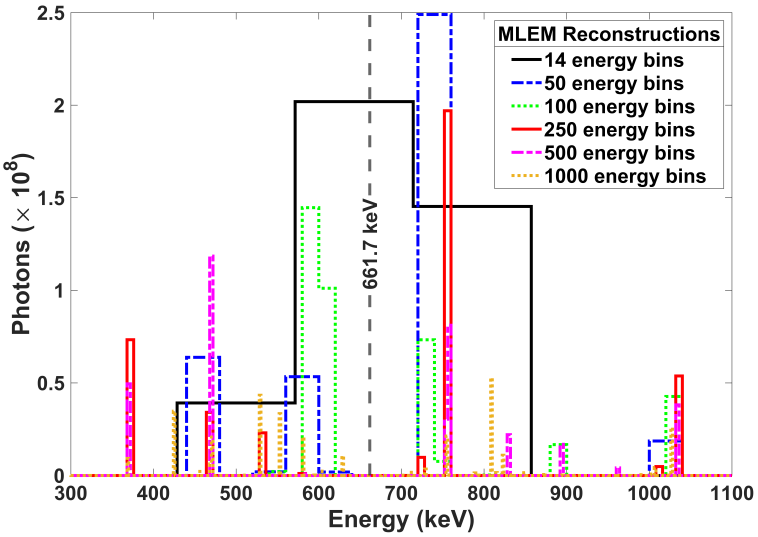

Figure 2.6: The results of spectral reconstruction using MLEM after 2.5×10^5 iterations with a variety of sizes of response matrices. The true incident spectrum consists of monoenergetic 661.7-keV gamma rays from ^{137}Cs. While the reconstruction of spectral shape is poor, the average energy was within 3% of the true value for 14-250 energy bins and 9% for 500 and 1000 energy bins.

2.5.1.2 ANN Reconstruction

Simulating a sufficient quantity of training data in Geant4 to train a neural network is computationally prohibitive. Instead, synthetic light output data for the detector array were created from random monoenergetic spectra, as described in Eq. (2.5), by multiplying the response matrix and spectra. To make the data realistic and to avoid repetition in the training data set, Gaussian noise was added to the measurement vector b, with a signal-to-noise ratio (SNR) of 40. The SNR is calculated as

$$SNR = b_i/\sigma_n, \tag{2.11}$$

where b_i is the expected value of the light output for array detector i, and σ_n is the standard deviation of the noise. The network was built using the Keras library [51] according to the specifications listed in Table 2.2. The results of the ANN

reconstruction of the ^{137}Cs spectrum are summarized in Table 2.1 and shown in Fig. 2.7. The network was successful in reconstructing the spectrum with coarse energy bins, but the performance degraded as the number of bins increased. It should be noted that the larger response matrices had lower numbers of counts in each energy bin and were therefore noisier (see Fig. 2.2). It is possible that if additional computation time is spent to generate smooth, finely binned response matrices, reconstruction with larger numbers of energy bins can be achieved.

Table 2.2: The ANN settings used to reconstruct the monoenergetic experimental spectrum.

Setting	Value	Note
Size of training dataset	$5 \times 10^{6*}$	Constructed with an SNR of 40
Epochs	20	
Batch size	64	
Dense hidden layer 1	28 nodes	Sigmoid activation
Dense hidden layer 2	40 nodes	Sigmoid activation
Output layer	1 node/energy bin	Sigmoid activation
Loss function	Mean squared error	
Optimizer	Adam	Learning rate: 0.001

* training dataset size was 10^7 for 1000 energy bins.

2.5.2 ICS spectral reconstruction from synthetic data

The spectral shape of ICS X rays is a function of, among other parameters, electron beam energy, electron beam divergence, and laser bandwidth. The electron beam energy primarily affects the energy centroid, while both the electron energy spread and laser bandwidth affect the width of the X-ray energy distribution. For training the neural network, ICS data were simulated by a random distribution of two parameters: a monoenergetic electron beam in the range of 175–275 MeV and a transform-limited 0.1–10 ps laser pulse. The corresponding ICS spectrum was then calculated according to the method described in Ref. [52]. The spectra are quasi-monoenergetic and characteristically asymmetrical, with a low-energy tail. Unlike the monoenergetic spectra used to train the network in Section 2.5.1.2, the training

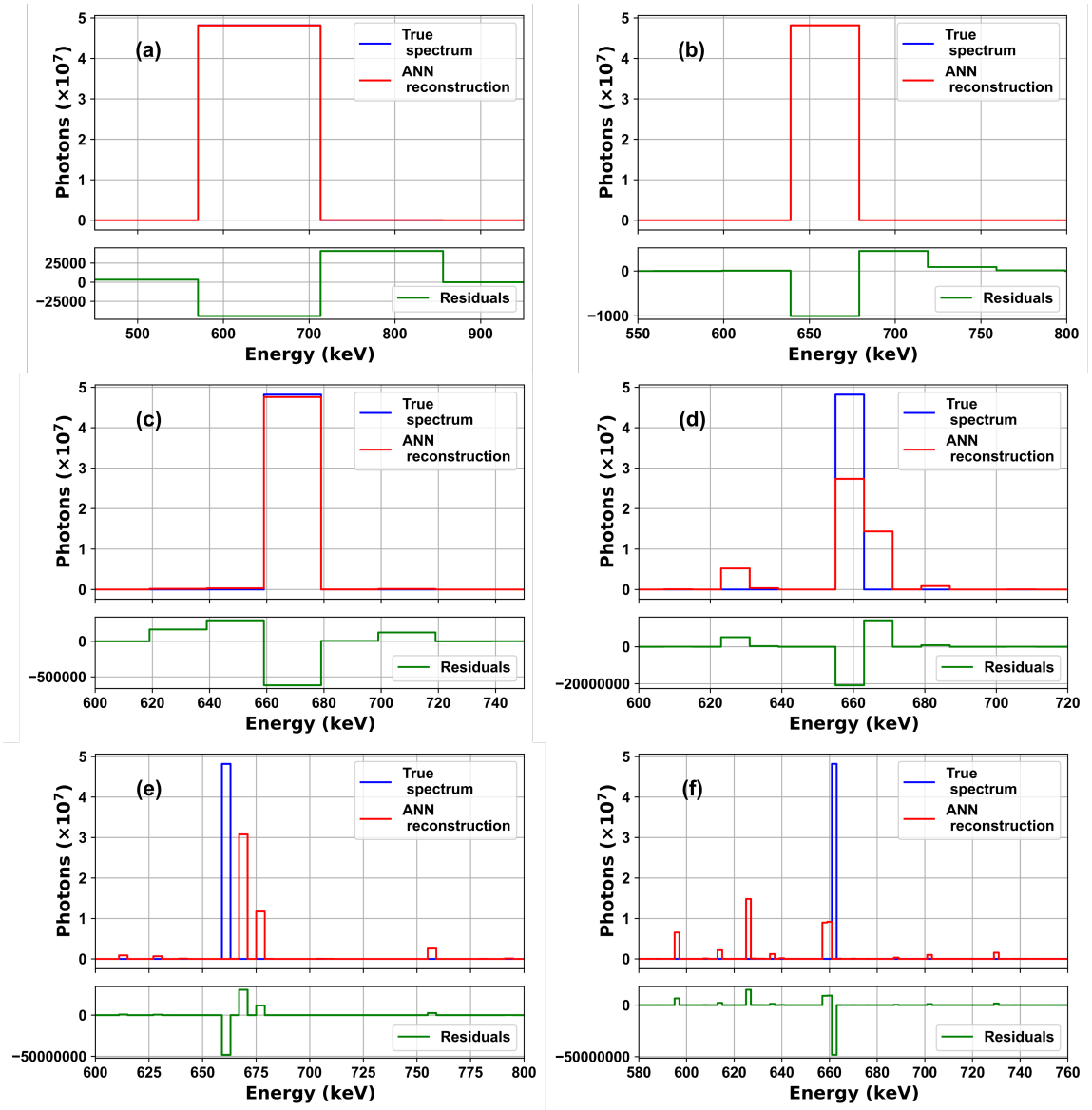

Figure 2.7: The results of spectral reconstruction using ANNs trained with data constructed using responses matrices of (a) 14, (b) 50, (c) 100, (d) 250, (e) 500, and (f) 1000 energy bins. The true incident spectrum was monoenergetic 661.7 keV photons from ^{137}Cs. The cosine similarities and energy weighted averages are tabulated in Table 2.1.

data varied not just by centroid, but also by their width. The training data were constructed in a manner similar to the training data for the monoenergetic reconstruction. The randomized spectra were multiplied by response matrices of various sizes to obtain the light output for each detector in the array. The settings used to train the network are shown in Table 2.3. The test data – which the network did not see during training – were constructed through direct simulation. This was computationally feasible because the testing dataset can be much smaller than the training dataset since it is only used to evaluate the quality of the neural network. First, a random ICS spectrum was generated as described above and then used to create a probability density function. Primary particles in the simulation were created with energy sampled from this distribution. The number of photons simulated was varied and smearing was applied to the detector response to create light output spectra with different amounts of noise.

Table 2.3: The ANN settings used to reconstruct the ICS pulse spectra.

Setting	Value	Note
Size of training dataset	10^6	No artificial noise added
Epochs	50	
Batch size	64	
Hidden layer 1	28 nodes	Sigmoid activation
Hidden layer 2	200 nodes	Sigmoid activation
Output layer	1 node/energy bin	Sigmoid activation
Loss function	Mean squared error	
Optimizer	Adam	Learning rate: 0.001

Figure 2.8 shows a reconstruction of ICS pulses using an ANN trained with a response matrix of 1000 energy bins. For each case, five pulses were simulated, each with the number of photons indicated. Reconstruction was performed on each, and the results were averaged. The error bars are the standard deviation of the five reconstructions. In each case, the cosine similarity was above 0.9.

It is important to note that due to the highly collimated nature of an ICS beam,

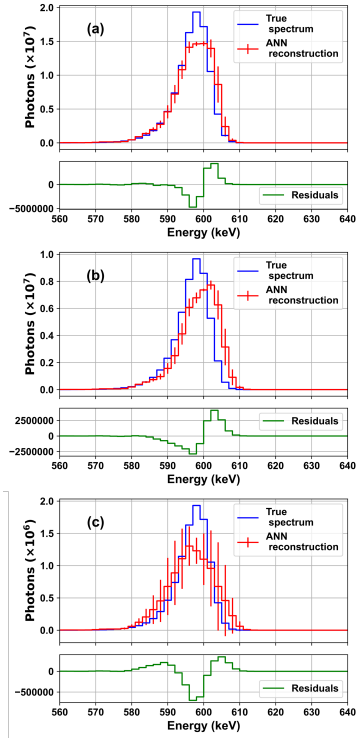

Figure 2.8: The results of spectral reconstruction using ANNs trained with simulated ICS pulses. A 1000 energy bin response matrix was used to train the network. ICS pulses were simulated with (a) 10^8 photons (cosine similarity: 0.9749), (b) 5×10^7 photons (cosine similarity: 0.9197) and (c) 10^7 photons (cosine similarity: 0.9537). The error bars are the standard deviation from the reconstruction of five pulses.

the 1000 energy-bin ICS response matrix was much more efficient to simulate than for the isotropic source, and thus had more consistency between bins. This likely contributed to the better performance of the finely-binned reconstruction when compared to the experimental reconstruction of an isotropic monoenergetic ^{137}Cs source.

2.6 Conclusion

A novel technique that could be used to resolve gamma-ray spectra in high pileup environments was demonstrated. The spectrum of a monochromatic beam of 662-keV gamma rays was reconstructed using two methods. The MLEM method was more consistent in reconstructing the average energy of the spectrum with coarsely-binned response matrices but failed to reconstruct the monoenergetic shape. The ANN method was better at reconstructing the spectral shape for response matrices of 250 bins and fewer, but was still unsuccessful when more finely binned response matrices were used. The method was used along with an ANN to reconstruct simulated ICS pulses consisting of 10^7-10^8 photons with a cosine similarity above 0.9.

2.7 Future Work

This technique may be well-suited for short-duration, high-intensity measurements, like an ICS pulse. However, to use Compton array spectroscopy in this application, additional studies are required. The array must tolerate the electromagnetic pulse associated with ICS shots. The scintillator and light sensor (*e.g.*, photomultiplier) response to large sum pulses needs to be well understood. Among the possible sources of nonlinearity are photocathode bleaching and dynode space charge effects [53]. In some situations, filters between the scintillating crystal and photocathode [54], PMTs that operate with low gain [55], or low light-producing detectors [56] may be needed to avoid saturation, all of which could be accounted

for in response matrix generation.

The scattering target was chosen to be a detector so that coincidence can be used between the target and array to filter out the background for the long measurements. However, in a short-pulse measurement, the target need not be a detector but could be an inert object optimized for the efficiency of Compton scattering. For instance, a hydrocarbon target would have favorable Compton scattering properties while minimizing pair production.

Additionally, experimental work with larger arrays should be performed to confirm that more precise and accurate results are achievable.

Lastly, the parameter space for an ICS beam is large, and only a small fraction was investigated here. For instance, the photon energy in an ICS beam can be broader than considered here and can have an angular dependence [57] that was not modeled. This technique should be investigated for stability under these conditions.

CHAPTER III

Light Transport and Collection in Highly Scattering Media

This chapter will discuss the theory and modeling for light transport in opaque scintillators, as well as the physics underlying light collection and transport in WLS fibers. Additionally, an estimation is made for the detection efficiency of an ideal opaque scintillation detector.

3.1 Light transport in turbid media

The transport of light can be modeled in several ways, including wave mechanics, "ballistic" kinematics, and diffusion [58]. This analysis forgoes the wave treatment, except when considering the reflection and refraction of light into and through the WLS fibers. For some applications, this simplification would be inappropriate. For instance, if the mean free path of light is on the order of the wavelength, the photons can be fully contained due to Anderson localization [59, 60]. In contrast, in opaque scintillators, the absorption length is multiple meters, and the scattering length is generally chosen to be on the order of a millimeter. Scintillation light has a spectrum that usually peaks around 400 nm, or 1/2500 of the mean free path, which puts opaque scintillators well outside of the Anderson regime. Furthermore, because the photon density is low in such a system, the interference is negligible. Lastly, because the polarization of scintillation light is random, the effects that could arise with

polarized light are neglected.

The transport of scintillation light in the detection system is modeled primarily as ballistic. Ballistic photons only change direction when they occasionally interact, and such a model is compared with diffusion theory in Chapter IV. The primary advantage of this modeling approach is that powerful, standard Monte Carlo particle transport frameworks can be used, such as Geant4 [46].

The remainder of this chapter describes various processes that a photon can undergo in an opaque scintillation detector, how light is collected by the wavelength-shifting fibers, and the readout process.

3.1.1 Scattering

There are two regimes of optical photon scattering germane to this application: Mie scattering and Rayleigh scattering. Both are elastic scattering, which means that the energy of the photon is the same before and after the scatter. Mie scattering describes the general case of a plane electromagnetic wave scattering off of a sphere. Rayleigh scattering is the special case of Mie scattering, in which the scatterer is much smaller than the wavelength of the scattering photon [61]. An important difference is that Rayleigh scattering is isotropic, whereas the distribution of Mie scattering is a function of the size of the scattering sphere [62].

For isotropic scattering, the effect of scattering on light transport can be described through a scattering coefficient, usually denoted as μ_s. The scattering coefficient μ_s has units of inverse length and is equal to the expected number of scattering events per unit length in a material. The average anisotropy of a scattering event due to Mie scattering can be accounted for by converting the scattering coefficient to the

reduced scattering coefficient:

$$\mu_s' = \mu_s(1-g), \tag{3.1}$$

where g is the average cosine of the scattering angle, known as the anisotropy factor. For isotropic scattering, the average cosine of the scattering angle is 0, and the reduced scattering coefficient is equal to the scattering coefficient. For scattering that tends to be forward-directed, g will be a positive number in the range of $0-1$, and the reduced scattering coefficient is lower than the scattering coefficient.

Consider the average distance from an origin that a photon reaches, given fixed absorption and scattering coefficients, and a variable anisotropy factor. For a large anisotropy factor of $g \to 1$, the scattering is forward-directed and does not significantly perturb the path of the photon, allowing it to travel a long distance before being absorbed. This is equivalent to infrequent isotropic scattering. Conversely, if $g \to 0$, the photon takes a folded path, and its net distance traveled is shorter. In this way, the reduced scattering coefficient accounts for scattering anisotropy in models using only isotropic scattering.

After many scatters, the reduced scattering coefficient correctly models the diffusion of photons in a material. However, this approximation may result in large errors in photon density after only a small number of scatters. In this application, that could manifest as an incorrect estimation of photon collection into a WLS fiber for photons that originate less than a few mean free paths from the fiber. To investigate the impact of this approximation, a Geant4 model was developed to create photons near a fiber with an isotropic distribution of initial directions. Light propagation in bulk materials that have identical reduced scattering coefficients, but variable scattering coefficients and anisotropy factors, is then compared.

For the remainder of this thesis, materials are often described by their scattering

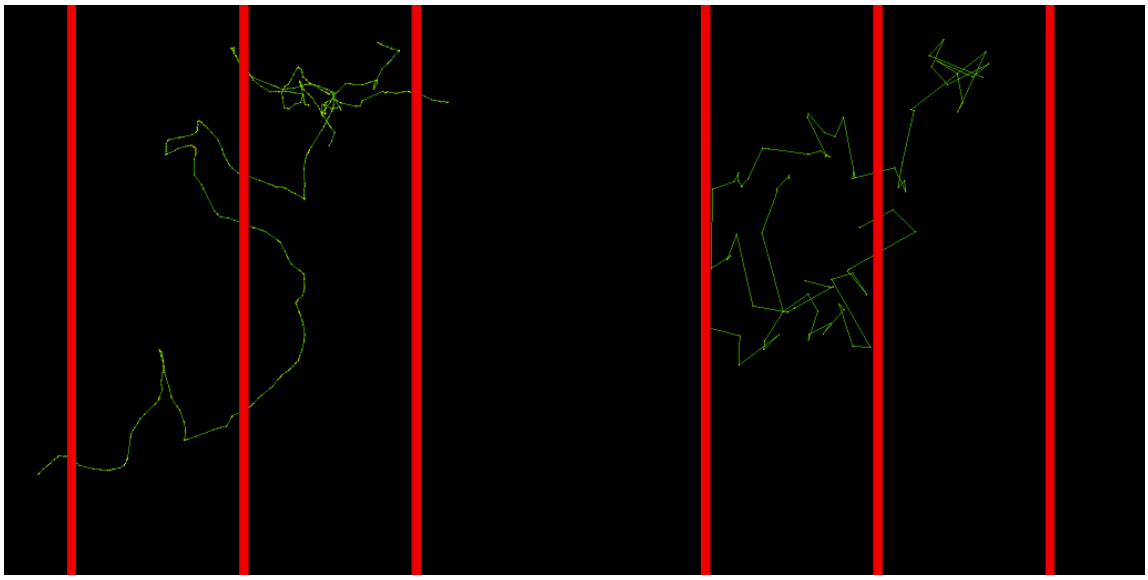

Figure 3.1: Example photon paths through a bulk medium with a reduced scattering length of 5 mm and an absorption length of 16 cm. The left panel shows the propagation of five photons for the case in which the anisotropy parameter $g = 0.9$, and the right panel shows the case in which $g = 0.1$. The lower anisotropy results in less frequent, but higher-angle scatters. The vertical red lines in each panel are WLS fibers at a 2 cm pitch.

lengths instead of their scattering coefficients. The scattering length is the inverse of the scattering coefficient and denotes the average distance a photon travels between scattering events.

Figure 3.1 shows example simulated photon paths through an opaque liquid with the same reduced scattering lengths, but different anisotropy factors.

Figure 3.2 shows the distribution of photoelectrons generated at the photocathode after photons are captured in the fiber nearest to the origin of the photons in the simulation. In this case, 1000 photons were generated 1 mm from the fiber for each event. The means and standard deviations of the distributions are 21.8 ± 4.6 photoelectrons for $g = 0.9$, 21.6 ± 4.6 photoelectrons for $g = 0.5$, and 22.3 ± 4.4 photoelectrons for $g = 0.1$.

Figure 3.3 shows the distribution of total photoelectrons generated after photons

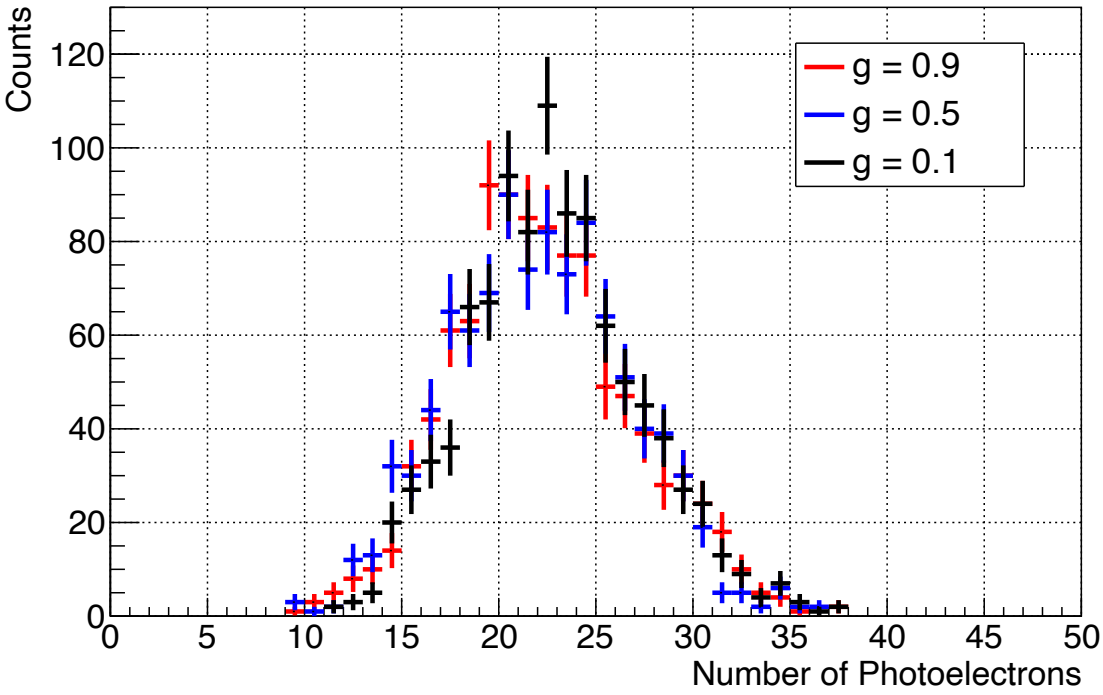

Figure 3.2: The distributions of photoelectrons generated by photon captures in the WLS fiber nearest to the origin of the photons for three different anisotropy factors. The reduced scattering length in each case is the same. For each event, 1000 photons were generated isotropically 1 mm from the fiber.

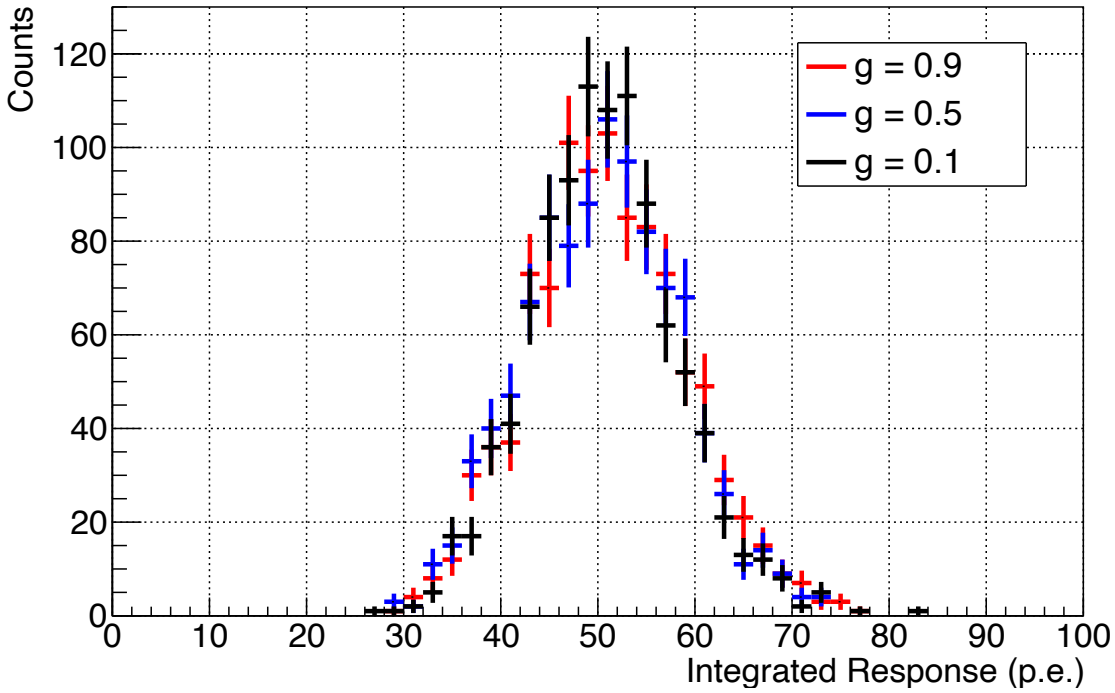

Figure 3.3: The total signal across all channels for photons transported through a highly scattering liquid with the same reduced scattering length, but different anisotropy factors. As expected, the distributions are very similar, demonstrating that the reduced scattering coefficient is an adequate approximation in modeling photon propagation for this context.

were captured in any fiber in a 1 L, 32-channel detector. The detector is described in Chapter VI. The means and standard deviations of the distributions are 50.9 ± 8.1 photoelectrons for $g = 0.9$, 50.4 ± 8.0 photoelectrons for $g = 0.5$, and 50.6 ± 7.5 photoelectrons for $g = 0.1$.

This demonstrates that even for photons born very close to fibers, the reduced scattering coefficient does an adequate job of modeling the photon diffusion in an opaque liquid. The Rayleigh approximation will therefore be used throughout the remainder of this thesis. A primary benefit of this approximation is that the particle-size distributions of the opaque liquids do not need to be known, as they would for correct modeling of Mie scattering. Additionally, due to the decreased number of scatters in the simulation, a model using Rayleigh scattering is significantly more computationally efficient than a comparable Mie model.

3.1.2 Wavelength-shifters in the bulk media

A second process experienced by photons in a highly scattering scintillation detector is wavelength-shifting. Many scintillating compounds do not create light that is well-matched to photosensors. For example, the emission spectrum of linear alkyl benzene with 2,5 diphenyl-oxazole (PPO) fluor peaks around 350 nm [63]. Although a variety of photocathode treatments are available, a typical photomultiplier tube (PMT) is most sensitive to light above 400 nm. To red-shift the spectrum of scintillation light from a material like LAB, a wavelength-shifting fluor is often added. Fluors absorb the scintillation light and reemit it at a longer wavelength with high efficiency. A typical wavelength-shifting fluor is 1,4-Bis(2-methylstyryl)benzene (bis-MSB), which has an emission spectrum that peaks at 423 nm and a quantum yield (efficiency of re-emission) of 92.6% at 350 nm [64].

3.1.3 Bulk absorption

In addition to scattering and undergoing wavelength shifts, optical photons can be absorbed by the bulk media in which they are moving. This represents a loss of signal and is generally undesirable in scintillation detectors.

Bulk absorption in scintillation detectors follows the Beer-Lambert law [65],

$$I(x) = I_0 e^{-\mu_a x} \tag{3.2}$$

where I_0 is the initial intensity of the light, μ_a is the absorption coefficient in units of inverse length, x is the distance traveled through the absorber by the light, and $I(x)$ is the remaining intensity after distance x.

The distance x is not the displacement, but rather the length of the path the photon takes. In opaque scintillators, this distance is often much larger than the displacement because of the repeated scattering described above.

The probability for a photon to be absorbed in a slice of its path dx after traveling a path length x is given by the product of probabilities that it will not be absorbed before it has traveled x and the probability it is absorbed in dx (simply $\mu_a dx$):

$$P(x) = \mu_a e^{-\mu_a x} dx. \tag{3.3}$$

The mean distance traveled by a photon before being absorbed is given by the normalized first moment of $P(x)$:

$$\bar{x} = \frac{\int_0^\infty x \mu_a e^{-\mu_a x} dx}{\int_0^\infty \mu_a e^{-\mu_a x} dx} \tag{3.4}$$

$$\bar{x} = 1/\mu_a \tag{3.5}$$

$$\bar{x} = \lambda_a, \tag{3.6}$$

which is the absorption length of the liquid.

Similarly to scattering, we often describe materials by their absorption lengths rather than coefficients. Opaque scintillators are designed to have absorption lengths much longer than their scattering lengths, so that an absorption event is rare compared to a scattering event.

3.1.4 Reflection

Reflection occurs within an opaque scintillation detector volume at two sets of boundaries: the wavelength-shifting fiber interfaces and the detector walls. The reflection at the surface of the fibers is discussed below. The nature of reflection at the walls depends on the materials used to construct the detector body. For example, the aluminum body used for the prototype detector described in Chap. V results in primarily specular reflection, while the acrylic body used in Chap. VI causes diffuse or Lambertian reflection. However, because of the nature of highly scattering bulk media, the net difference in photon transport caused by the two regimes of reflection is negligible. What is more important is the efficiency of reflection, also known as the reflectivity. Similarly to bulk absorption, a photon that is absorbed at the walls of the detector instead of reflected is lost and cannot contribute to the signal generated by the rest of the event. Reflection at the walls in an opaque scintillator is only a concern for events that take place within a few mean-free paths of the wall. The larger the detector, the smaller the fraction of the detector that meets this criterion. For the small prototypes discussed in Chs. V–VI, a large fraction of the volume of the detector meets this criterion, and the reflectivity of the walls is important in the modeling process.

3.2 Light collection into WLS fibers from a liquid scintillator

3.2.1 Reflection at the fiber-scintillator boundary

There is a large body of literature on the use of WLS fibers in scintillators in the field of high-energy physics. Commonly, these applications are solid detectors wherein grooves have been carved to allow for the passage of the WLS fibers. Artikov *et al.* found in 2019 that adding optically matched glue to the grooves increased light collection efficiency by up to 50% compared to fibers laid in bare grooves [66]. The underlying cause of collection inefficiency when no glue is present is the small air gap between the scintillator and the fiber cladding. Due to the relatively high index of refraction of the scintillator, the photons face an additional probability of reflection at this boundary. Instead, when the groove is filled with an optically matched liquid, more of the scintillation light makes it into the fiber. A natural advantage of using a fiber in a liquid scintillator is that there will be no air gap between the fiber and the scintillator. However, the fiber and scintillator must be chemically compatible with each other, so that neither is degraded by contact.

The Fresnel equations (Eq. 3.7) give the fraction of S and P polarized light, R_s and R_p, incident at an angle of θ_i from a material of index of refraction n_1 that reflects off a surface of an index of refraction n_2.

$$R_s = \left[\frac{n_1\cos\theta_i - n_2\sqrt{1-(\frac{n_1}{n_2}\sin\theta_i)^2}}{n_1\cos\theta_i + n_2\sqrt{1-(\frac{n_1}{n_2}\sin\theta_i)^2}}\right]^2 \tag{3.7}$$

$$R_p = \left[\frac{n_1\sqrt{1-(\frac{n_1}{n_2}\sin\theta_i)^2} - n_2\cos\theta_i}{n_1\sqrt{1-(\frac{n_1}{n_2}\sin\theta_i)^2} + n_2\cos\theta_i}\right]^2$$

If n_1 and n_2 are close to equal, the fraction of reflected light is small.

As an example liquid scintillator, Eljen EJ-309 has an index of refraction of 1.57 [67], and the outer cladding of a double-clad Kuraray WLS fiber has an index

of refraction of 1.42 [68]. In the best-case scenario, in which a photon is normally incident on a fiber from a liquid scintillator, there is a probability of reflection at this interface of about 0.3%. However, this probability increases to 100% if the angle of incidence is above the critical angle (discussed below). The average probability of reflectance for angles in the range of $0-90°$ is about 30%. Photons that are reflected from the surface of a fiber may scatter in the opaque scintillator and return to the fiber surface, may reach another fiber, or may be absorbed and not detected.

3.2.2 Absorption and re-emission

If a photon reaches the core of a WLS fiber, it has a chance of being absorbed and wavelength-shifted. The core of the fiber is doped with a dye that operates in the same way as the wavelength-shifting compounds in bulk scintillators described above. The fibers are generally designed such that light within a specified band of wavelengths is efficiently absorbed. Fibers with various dye species and concentrations are available, but the fibers used in the experimental portion of this thesis were Kuraray Y-11(200) (non S-type) [69]. The Y-11 fibers use K27 dye, and the (200) refers to the dye concentration in ppm. K27 is a blue-to-green shifting dye with an absorption that peaks at about 430 nm. K27(200) has an absorption length of approximately 0.34 mm for the light of wavelength 430 nm [70]. For photons that are incident normally and travel through the central axis of the fiber (thus having a path length of 1 mm through the dye), only about 5% are not absorbed.

3.2.3 Light trapping and transport

Once a photon is absorbed and re-emitted in the core of a WLS fiber, there are two possible outcomes. First, the photon may escape the fiber and re-enter the scintillation liquid, in which case it is very unlikely to be detected. More preferably,

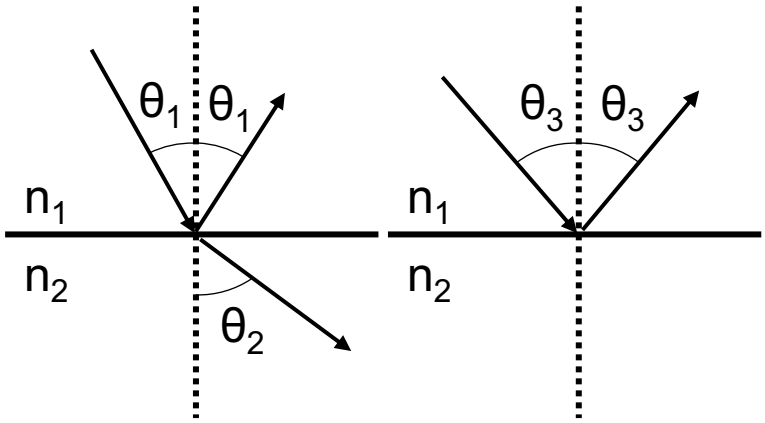

Figure 3.4: A sketch of reflection and refraction of a ray of light according to Snell's Law. The left panel shows a ray of light partially refracting from a medium with a higher index of refraction to a medium with a lower index of refraction. The right panel shows light incident on medium 2 at an angle greater than the critical angle; the light is reflected and not refracted.

the red-shifted photon may be emitted in the core of the fiber in a direction that results in reflection at a cladding boundary.

Snell's Law describes the angle of refraction for a photon moving from a medium with an index of refraction n_1 into a medium with an index of refraction n_2.

$$n_1 \sin(\theta_1) = n_2 \sin(\theta_2), \tag{3.8}$$

where θ_1 is the angle of incidence, measured from the normal, and θ_2 is the angle of refraction, as shown in Fig. 3.4.

In the case in which $n_1 > n_2$, there is an angle of incidence θ_c, known as the critical angle, for which the angle of refraction is 90°:

$$n_1 \sin\theta_c = n_2 \tag{3.9}$$

$$\theta_c = \sin^{-1}\frac{n_2}{n_1}. \tag{3.10}$$

All light incident on the surface at an angle less than the critical angle is reflected, a condition known as total internal reflection.

The probability that a photon emitted in the core of a WLS fiber meets the

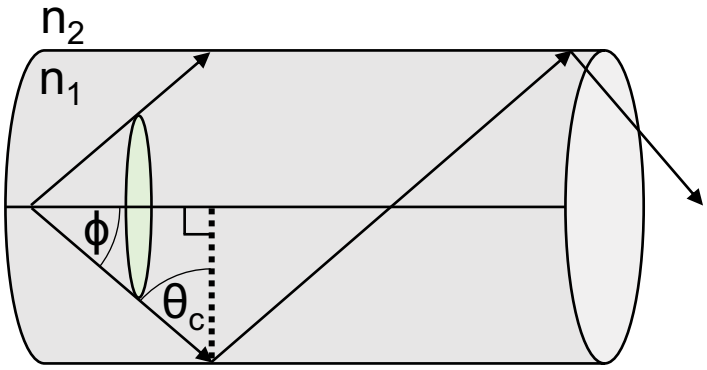

Figure 3.5: A sketch of the geometry of the path of a photon that originates on the optical axis of a fiber. The green region represents the fractional solid angle that results in total internal reflection.

condition of total internal reflection dictates the trapping efficiency of the fiber. A sketch of the geometry of this situation is shown in Fig. 3.5.

Following the analysis in Ref. [70], the solid angle that results in total internal reflection for rays that originate at the center of the fiber core can be expressed as

$$\Omega_c = \int_0^{2\pi} d\psi \int_0^{\frac{\pi}{2}-\theta_c} \sin(\phi) d\phi \tag{3.11}$$

$$\Omega_c = 2\pi(1 - \sin\theta_c) \tag{3.12}$$

$$\Omega_c = 2\pi(1 - \frac{n_2}{n_1}), \tag{3.13}$$

where ψ is the azimuthal angle. Generally, in opaque scintillators light is collected at both ends of the fiber, so the above result is multiplied by 2 and divided by the total solid angle 4π to calculate the fraction of the solid angle that results in total internal reflection:

$$\Omega_f = 1 - \frac{n_2}{n_1}. \tag{3.14}$$

To maximize this quantity, the ratio of the index of refraction of the core to the cladding should be as large as possible. A typical single-clad Kuraray fiber has a polystyrene core with an index of refraction of 1.59 and a polymethylmethacrylate

(PMMA) cladding with an index of refraction of 1.49. This gives a fractional solid angle of approximately 6.3%.

Most commercial wavelength-shifting fibers have two or three layers. A two-layer model consists of the fiber core sheathed by a cladding material, whereas a three-layer fiber has an additional outer cladding. While a three-layer fiber reflects more scintillation light into the scintillating fluid, it also retains up to 70% more light (compared to a similar two-layer fiber) in the core due to additional internal reflection [71]. The combined effect is that a three-layer fiber delivers up to 43% more scintillation light than a similar two-layer fiber [72].

Assuming the second layer of cladding has an index of refraction n_3, the angle of incidence from the core to the first layer of cladding θ_1 that would result in the critical angle of the second cladding $\theta_{2,c}$ is given by

$$n_1 \sin\theta_1 = n_2 \sin\theta_{2,c} \tag{3.15}$$

$$\theta_{2,c} = \sin^{-1}\frac{n_3}{n_2} \tag{3.16}$$

$$n_1 \sin\theta_1 = n_2 \sin\left(\sin^{-1}\frac{n_3}{n_2}\right) \tag{3.17}$$

$$n_1 \sin\theta_1 = n_2\frac{n_3}{n_2} \tag{3.18}$$

$$\theta_1 = \sin^{-1}\frac{n_3}{n_1}. \tag{3.19}$$

Therefore, the effective critical angle of the double-clad system is $\sin^{-1}\frac{n_3}{n_1}$ and does not depend on the index of refraction of the inner cladding. A typical outer cladding for a double-clad Kuraray fiber is made of a fluorinated polymer with an index of refraction of 1.42, which gives a fractional solid angle for a total internal reflection of about 10.7%. If the fiber were in the air, there would be additional angles of incidence that result in total internal reflection at the boundary between the air and the second cladding. However, most liquid scintillators have an index of refraction

greater than 1.42, so a WLS fiber immersed in a liquid scintillator does not exhibit additional trapping from reflection at this boundary.

In addition to meridional rays, skew rays – or rays that do not pass through the optical axis of the fiber – can result in total internal reflection. These rays have a helical path through the fiber and can have extremely long path lengths before reaching the terminus. The trapping efficiency for all emitted photons (including non-meridional photons) in a fiber was determined by Weiss in Ref. [73] to be $1-(n_3/n_1)^2$, which for the fiber described above would be about 20%. However, the contribution of the skew rays to the detected signal depends on the fraction of skew rays that arrive at the photon sensor before being absorbed and the efficiency of the photocathode in converting these highly oblique photons to photoelectrons. In WLS fibers, the bulk absorption length for re-emitted photons is on the order of several meters [69]. The interplay between these variables is sufficiently complex that the effective trapping efficiency for a given detector geometry is best found through Monte Carlo analysis.

3.3 Readout

For a photon to be detected, it must interact with a light sensor. In the experimental component of the work in this thesis, the type of photon sensor used is a multi-anode photomultiplier tube (MAPMT). The quantum efficiency of the MAPMT describes the probability that an incident photon undergoes photoelectric absorption at the photocathode and produces a free electron that is emitted in a direction that allows it to be multiplied and eventually read out as a voltage pulse. The typical quantum efficiency for the type of MAPMT used in this thesis is about 20% at 480 nm.

A silicon photomultiplier (SiPM) is a photon sensor consisting of many small

avalanche photodiode cells that each operate in Geiger mode. SiPMs can achieve a photon detection efficiency (PDE) as high as 50%.

3.4 Theoretical maximum efficiency

The probability that a photon created in an opaque scintillator is eventually be converted into an electrical signal at a photon sensor depends upon many factors. Speaking broadly, for a photon to be "detected" by a photomultiplier, the following must occur:

1. The photon must arrive at a fiber before being absorbed in the bulk liquid or at a partially reflecting boundary. In some cases, the photon may arrive at a fiber multiple times before being absorbed.
2. The photon must be transmitted through both layers of cladding into the fiber core, instead of being reflected or absorbed
3. The photon must be absorbed in the fiber core and not simply transported through it.
4. A new (wavelength-shifted) photon must be emitted in a direction relative to the fiber that results in total internal reflection at the core/cladding boundary. Because the WLS fibers are designed with a large Stokes shift, it is very improbable that a wavelength-shifted photon that escapes the WLS fiber in which it was emitted is reabsorbed again by the same or another fiber.
5. The photon must be transported through the fiber to the photon sensor without being absorbed or scattered out of the core. The path length of a photon is often multiple times the nominal length of the fiber.
6. The photon must be transmitted through the end of the fiber into the coupling grease and onto the photon sensor.

7. The photon must be converted to an electrical signal by the photon sensor and read out.

By estimating the maximum probabilities of each step above, one can approximate the highest possible detection efficiency of this type of detector.

In the case of a scintillation liquid with a very long absorption length, the fraction of photons that would eventually be absorbed in the core of WLS fiber would approach unity. Similarly, an optimally designed WLS fiber with an extremely long absorption length would deliver all trapped photons to the light sensor. As discussed in Sec. 3.2.3, the trapping efficiency of a typical double-clad fiber is approximately 20%, including skew rays. Lastly, the PDE of a SiPM of 50% yields an ideal total detection efficiency of 10%. While this estimate is likely at least an order of magnitude too high for a real-world detector, it gives an idea of the maximum theoretical efficiency that could be achieved with optimal materials.

More realistic determinations of these parameters and probabilities and the resulting total detection efficiency are provided in the chapters that follow.

CHAPTER IV

Evaluation of Light Collection From Highly Scattering Media Using Wavelength-Shifting Fibers

This chapter is based on an article published in 2023 in *Nuclear Instruments and Methods in Physics Research Section A* and co-authored by Prof. Igor Jovanovic, Garrett Wendell, Brandon Collins, and Prof. Doug Cowen [74].

The work presented in this chapter serves to quantify the parameters and probabilities discussed in Ch. III for a specific set of WLS fibers and MAPMT. Further, the Monte Carlo simulation of opaque scintillators is experimentally validated and is used to understand the performance of the prototypes described in Chs. V and VI.

4.1 Introduction

All radiation detectors rely on the interaction of incident particles with matter, where the kinetic energy of primary or secondary particles is deposited in the instrumented detector volume. In scintillation detectors, a fraction of the energy deposited by the interacting particle is emitted as light, which is then converted into an electrical signal via a photosensor such as a photomultiplier. The photosensor is usually placed outside the active volume, near its boundary. In this case, the scintillation medium should be as transparent as possible so that the maximum fraction of generated light reaches the boundary and is detected by the photosensor. A scintillation

photon often scatters or reflects multiple times at non-sensing detector boundaries before reaching the photosensor and, thus, the information available for position reconstruction in the detector's active volume may be severely degraded or even entirely lost. The locations of energy deposition within a detector volume arising from a single quantum of incident radiation are referred to collectively as the "event topology."

The measured event topology in a radiation detector can be leveraged to infer the direction of origin of a radiation source [75] and to identify the type of interacting particle [76]. There are several ways to obtain event topology in a scintillation detector. One method is to optically isolate segments of the detector, each of which then functions as a pixel [20, 77]; another is to use relative time-of-arrival of the optical photons at multiple photosensors, which is often employed in large detectors [78] and in applications that require excellent timing resolution, such as Positron Emission Tomography (PET) [79].

LiquidO [24] has been proposed as a method to localize scintillation photons by designing the detection medium to have a short scattering length, thus achieving virtual pixelization without the need to highly segment the detector volume. A scintillation photon travels only a short distance between scatters such that it is *stochastically confined* [24]. A challenge in using an opaque scintillator is that the light must be eventually extracted from the detection volume so that it can be sent to a photosensor and converted into an electrical signal. This can be achieved using a lattice of wavelength-shifting (WLS) fibers. Scintillation photons are absorbed in the core of a WLS fiber and are isotropically reemitted with a longer wavelength, such that some of them meet the criterion for total internal reflection. A photon captured in this manner can be transported through the fiber to the photosensor.

Event topology can then be reconstructed from the relative amount of light collected in multiple fibers that traverse the region near the origin of scintillation.

An ideal opaque scintillator has a high light yield, a short scattering length, and a long absorption length. Liquids with the latter two characteristics in the visible range appear white and milky or waxy. Currently, at least two materials are under consideration for LiquidO applications: (1) NoWaSH, which is a mixture of linear alkyl benzene (LAB) and paraffin that reduces the scattering length [27] and (2) water-based liquid scintillator (WbLS), which can be tuned to have the desired optical properties [80, 81]. Additionally, a scintillator with desired LiquidO properties may be created by adding nanoparticles (*e.g.*, TiO_2) to a traditional liquid scintillator, though the stability of such a compound remains to be demonstrated.

To design a LiquidO detector, an accurate model of light transport in the medium and collection into the fibers is required. In this work, the efficiency is measured with which the light emitted by a highly scattering medium is collected by WLS fibers. This data is used to validate a Geant4 [46] model for the experiment, which offers the prospect of predicting the performance of future LiquidO detectors.

4.2 Experiment

To measure light collection efficiency from an opaque liquid into WLS fibers as a function of the distance between the light source and fiber, the precise origin of the light must be known. To achieve this, an inert (*i.e.*, non-scintillating) liquid is used, and the light is injected at a known position using a fiber-coupled pulsed laser. This allows the control of both the location of emission and the intensity of light in the opaque medium. Additionally, since the time of arrival of laser pulses is known with great accuracy, the effect of spurious pulses arising from various backgrounds in this

measurement can be greatly reduced.

For this study, we chose to use dilutions of commercial cow milk as the opaque, non-scintillating liquid. Milk has several salutary properties, one of which is that it has a longer absorption length than scattering length for the wavelengths of light under consideration [82]. Another is that milk is water soluble, which means that its optical properties can be easily tuned by mixing it with distilled water. Additionally, milk is readily available and inexpensive. Another candidate liquid was a TiO_2-water nanofluid. However, in addition to agglomeration, TiO_2-water nanofluids suffer from sedimentation over time, at rates up to 5% in an hour [83]. Another attractive option is Intralipid, which has consistent optical properties batch-to-batch, stability on the timescale of years, and high scattering and low absorption [84]. However, it is much more expensive than milk.

4.2.1 Apparatus

A schematic of the experimental setup is shown in Fig. 4.1. The experiment was conducted in a light-tight box (shown in Fig. 4.2). The container for the liquid was a 2-gallon, high-density polyethylene (HDPE) bucket.

The light source was a pulsed diode laser from NKT Photonics, operating at 407 nm. The pulse duration is approximately 35 ps, and the output power is tunable. The laser was coupled to a single-mode fiber after passing through neutral-density filters to attenuate it. In this experiment, the laser operated at 10 kHz, such that each pulse contained approximately 18,000 photons after attenuation using the neutral density filters. The laser power was measured before each experimental run using a Thorlabs PM101 power meter.

The WLS fibers used were 1 m sections of Kuraray Y-11(200) (non-S type). One end of each fiber terminated at the bottom of the vessel, with a gap of 10±3 mm

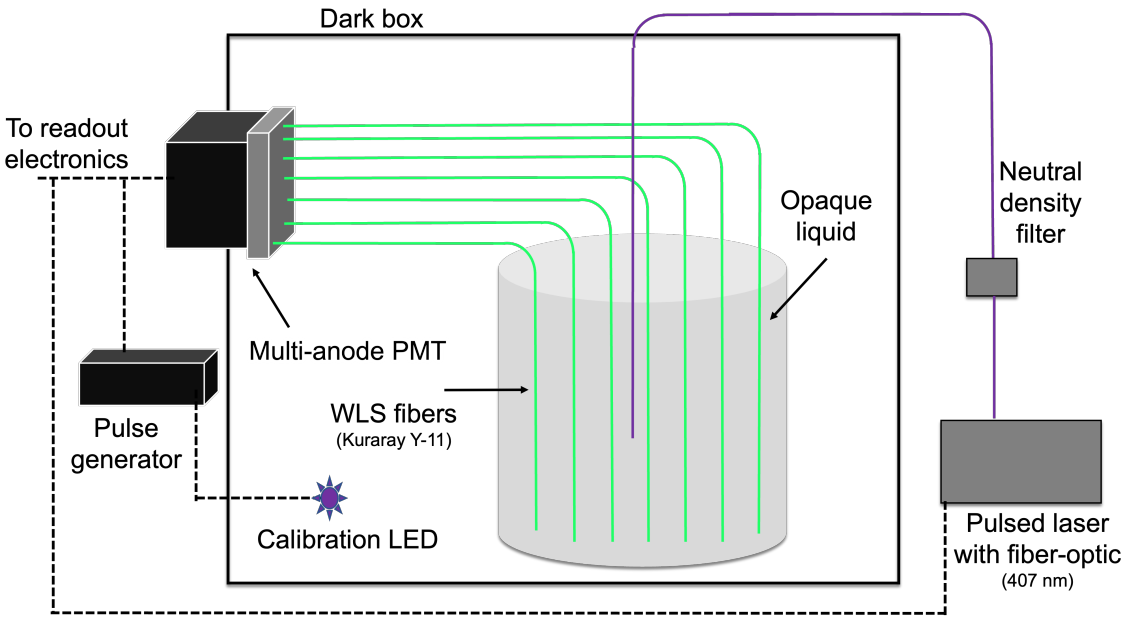

Figure 4.1: A sketch of the experimental apparatus. The dashed interfaces are electrical, and the solid ones are optical. The data acquisition system is triggered by the pulse generator during calibration and by the laser controller during experiments with laser pulses.

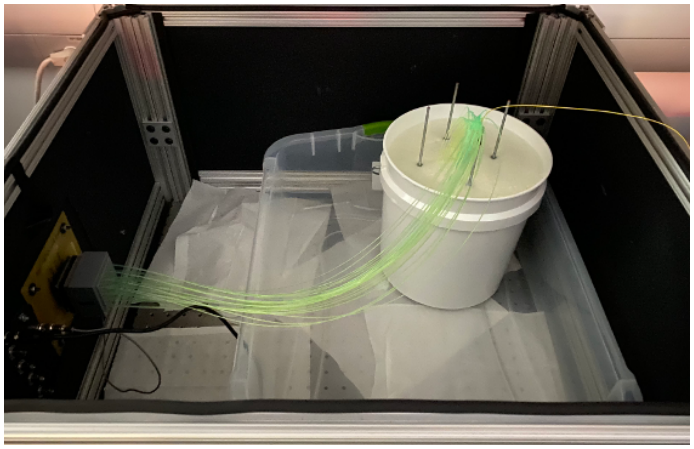

Figure 4.2: The experimental apparatus inside a dark box. The yellow-jacketed fiber carries the light from the pulsed laser to the center of the fiber array, which is submerged in 7500 ml of opaque liquid. The fibers emerge from the liquid and terminate at individual pixels of the MAPMT.

to reduce reflections back into the fiber. The other end was coupled to a pixel of a Hamamatsu H12700A multianode photomultiplier tube (MAPMT). Each fiber end was cleaved using a Comptyco KPT-130 High Precision Cleaver and then polished using a series of sandpapers with 1000–4000 grits. Consistent contact between the fiber and photocathode was achieved using optical grease. The H12700A has 64 pixels, but only 32 pixels were used in a checkerboard pattern to reduce cross-talk between neighboring channels. The MAPMT was biased at -1100 V, and the waveforms were digitized with two CAEN V1730 boards. Pulse integration was done onboard the V1730s using DPP-PSD firmware with an integration window of 256 ns. This was longer than necessary, as the decay time of the WLS fibers is 7.4 ns [85]. The digitizer was triggered with a signal from the laser controller, regardless of whether a voltage threshold in that channel was met. As a result, there were often no photoelectrons measured in a given integration window. This approach enabled the determination of the average number of photoelectrons per pulse for each MAPMT pixel.

The fibers were held in place by a 3D-printed fixture; four fibers at 90° angular intervals were placed at each set distance from the center to provide redundant sampling. The apparatus had a 0.2 mm diameter nylon monofilament suspended vertically in the center of the volume. The single-mode fiber that carried the laser light was affixed to this central monofilament such that the light was injected into the center of the array. The first set of WLS fibers was placed 2 ± 1 mm from the center (the location of light injection), after which each additional set of fibers increased in distance from the center by 4 ± 1 mm. Each arm of the fiber array held 8 WLS fibers, at distances of 2, 6, 10, 14, 18, 22, 26, and 30 mm from the center of the volume. The fiber holder array is shown in Fig. 4.3.

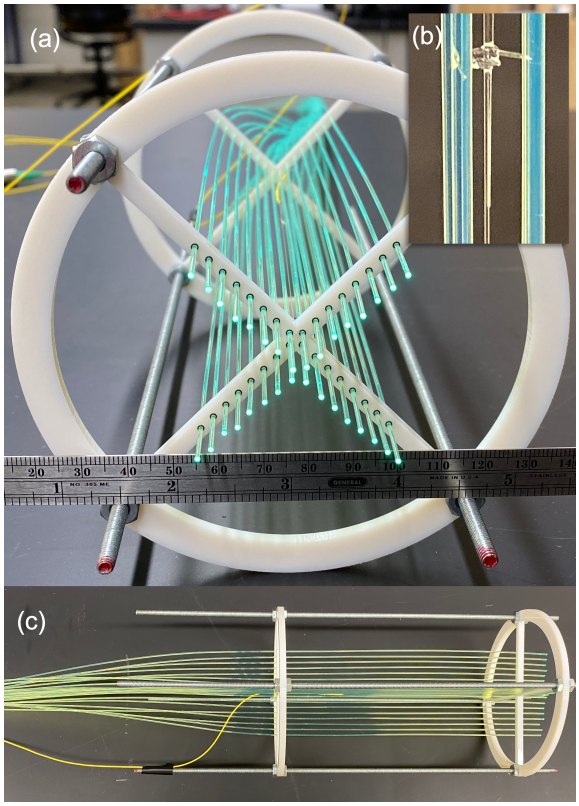

Figure 4.3: Views of the fiber holder with WLS fibers from (a) bottom and (c) side. The end of the laser-coupled single-mode fiber is shown in (b). A 0.2 mm diameter nylon monofilament is suspended vertically in the center of the array. The single-mode fiber (ThorLabs SM300) is secured to the nylon monofilament by a small knot, made of more nylon monofilament, to maintain the central positioning of the light source.

4.2.1.1 Calibration

To determine the number of photoelectrons produced at the photocathode per integration window, the MAPMT by-pixel single photoelectron response was measured. Before each experimental run, four calibration measurements were made with varying intensities of light from a pulsed LED. The first measurement was a background measurement, in which the signal from a pulser only served to trigger the digitizer. The pulser signal was also used to drive a 400-nm LED with a pulse width of 3 ns at voltages of 3.5, 3.7, and 3.9 V. The LED was positioned in a corner of the dark box so it was as far away from the WLS fibers as possible but within direct view of the portion of the WLS fibers that span between the opaque liquid vessel and the MAPMT. In all cases, the light was incident upon the WLS fibers, which were each coupled to their assigned MAPMT pixel. The resulting four pulse integral spectra were simultaneously fitted according to the method described in Ref. [86]. The fitting algorithm determines parameters that describe the response of each MAPMT pixel to zero photoelectrons (pedestal charge) and single photoelectrons. These parameters were then applied to the pulse integral spectra. Four other parameters, including scaling, two noise parameters, and the average number of photoelectrons per pulse, were allowed to vary. The fitting algorithm was then applied to the experimental run data, and the average number of photoelectrons per pulse was recorded. Example calibration spectra and fits are shown in Fig. 4.4, and the final fit to data from an experimental run is shown in Fig. 4.5.

4.2.2 Results

A predicted feature of LiquidO is that light collection can increase with increased scattering for photons that originate close to the WLS fibers. To demonstrate this

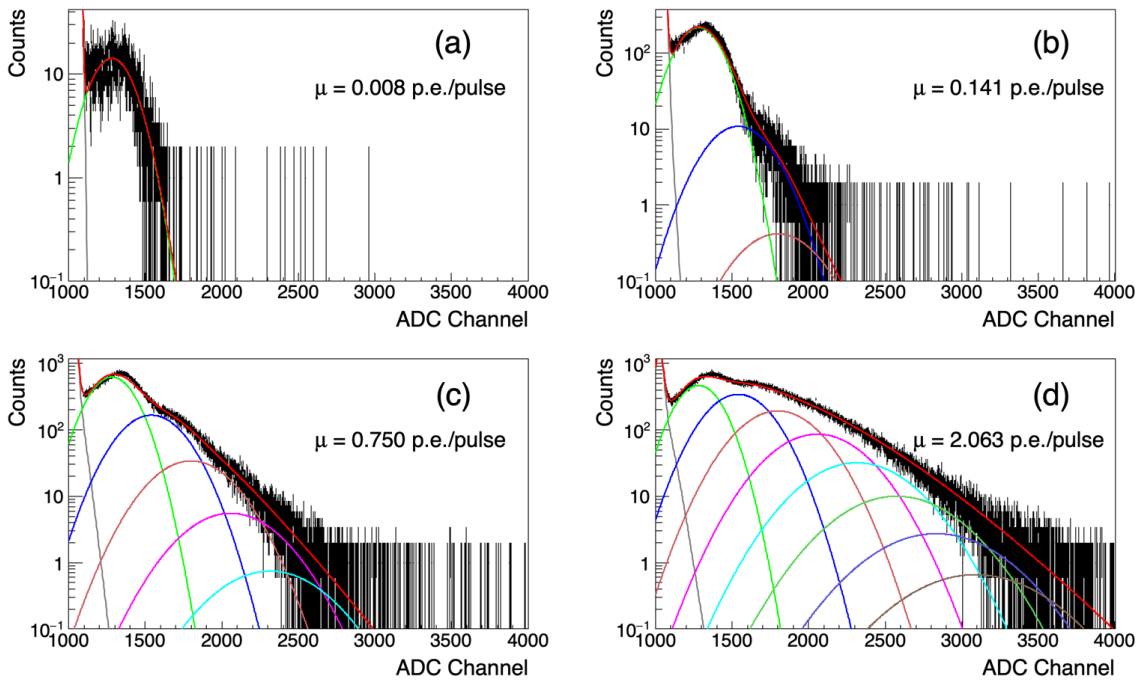

Figure 4.4: The pulse integral spectra from an example channel of the MAPMT during calibration are shown on a semi-log scale. A constant pedestal charge of 1024 ADC channels was added to aid the fitting process. (a) is the background, while (b)–(d) shows the response to increasing light intensity from a pulsed LED. In each plot, the red line is the overall fit, while the other colors show the contributions from a single photoelectron (green), two photoelectrons (blue), *etc* (see text for details). The value μ shown in each plot is the average photoelectrons per pulse, which was a fitted parameter.

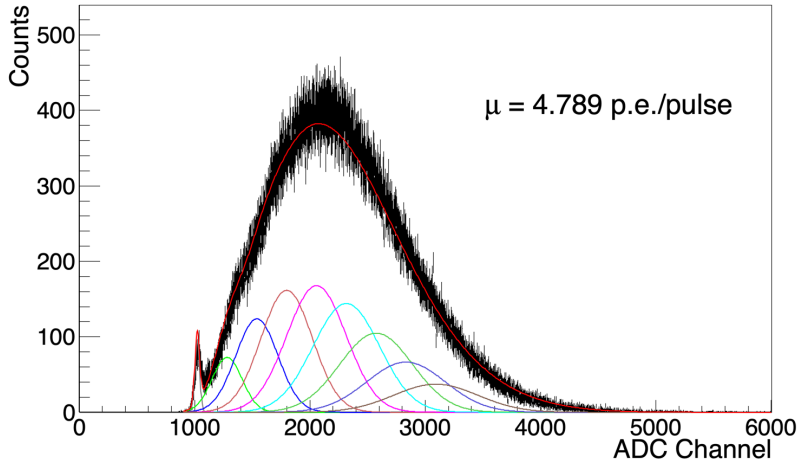

Figure 4.5: Experimental data from the same channel as in Fig. 4.4, fit with the parameters found during calibration. The red line is the overall fit, while the other colors show the contributions from events in which an increasing number of photoelectrons was produced. While the events of up to 12 photoelectrons are included in the fitting function, only 8 are shown for clarity. The parameter μ represents the average number of photoelectrons per pulse.

experimentally, photons were injected roughly 0.1 mm from the outer cladding of a WLS fiber. The photons were emitted from a single-mode fiber that was coupled to the pulsed laser described in Sec. 4.2.1. The laser was tuned to provide 17,600±900 photons/pulse. The single-mode fiber was parallel to the WLS fiber, such that few photons were incident on the WLS fiber without first being scattered. This was a different arrangement than that shown in Fig. 4.3. Instead of being mounted in the center of the array, the fiber carrying the laser light was affixed directly to the side of a WLS fiber. The experimental data are presented in Fig. 4.6 for various dilutions of 0% fat content (skim) milk, which is used as the scattering medium. To avoid perturbing the fiber arrangement, the fiber array was not removed from the vessel between iterations of the experiment with different dilutions. Instead, the liquid was siphoned from the volume and replaced with distilled water to increase the dilution. The new mixture was then stirred for 60 seconds with a stirring rod spun by an electric drill. As expected, the light collected in the fiber increases with milk concentration. The Spearman correlation coefficient for the data presented in Figure 4.6 is 0.70 ± 0.26, which indicates a strong relationship [87]. As the concentration increases, the scattering length of the medium decreases, and more photons are confined to the region near the WLS fiber and collected. As the scattering length decreases, the absorption length also decreases; however, light collection efficiency still increases. Although the average path length of the photons decreases with a higher milk concentration, a greater fraction of that path is in the vicinity of the fiber, which increases the probability of collection.

To measure the light collection efficiency into WLS fibers as a function of distance from the light source and bulk liquid opacity, the apparatus described in Sec. 4.2.1 was used. The opaque liquid used was a dilution of homogenized, commercial, 2%

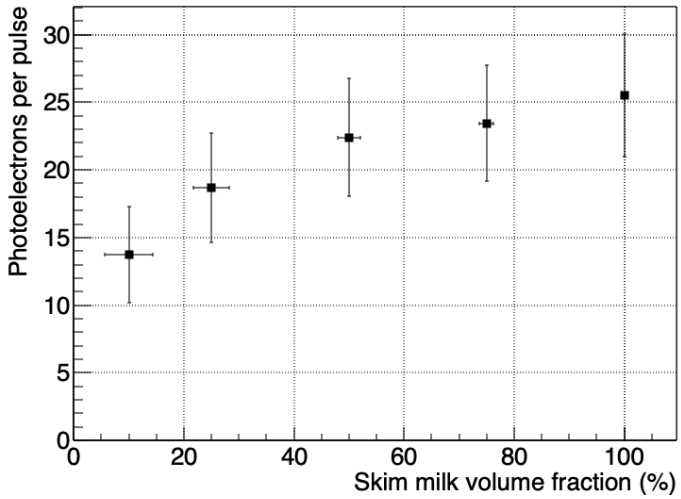

Figure 4.6: Photoelectrons detected per pulse from photons collected in a WLS fiber closest to the location of light injection. The first iteration of the experiment was done with 100% cow skim milk, and then the liquid was replaced with distilled water to dilute the milk. The uncertainty in the reconstructed number of photoelectrons per pulse is derived from the uncertainty of the fitting algorithm described in Sec. 4.2.1.1.

fat cow milk. The dilutions given are volumetric mixtures with distilled water, (*e.g.*, a 15% dilution means the mixture was 85% distilled water by volume). The laser power for this experiment was 17,900±900 photons/pulse. As discussed in Sec. 4.2.1, there were four fibers at each distance from the center of the fiber array. The number of photoelectrons per pulse was averaged at each position, and the uncertainty was taken to be the standard deviation of these four measurements. The results are shown in Fig. 4.7. Similarly to what was shown in Fig. 4.6, the collection efficiency increased with higher concentrations of milk, (*i.e.*, more scattering) for the fiber closest to the light source. Additionally, light collection at distances far from the light source was systematically suppressed by the increased light scattering in higher milk concentrations. This highlights the localization of optical photons and, therefore, the potential for determining the location of origin of the emitted light.

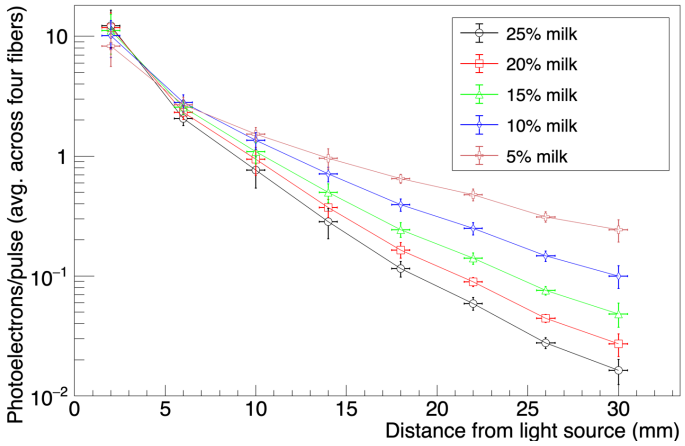

Figure 4.7: Photoelectrons per pulse from photons collected in WLS fibers at various distances from the light source for a variety of dilutions of commercial, 2% fat cow milk. Each pulse of light contained 17,900±900 photons.

4.3 Modeling

4.3.1 Monte Carlo

The Geant4 model includes the HDPE vessel, the opaque liquid, and the multi-clad WLS fibers in their appropriate locations. Geant4 has a built-in wavelength-shifting process, which requires user-defined absorption and emission spectra. The relevant parameters used in the Geant4 model are summarized in Table 4.1. The fibers were modeled to have perfectly smooth surfaces, such that reflection and refraction probabilities depended only on solutions to the Fresnel equations given the relative indices of the refraction of the materials in contact. Cow milk is a complex

Table 4.1: The material properties used to construct the Geant4 model.

Parameter	Value	Reference
Index of refraction (Y-11 outer cladding)	1.42	[69]
Index of refraction (Y-11 inner cladding)	1.49	[69]
Index of refraction (Y-11 core)	1.59	[69]
WLS absorption length	See Fig. 4.8	[70]
WLS emission spectrum	See Fig. 4.8	[88]
Y-11 bulk absorption length	See Fig. 4.9	[89]
MAPMT quantum efficiency	See Fig. 4.9	[90]
Reflectivity of HDPE (vessel)	0.9	[91]

liquid, with a variable particulate size that depends on fat content, homogenization

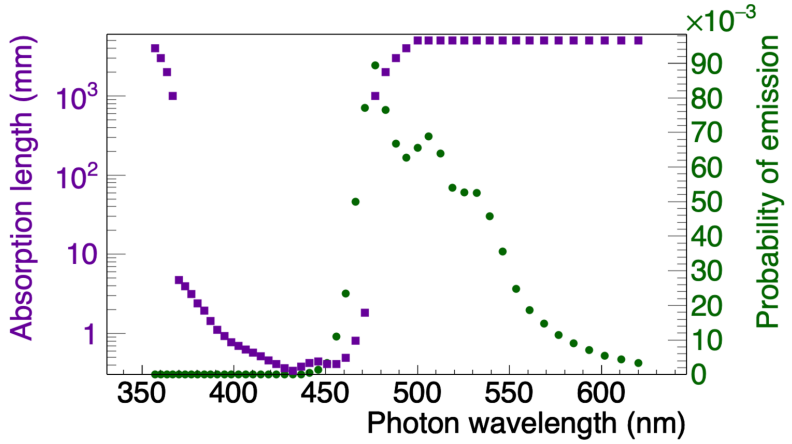

Figure 4.8: Kuraray Y-11 WLS absorption (purple squares) and emission (green circles) spectra used in the Geant4 model. WLS absorption results in a new optical photon with a wavelength sampled from the emission distribution and a randomized direction.

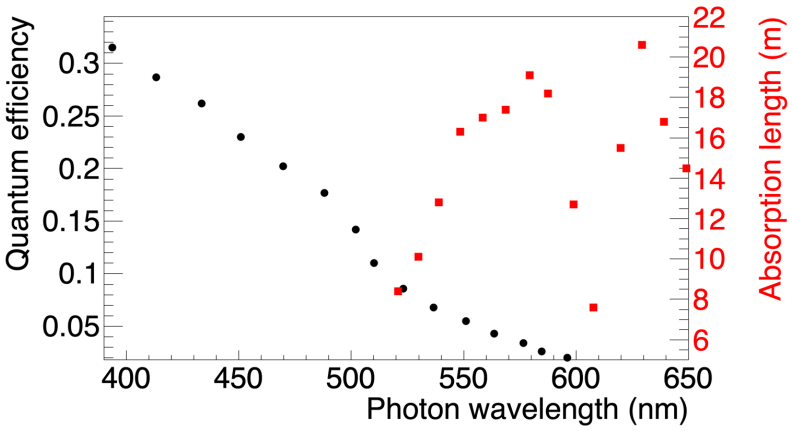

Figure 4.9: Quantum efficiency (black circles) of the Hamamatsu H12700A and the bulk absorption length of the Kuraray Y-11 fiber (red squares) used in the Geant4 model. Bulk absorption is a separate process from WLS absorption in Geant4 and cannot result in the emission of a new optical photon. The dip in the absorption length around 610 nm is due to a resonance in the absorption cross-section characteristic to WLS fibers with a polystyrene core [89]

process, and many other factors. Typical commercial cow milk has a sufficiently large average particle size for Mie scattering at visible wavelengths [82]. Mie scattering is generally more forward-directed than Rayleigh scattering, which is the approximation for the scattering of photons off of spherical particles that are small in comparison to wavelength. Another way to account for this anisotropy is to use the reduced scattering coefficient μ_s':

$$\mu_s' = \mu_s(1 - g). \tag{4.1}$$

Here, μ_s is the scattering coefficient with units of inverse length, and g is the average cosine of the scattering angle; $g = 1$ indicates total forward scattering, while $g = 0$ represents isotropic scattering. Similarly, the reduced scattering length is

$$\lambda' = 1/\mu_s' \tag{4.2}$$

and has units of length.

The Geant4 framework incorporates the Mie and Rayleigh scattering physics, but only Rayleigh scattering was used because an accurate accounting for Mie scattering requires the knowledge of the particle size distribution, which is unknown for the used milk samples. Geant4 does not allow the specification of an anisotropy parameter, so the reduced scattering length was used in place of the scattering length. The reduced scattering length and absorption length were treated as free parameters obtained from the fit of the model to the experimental data (see Sec. 4.3.1.)

Since the number of photoelectrons per pulse is measured in the experiment, the objective is for the model to output results in the same units. To this end, the probability of a photon creating a photoelectron at the photocathode of the MAPMT was included. The primary particle in our simulation is a 407-nm optical photon. To result in a photoelectron count for a given channel, the optical photon has to enter

a WLS fiber, be refracted through the cladding, absorbed in the core, and reemitted in a direction conducive to total internal reflection. The photon then has to be transported through the 1-m long fiber, during which it could be absorbed by the fiber core. At the end of the fiber, the photon undergoes conversion to photoelectron at the photocathode with a quantum efficiency that depends upon its wavelength. The values for the wavelength-dependent quantum efficiency were taken from the manufacturer's datasheet and are shown in Fig. 4.9.

The optical parameters of an actual candidate LiquidO media should be well-characterized before prototyping. However, as the determination of the optical parameters of the milk samples was not the purpose of this study, no direct measurement was made. Instead, to find the best-fit parameters for the reduced scattering length and absorption length of the milk sample, measurements were made at a series of dilutions. The absorption coefficient $\mu_{a,c}$ of a compound can be calculated from

$$\frac{\mu_{a,c}}{\rho_c} = \sum_i w_i \frac{\mu_{a,i}}{\rho_i}, \tag{4.3}$$

where ρ is the density of the material, and w_i is the fraction of the ith material by mass. The reduced scattering length can be calculated analogously under the assumption that the particle size distribution is unaffected by concentration. The validity of this assumption is discussed below.

In the parameter search, a combination of reduced scattering and absorption lengths for pure milk was chosen, the resulting parameters were calculated, and a simulation was run for each dilution. The total weighted sum of squared errors (WSEE) was then calculated:

$$\text{WSSE} = \sum_{i=1}^{8} \frac{1}{\sigma_i^2}(y_{i,\text{sim}} - y_{i,\text{exp}})^2, \tag{4.4}$$

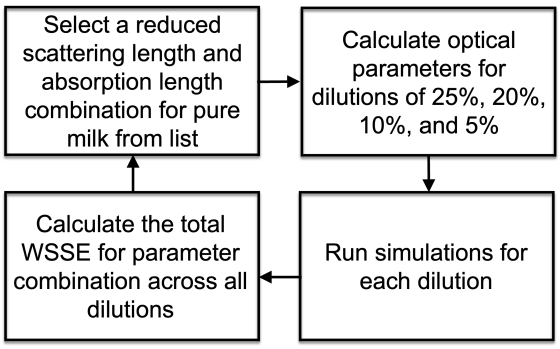

Figure 4.10: A flowchart of the parameter search process to determine the optical parameters of pure milk.

where σ_i is the uncertainty of the measurement at the ith distance from the light source, and $y_{i,\text{sim}}$ and $y_{i,\text{exp}}$ are the average numbers of photoelectrons from the four fibers at that distance from the light source in the simulation and experiment, respectively. The values of parameters were pre-selected at regular intervals such that the search comprised a grid. This process is shown as a flowchart in Fig. 4.10.

The dataset from 15% dilution was withheld from the fitting for validation. The results of the parameter search are shown in Fig. 4.11. The parameter combination with the lowest total error (31.7) is a reduced scattering length of 0.75 mm and an absorption length of 8 mm.

The comparison between experimental and simulated data for these parameters is shown in Fig. 4.12. The χ^2 values are 26.3, 2.4, 11.3, and 13.6 for concentrations of 25%, 20%, 10%, and 5%. The fits are best for concentrations of 20% and 10%, and worst for concentrations of 25% and 5%. The particle size distributions for dilutions of milk above 10% are inconstant, which introduces nonlinearity into the rate at which the reduced scattering length changes with concentration [92]. One study found a measurable departure from reduced scattering length linearity in milk concentrations above approximately 0.6% [93]. The best overall fit found by our parameter search approximates an average for the particle size distribution, which

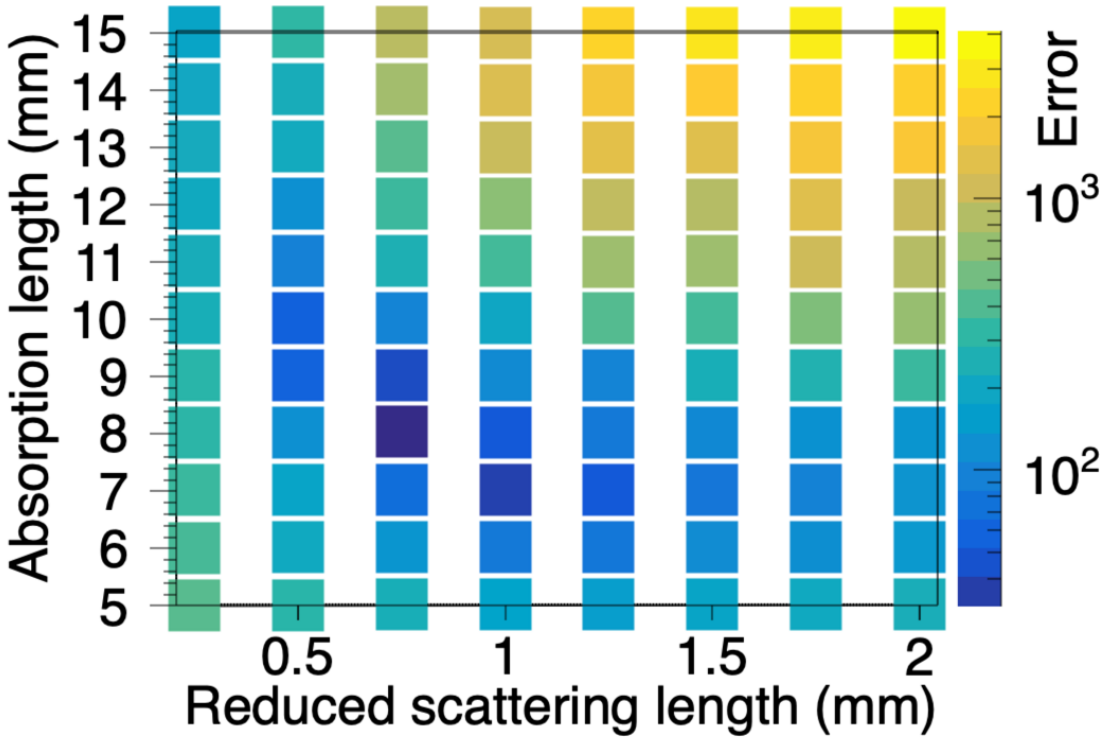

Figure 4.11: The total WSSE values for combinations of scattering and absorption parameters for simulation and experimental data. The total WSSE is the individual WSSEs from the 25%, 20%, 10%, and 5% dilutions of 2% milkfat commercial milk datasets, added in quadrature. The minimum error was 31.7, at a reduced scattering length of 0.75 mm and an absorption length of 8 mm.

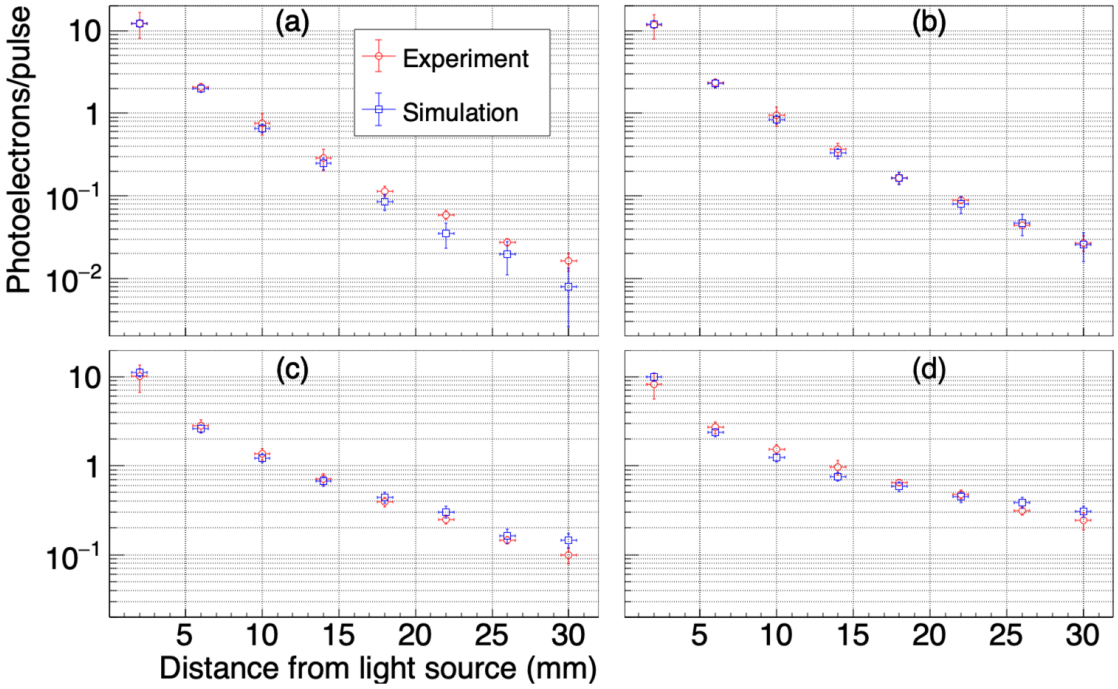

Figure 4.12: Comparison of simulated and experimental results for (a) 25% milk, (b) 20% milk, (c) 10% milk, and (d) 5% milk. All simulated values agree with the experiment within uncertainty. The optical parameters used for pure milk were optimized as shown in Fig. 4.11. Note that the vertical scale for (a) and (b) differs from the scale for (c) and (d).

likely explains why the fits degrade in quality away from the average concentration.

As a validation of the selected optical parameters, the dataset for 15% milk dilution (which was omitted from the parameter search) was compared to the simulation; the results are in Fig. 4.13. The data shows good agreement ($\chi^2 = 9.0$) with simulation at all distances from the origin. Summing the χ^2 values from all five datasets gives a χ^2 value of 62.5, which corresponds to a reduced χ^2 of 1.60, and a p-value of 0.013. The origin of the low p-value is likely the effect described above; a departure from linearity in the reduced scattering length of milk as a function of concentration is expected for the range of dilutions used in this experiment.

Ref. [94] measured the absorption and reduced scattering lengths for 2.44% fat cow milk in the wavelength range of 530–900 nm. Extrapolating their data to 407 nm

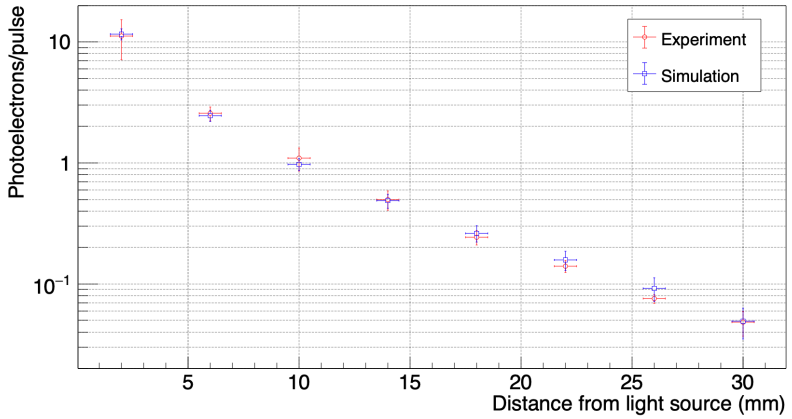

Figure 4.13: The comparison of simulated and experimental results for 15% milk dilution. The optical parameters for milk used were the same as shown in Fig. 4.12.

gives an absorption length of approximately 7 mm and a reduced scattering length of 0.8 mm, very close to the values obtained from the fit to experimental data. Ref. [82] found that the reduced scattering length of whole cow milk at 400 nm can vary in the range of 0.3–1.0 mm depending on homogenization time, and the absorption length at 400 nm is as high as 40 mm for 1.5% milkfat.

4.3.2 Diffusion Approximation

LiquidO-type detectors are characterized by a bulk medium with a short scattering length and long attenuation length. Within this medium, there is an array of wavelength-shifting fibers acting as photon sinks. These detector requirements provide conditions for diffusion calculations to approximately describe photon dynamics in the system and provide verification of the Monte Carlo model.

The diffusion equation can be derived by simplifying the Boltzmann transport equation; this is common in modeling neutron transport [95]. One can assume photon flux to be linearly anisotropic, photon current varies slowly compared to mean collision time, and the sources are isotropic. This can be physically realized in a LiquidO detector by spacing fibers and sources many scattering lengths apart on a

uniform grid.

Here, the aim is to predict the probability of photon capture in the WLS fiber given an initial photon distribution. Three processes the photon may undergo are of concern: scattering in the bulk medium, absorption in the bulk medium, and absorption in the fibers. Two equations describe two groups of photons; the first tracks a photon density in the bulk medium, while the second tracks the absorbed photon density in the wavelength-shifting material:

$$\frac{\partial \rho_m}{\partial t} = \nabla \left[D \nabla \phi_m \right] - \frac{\phi_m}{\alpha_m} - \frac{\phi_m}{\alpha_f}, \tag{4.5}$$

$$\frac{\partial \rho_f}{\partial t} = \frac{\phi_m}{\alpha_f}, \tag{4.6}$$

$$D = \frac{1}{3(\alpha_m^{-1} + \alpha_f^{-1} + \sigma_m^{-1})}. \tag{4.7}$$

Here, ρ_m and ρ_f are photon densities in the bulk material and WLS fiber, respectively, and ϕ_m is the photon flux in the medium. The material properties pertinent to the model are α_m, the mean free path to absorption in bulk material, α_f, the mean free path to absorption in WLS fiber, and σ_m, the mean free path to scattering in bulk material. Finally, t is time, and D is the diffusion coefficient.

Using the speed of light in the medium, one can replace $\phi = \rho c/n$ and rewrite the coupled diffusion equations entirely in terms of photon density. Assuming $n_{\text{fiber}} \approx n_{\text{medium}}$, we have:

$$\frac{\partial \rho_m}{\partial t} = \frac{c}{n} \left(\nabla \left[D \nabla \rho_m \right] - \frac{\rho_m}{\alpha_m} - \frac{\rho_m}{\alpha_f} \right) \tag{4.8}$$

$$\frac{\partial \rho_f}{\partial t} = \frac{c}{n} \frac{\rho_m}{\alpha_f}; \tag{4.9}$$

where c is the speed of light in vacuum, and n is the medium's index of refraction.

To verify the Monte Carlo simulation, a uniform square grid of WLS fibers is generated with a pitch of 15 mm, a scattering length of 1 mm, and an absorption

length of 50 mm for the bulk medium. An isotropic source is placed at the center of this square array of fibers. The Eq. (4.8) is solved for this geometry using pypde, a library implementing the finite difference method [96]. The mesh size of the simulation was set to 0.05 mm, an order of magnitude smaller than the absorption length of the fibers. Von Neumann stability analysis [97] is used to determine an upper bound on Δt for the numerical stability of the solution:

$$\Delta t \leq \frac{n}{2Dc}\left(\frac{1}{(\Delta x)^2}+\frac{1}{(\Delta y)^2}\right)^{-1} \approx 6 \text{ fs}, \tag{4.10}$$

where Δx and Δy are the mesh sizes in the x and y directions. To increase computational efficiency, two types of symmetry are leveraged in the detector model. First, the detector is homogeneous in the axial direction, and the medium boundaries are many absorption lengths away from the source, allowing one to treat the detector as infinite. Since the photon distribution along the axis of the fiber is of less interest, one can incorporate this symmetry by solving the diffusion equation in two dimensions. Second, the detector and source contain symmetries of the dihedral group D_4. Of the eight symmetries available, four are used by modeling one quadrant in the x-y plane with Neumann boundaries at the quadrant boundaries. The last set of symmetries could be implemented by slicing each quadrant diagonally through the origin, but this symmetry is not considered due to the increased complexity of implementation.

For the square grid geometry, the probability of each WLS fiber absorbing a photon is simulated using both the diffusion and Monte Carlo models. The results for each are shown in Fig. 4.14; they agree within 11% for the diffusion and Monte Carlo simulation for each fiber.

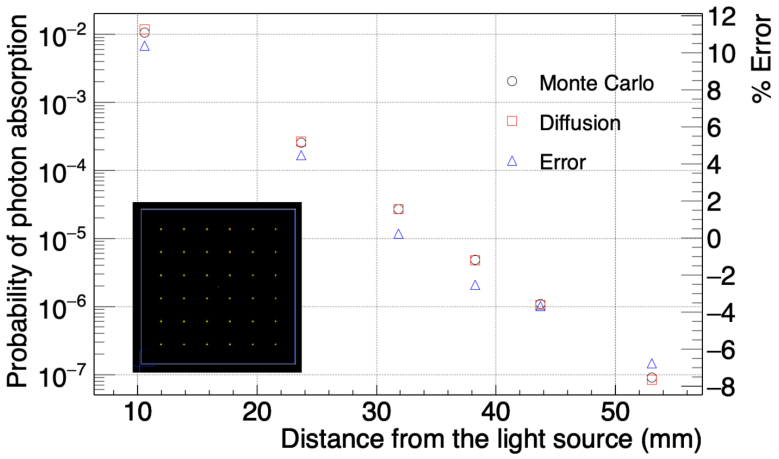

Figure 4.14: Photon absorption probabilities for a square grid array of WLS fibers with a fiber pitch of 15 mm simulated using the diffusion approximation and Monte Carlo. The inset shows a visualization of the geometry in Geant4. The two simulation methods perform within 15% of each other at each fiber.

4.4 Extension of model to low-absorption medium

The results described in this study pertain to dilutions of cow milk, which was chosen because it is readily available, water-soluble, and highly scattering. However, the relatively short absorption length of <10 mm means that the overall efficiency of photon collection is poor. In contrast, NoWASH can be created with an absorption length of above 2 m, while still maintaining a scattering length of below 1 mm [27]. WbLS has an even longer absorption length of tens of meters [98], but measurements of the scattering length for opaque WbLS have not yet been carried out.

As an illustration of the efficiencies possible in a real detector with desirable optical properties, the simulation from Sec. 4.3.1 was repeated with a reduced scattering length of 0.5 mm and an absorption length of 5 m, with a single WLS fiber at each distance from the origin. The light collection was also modeled at both ends of the WLS fibers instead of only one end as in the experiment; the results are shown in Fig. 4.15. In this instance, the fiber 2 mm from the light source produces approximately 0.0077 photoelectrons for each incident photon. WbLS with a 10%

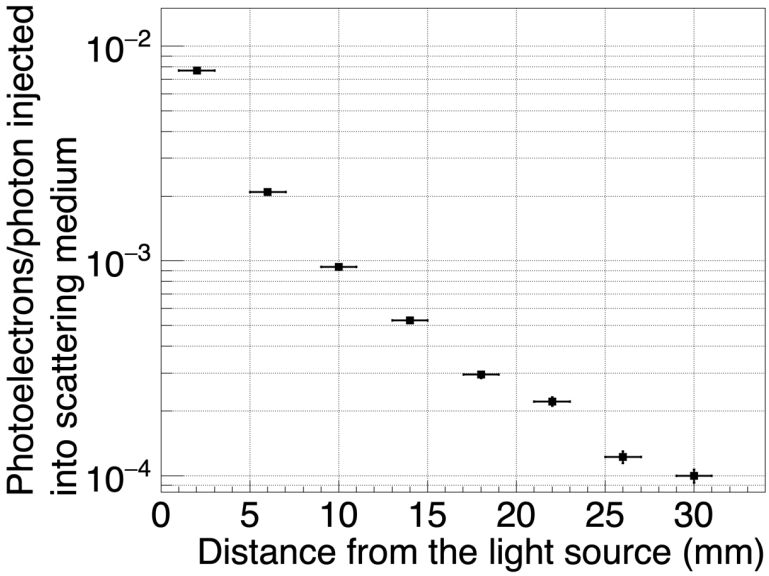

Figure 4.15: Simulated efficiency of light collection possible in an opaque liquid with a 5 m absorption length and a 0.5 mm reduced scattering length. The plot shows the number of photoelectrons detected per photon injected into the system and includes losses in transport in the bulk medium, collection in the WLS fiber, and conversion at the photocathode.

loading of LAB-PPO has a light yield of 1357±125 photons/MeV [81]; therefore, an event that deposits 1 MeV of energy 2 mm from a WLS fiber in 10% loaded WbLS with the optical parameters discussed above could be expected to produce about 10 photoelectrons, which is readily detectable in this experiment. The efficiency would be further increased by instituting a lattice of WLS fibers, such that light was collected from a single event in multiple fibers. Additionally, the MAPMT could be substituted for a silicon photomultiplier (SiPM) which can have a higher quantum efficiency, though at a cost of increased dark noise at room temperature. However, this is an extension of the model to conditions that were not directly experimentally validated. While the basic physics is unchanged for shorter scattering lengths and longer absorption lengths, these conditions will need to be confirmed as part of future detector validation.

4.5 Conclusion

In this work, the light coupling efficiency from an opaque liquid (dilutions of commercial cow milk) into a WLS fiber was quantified as a function of the optical parameters of the liquid and the distance from the origin of the light to the fiber. The Geant4 model was validated against experimental data, and an agreement between the Geant4 model and a simplified diffusion approximation to within 11% error was demonstrated. The validated model was used to show the efficiencies that may be possible in LiquidO-style detectors of optimal optical properties.

CHAPTER V

Design and Fabrication of an Opaque Scintillator Prototype Based on NoWASH-20

This chapter describes the design, fabrication, and preliminary characterization of a prototype opaque detector using a wax-based scintillation liquid. First, it discusses the design considerations including constraints and material factors. The design was intended to allow for compatibility with a variety of opaque scintillator liquids, rather than optimizing for a specific type or set of optical parameters. Following this, the chapter outlines the formulation of the scintillation liquid and the construction of the prototype. Lastly, it presents the detector's response to gamma rays of various energies and demonstrates coarse reconstruction of source direction using the average event topology resulting from light confinement.

5.1 Design considerations

5.1.1 Constraints

The main design constraint was a limitation in the number of channels that could be instrumented. A large quantity (500 m) of wavelength-shifting fiber was procured and the multi-anode photomultiplier tube (MAPMT) used had 64 pixels. However, only two identical digitizers (of 16 channels each) were available for use. Using several different types of digitizers could introduce additional uncertainty into the relative

responses of various channels, and was avoided. This limited the available number of readout channels to 32.

A different readout scheme that would not rely on digitized waveforms was examined. For instance, a PETSYS TOFPET2 ASIC connected to a 64-channel SIPM array was investigated for suitability. However, single-photoelectron signals were indistinguishable due to electronic noise. A commercial system for reading out a large number of SIPM channels was also considered. For example, the CAEN DT5202 readout system can connect to 64 individual SIPMs, which could each be coupled directly to fiber ends. However, this device is designed to count individual photons (with a long dead time following each count) or to combine the signal from multiple photons that arrive in a very short time. It is unable to integrate over the long time window in which photons are expected to arrive in an opaque scintillation system ($\sim$100 ns). After discussing with CAEN engineers, it was clear that the DT5202 or a similar system could not be used for this application, and traditional waveform digitization became the most attractive choice.

The goal of the design was to enable topological reconstruction in three dimensions. A hit on a fiber gives information in two axes, but not three. For example, if a fiber is aligned along the x-axis, a detected photon within it provides positional information about the origin of that photon in the y-direction and z-direction. Information about the depth (in this example, the x-direction) at which the photon originated within the fiber is lost because of the relatively long decay time of the WLS dye and because both ends of the fiber are connected to a single MAPMT pixel. Furthermore, due to the small size of the prototype detector (10 cm in width), the relative delay in arrival time for a photon on one side of the detector compared with the other would be less than 1 ns. Therefore, a further constraint was that

the fibers had to be aligned in at least two orthogonal directions, so as to provide three-dimensional position information.

5.1.2 Geometry

The 32-channel constraint, along with the need to have fibers running in two planes, naturally suggested a cubical design with 16 fibers per vertical plane. In this design, the fibers interspersed throughout the xz-plane (where z is the vertical direction) could be offset vertically by 1/2 the fiber pitch, such that they did not collide with the fibers in the yz-plane. The last remaining parameter to select was the fiber-pitch, which would determine the overall size of the detector body. A suitable fiber pitch was determined through the use of a Geant4 model, in which the parameters of NoWASH-20 were estimated from Ref. [27]. The optical parameters key to choosing the fiber pitch were the absorption and scattering length, which were taken as 1 m and 1 mm, respectively. The model indicated that a photon collection efficiency (fraction of photons delivered to the MAPMT) as high as 9.8%, was possible with a $10 \times 10 \times 10$ cm^3 cube size, corresponding to a total efficiency (in p.e./photon) of 1.2%.

A CAD rendering of the final cube prototype design is shown in Fig. 5.1. The fiber pitch is 2 cm, and the fibers are in the planes offset vertically from one another to avoid collisions.

5.1.3 Materials

5.1.3.1 Fiber

To maintain consistency with the previously validated model (see Ch. IV) the prototype was designed to use Kuraray Y-11(200) WLS fibers. Y-11 fiber is not unique in its applicability to opaque scintillators; there are many other sizes, types,

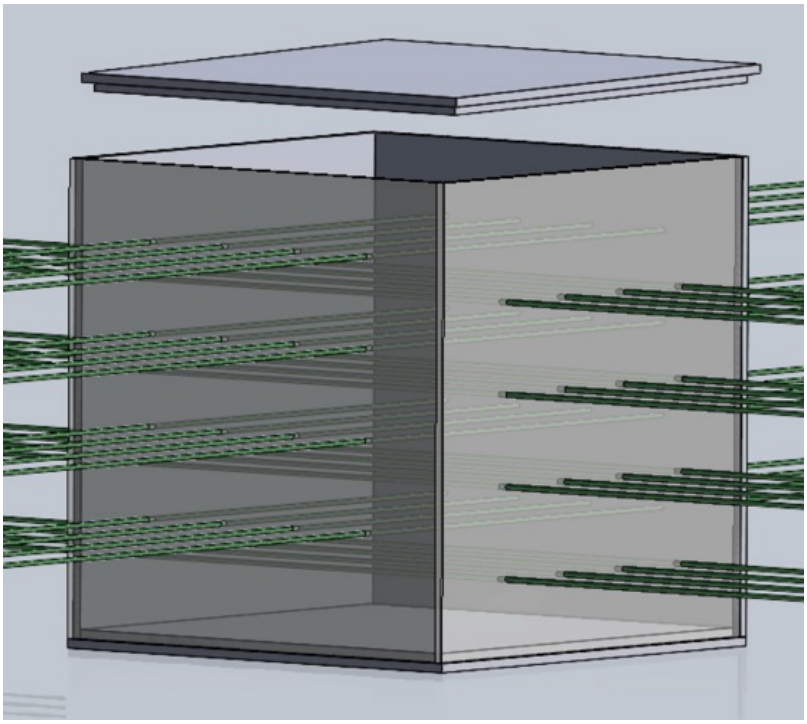

Figure 5.1: A CAD rendering of the final cube design. The capacity is 1 L, and the fiber pitch is 2 cm. The fibers are shown as green lines.

and manufacturers of WLS fibers. For example, the Kuraray B-3 fiber is a UV-to-blue shifter that has a longer attenuation length than the Y-11 [69], and the YS-2 has a similar attenuation length to Y-11 but has a decay time of around half the value of the Y-11 [85]. However, Y-11 fiber is commonly used in scintillation applications, represented by a wide body of literature, and its properties are well understood. This made it a good choice for the prototype presented here.

5.1.3.2 Body

The body of the detector volume is made from 1/4″ thick 6061 aluminum and was fabricated with 4043 welding rods by the University of Michigan Physics Instrumentation Shop. Aluminum was chosen for its relatively low atomic number (to minimize gamma ray shielding), ease of machining, and good compatibility with a variety of solvents. The holes for the fibers were drilled out with a 3/64″ bit. The

lid is made of the same material as the body.

An advantage of aluminum over a 3D printed material was that it allowed for the hot-pouring of wax-based opaque scintillators (described below). Many 3D printed materials have a very low melting point and are thus unsuitable for this application.

5.1.3.3 Glue

The glue chosen was a UV-cured epoxy called Bondic. This epoxy was recommended by Thiago Sogo Bezerra from the University of Sussex, who investigated compatible glues for the LiquidO collaboration. The epoxy was easy to apply as it was very viscous, and remained in place well until cured with UV light. In the first trial, several fiber holes leaked scintillation liquid during the cooling and solidification process. Upon inspection, it appeared that some of the Bondic did not adhere strongly to the aluminum body of the detector. Adherence may not be a problem with other detector body materials, but for aluminum-bodied detectors, other glues should be investigated.

An additional shortcoming of this glue was the need to be UV cured. Previous studies of scintillating fibers have shown that the attenuation length of the core can worsen by up to 50% with a long duration (multi-day) exposure to fluorescent lights [99]. While the effect of exposure to a short-duration, high-intensity UV light source on a WLS fiber is unknown, it is likely deleterious. For this reason, a non-UV cured epoxy was used for subsequent prototypes.

5.1.3.4 Scintillation liquids

There are two major types of opaque scintillation liquids currently under investigation by the LiqudO collaboration: wax-based and emulsion-based. NoWASH-20 (New opaque Wax Scintillator, Heidelberg) is an example of a wax-based liquid scin-

tillator, in that the opacity is a result of the addition of paraffin. Conversely, the opaque water-based liquid scintillator (oWbLS) accomplishes opacity via the stable emulsion of water into a base solvent. There are many other ideas to achieve opacity in scintillation compounds, but these two technologies are the most mature. Formulations of oWbLS and NoWASH-20 were simultaneously pursued to de-risk the design. In both cases, receiving the liquids took longer than originally anticipated, so the optical parameters of the scintillators were unknown when designing the detector prototype. However, the NoWASH-20 parameters could be estimated from the groundbreaking work done by Buck *et al.* [27].

The remainder of this chapter will focus on NoWASH-20, with the characterization of an oWbLS-based design discussed in the following chapter.

NoWASH-20 was prepared according to the steps outlined in Ref. [27]. NoWASH is comprised of a minimum of three component chemicals. The first is linear alkylbenzene (CAS 67774-74-7), known as LAB, sourced from BOC Chemicals. The second is 2,5-diphenyloxazole (CAS 92-71-7), known as PPO and sourced from Sigma Aldrich. The third is paraffin wax (CAS 8002-74-2) obtained from Sigma Aldrich. The wax has a nominal melting point of $53-58^{\circ}$ C, which is associated with the ASTM D 87 standard. The scintillation light from LAB peaks around $330-350$ nm [63], which is well below the absorption spectrum for the Kuraray Y-11 fibers. The PPO works as a primary fluor, the addition of which increases the light yield of the base LAB. One study identified that increasing the concentration of PPO in LAB from 1 to 4 g/L corresponded with a 30% rise in light yield [100]. PPO also serves as a wavelength shifter, peaking in emission at around $350-380$ nm [101], although this range is not optimal for Y-11 fibers, which have maximum absorption around 420 nm. The initial goal was to replicate the original NoWASH formulation as described in

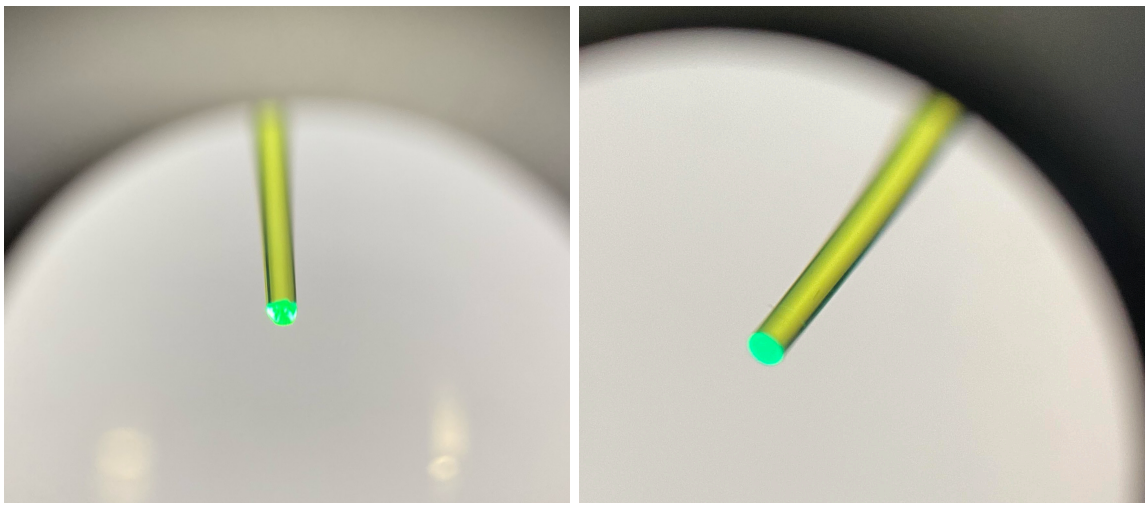

Figure 5.2: An image taken through a jeweler's glass of the end of a WLS fiber before (left) and after (right) polishing with a series of fine grit sandpaper. All fibers were similarly prepared and inspected before loading into the prototype detector body.

Ref. [27]. However, the absorption spectrum of the fibers indicated the potential need for a secondary wavelength shifter, such as 1,4-bis(5-phenyloxazol-2-yl)benzene (POPOP).

5.2 Assembly

5.2.1 Detector body and fibers

The holes in the detector body needed to be hand-filed before they could receive the fibers without scratching the cladding. The file used was a 1.0 mm diamond round jeweler's file. Fibers were cut to a length of 1 m, and polished using the same procedure described in Ch. IV.

As described in Ch. IV, the fibers were cut with a fiber cleaver and polished with fine-grit sandpaper. Fig. 5.2 shows a magnified image of a fiber end before and after polishing. The fibers were connected to the MAPMT via a 3D-printed interface. The holes in the interface are 3 mm in diameter, allowing for silicon o-rings to fit inside the holes to hold the fibers in place by friction. An image of the interface

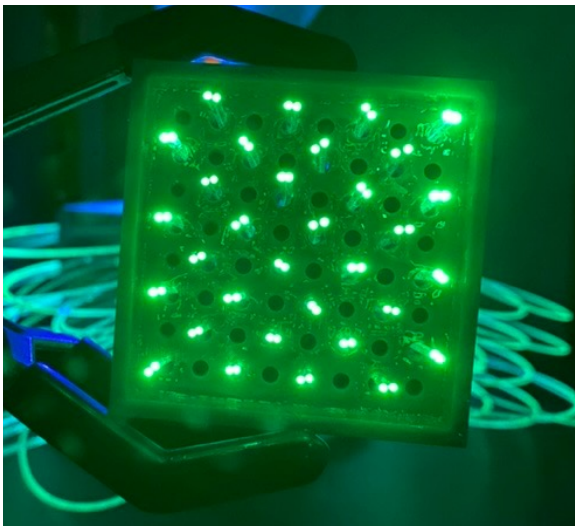

Figure 5.3: An image of the fiber-MAPMT interface. The fibers are held in place within the interface with silicon o-rings and are coupled to the face of the MAPMT with optical grease. Both ends of each fiber are routed to the same MAPMT pixel.

with polished fibers loaded and ready for mounting to the MAPMT is shown in Fig. 5.3. Differently from the arrangement described in Ch. IV, both ends of each fiber were routed to a single MAPMT pixel to maximize the light collection in each channel. The fibers were installed and aligned in the holes such that the bending radius for each was minimized when coupled to the MAPMT interface. The dark box, MAPMT, and interface were the same as described in Ch. IV. The installation process is shown in Fig. 5.4. A schematic of the assembled apparatus is shown in Fig. 5.5.

5.2.2 NoWASH-20

The most opaque NoWASH formulation discussed in the cited reference is known as NoWASH-20 for its 20% (by weight) wax inclusion. The cocktail includes a 0.3% weight fraction of PPO, with the balance consisting of LAB. The wax was added to the LAB as a room-temperature solid and then heated to 60° C on a hotplate until the wax fully melted. Temperature measurements were taken with a Fluke 61

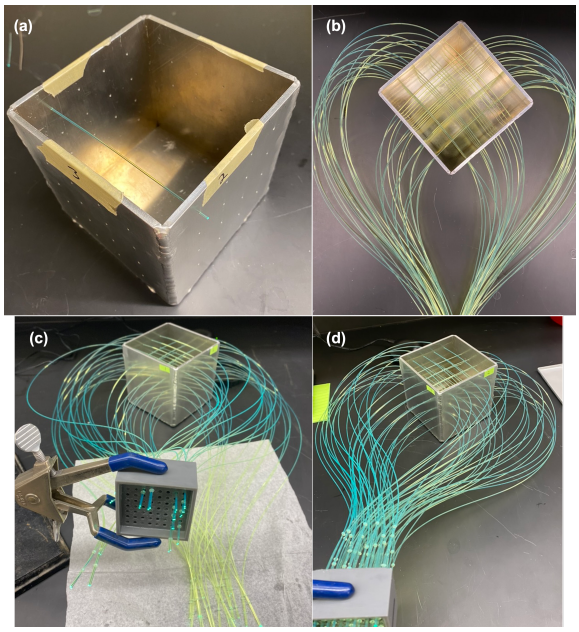

Figure 5.4: The detector body prototype (a) and installation of fibers (b-d). The fibers were 1 m long and arranged such that the bending radius was minimized when coupled to the MAPMT interface (d).

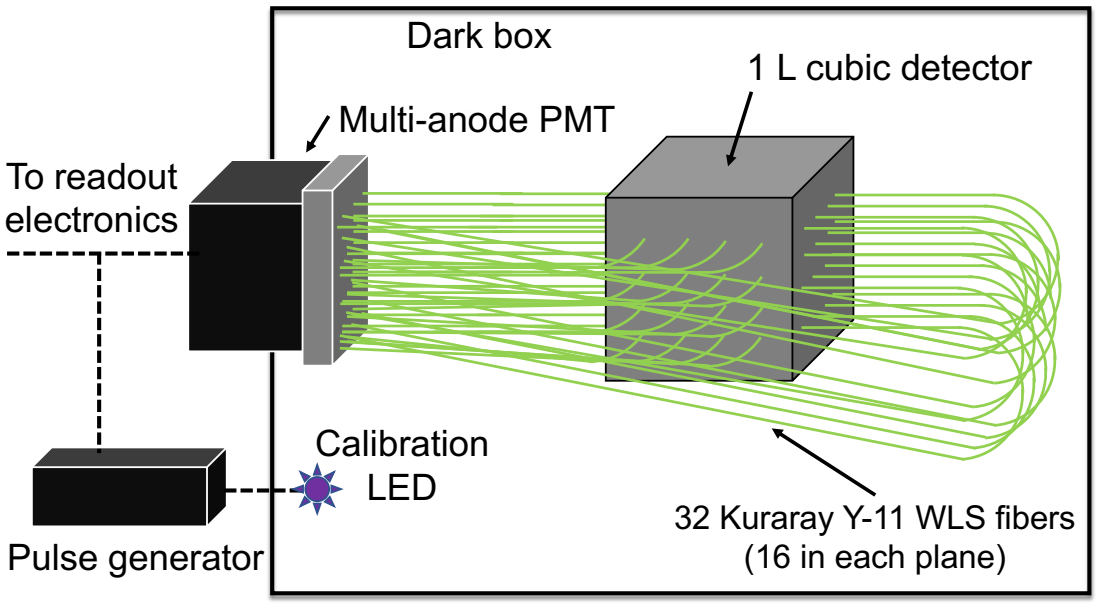

Figure 5.5: A schematic of the experimental apparatus, including the 1 L aluminum cube prototype. The dark box, calibration LED, MAPMT, and readout electronics are the same as were described in Ch. IV.

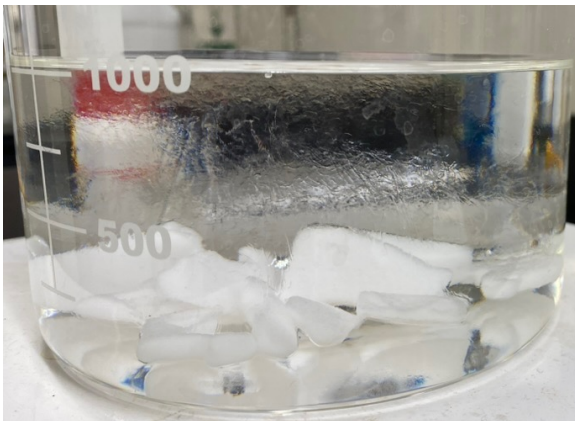

Figure 5.6: An image of the NoWASH-20 melting process. A 20% weight fraction of paraffin wax was added to a mixture of LAB and 3 g/L PPO, then slowly heated to 60° C on a hotplate. The melting process took about 15 minutes, after which the liquid appeared completely clear.

infrared thermometer, which is rated to an accuracy of ±3° C. Heating and melting took about 15 minutes, and is shown in Fig. 5.6. Once the wax was completely dissolved, the PPO was added and stirred for 1 minute. The PPO dissolved in a matter of seconds, and the resulting liquid appeared completely transparent. The cocktail was poured while still warm into the detector body and allowed to cool. The liquid continued to appear clear until it cooled to about 34° C, after which crystallization became apparent as a skein on the top. As the liquid continued to cool, the opacity increased rapidly. By about 30° C, the immersed sections of fibers could no longer be seen. See Fig. 5.7 for a visualization of the cooling process.

5.2.3 Volume collapse

The density of paraffin can increase by up to 19% when cooled from 70° C to 25° C [102]. An analysis of a mixture of linear-alkylbenzene compounds meant to be used as a lubricant showed a lesser, but still appreciable increase in density of about 3% from 68.6° C to 23.4° C [103]. Taken together, a density increase of about 5% is expected when NoWASH-20 cools from 60° C to 20° C. The prototype detector is not equipped with active cooling but cools from the outside-in from exposure to

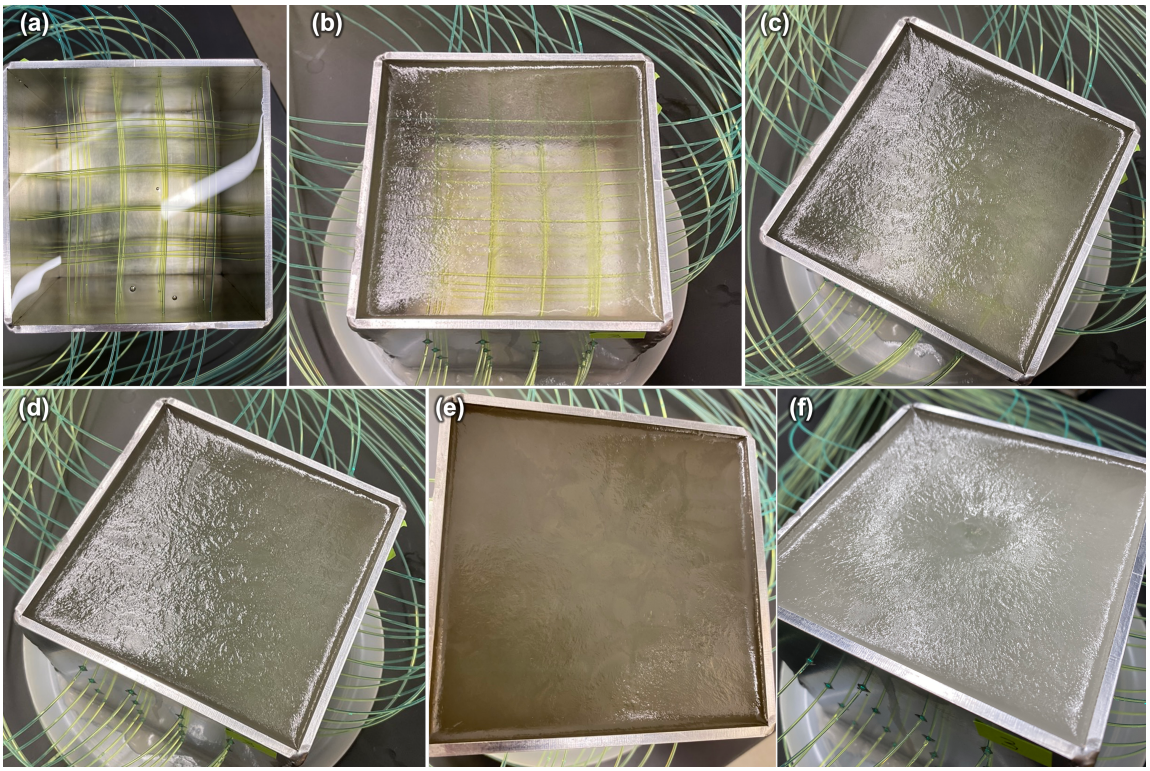

Figure 5.7: The change in appearance of the NoWASH-20 scintillating liquid as it cools. The temperatures were (a) 49° C, (b) 34° C, (c) 32° C, (d) 31° C, (e) 30° C, and (f) 19° C, after cooling to room temperature overnight. As can be seen in panel (f), the reduction in density as the liquid-cooled resulted in a small depression in the center of the surface.

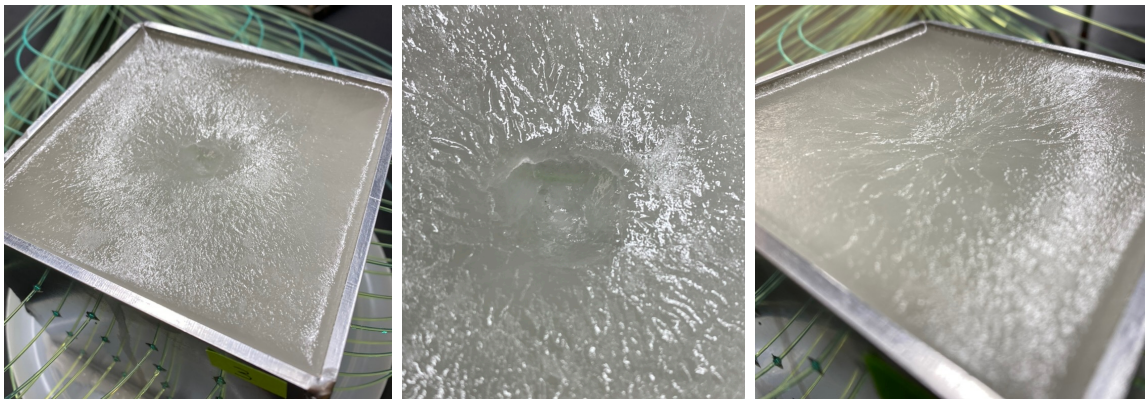

Figure 5.8: An image of the volume collapse on top of the detector. The left panel shows the volume collapse of the first iteration of the prototype, in which the liquid was poured at approximately 60° C. The center panel shows a close-up of the volume collapse in this iteration. The top layer of fibers can be seen, indicating that the light collection efficiency of these fibers is impacted by the depression. The right panel shows the reduced volume collapse from allowing the liquid to cool to approximately 41° C before pouring.

its environment. This means that the outside, and especially the top of the liquid, cools and solidifies first. Then when the inside cools and subsequently decreases in volume, the result can be volume collapse. An illustration of volume collapse is shown in Fig. 5.8. As a result of the depression, the top layer of fibers is partially exposed, which may impact the light collection efficiency in this part of the detector. Due to the opacity of the material, it is difficult to assess whether voids are present in the interior of the detector. However, due to the relatively low viscosity of the cooled liquid (it is more gel-like than wax-like), such structures are improbable. In later iterations, the liquid was allowed to cool to 41° C before pouring into the cube, which mitigated the severity of the volume collapse phenomenon considerably, as can be seen in the right panel of Fig. 5.8.

5.3 Gamma-ray response

5.3.1 Event building

Pulses were calibrated from ADC channels to units of photoelectrons (p.e.) using the method described in Ch. IV. Pulses were required to have an integral value of 0.5 p.e. to be included in the datasets.

In order to correlate pulses into events both CAEN V1730 digitizers were synchronized to share a clock. Each channel was allowed to trigger independently, and the timestamps from individual pulses were used to bundle pulses into events. To reduce the effect of stray room light, a minimum of three channels were required to trigger within a coincidence window of 100 ns to qualify as an event.

Further discussion of event building is included in Ch. VI.

5.3.2 Response with PPO as the sole wavelength-shifter

After cooling overnight, the detector was exposed to gamma-ray radiation from ^{137}Cs and ^{60}Co. Gamma rays from ^{137}Cs beta-decay have an energy of 661.7 keV, whereas ^{60}Co beta-decay produces gamma rays of 1173.2 keV and 1332.5 keV. For gamma rays in this energy range, the dominant interaction with low effective atomic number material like NoWASH-20 is Compton scattering. There was a visible difference in the spectra from each radioisotope, with the gamma rays from ^{60}Co creating more light, as expected. However, neither the Compton continuum nor Compton edge was visible in either spectrum (see Fig. 5.9), and overall the collected signal was lower than expected from the simulation. The high opacity of the liquid is expected to smear Compton features, because the collected signal depends not only on the amount of light created in the volume, but also on the position of interaction in relation to the fibers.

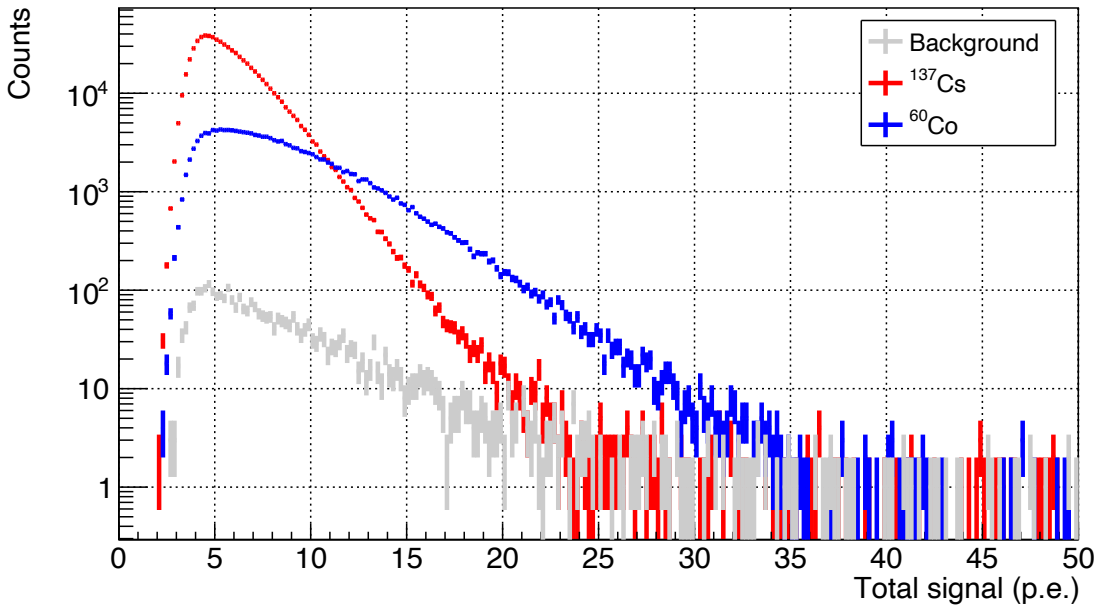

Figure 5.9: The measured integral gamma-ray spectra from the decays of ^{137}Cs and ^{60}Co. As expected, the higher energy gamma rays from ^{60}Co have a higher spectral endpoint, indicating that they created more light in the volume. However, no Compton features are readily identifiable.

There were two possible explanations for the low light level. The first is that the scattering length of the liquid was too short to be well-matched to the selected fiber pitch. This would manifest as isolated, very bright events for gamma rays that deposited energy in the immediate vicinity of a fiber, and the signal from most events would be isolated to a single fiber. This was not the case, so an extremely low scattering length was dismissed as the possible cause of the low light collection. The second possible explanation was that the emission spectrum of the PPO and the absorption spectrum of the WLS fibers were poorly matched. This was anticipated from the published values for each, which are shown in Fig. 5.10. Buck *et al.* directly measured the emission spectrum of NoWASH-20 with PPO loading and found a similar spectrum to the PPO emission spectrum shown in Fig. 5.10, except for slight red-shifting which caused the peak around 335 nm to be absent [27]. They expect

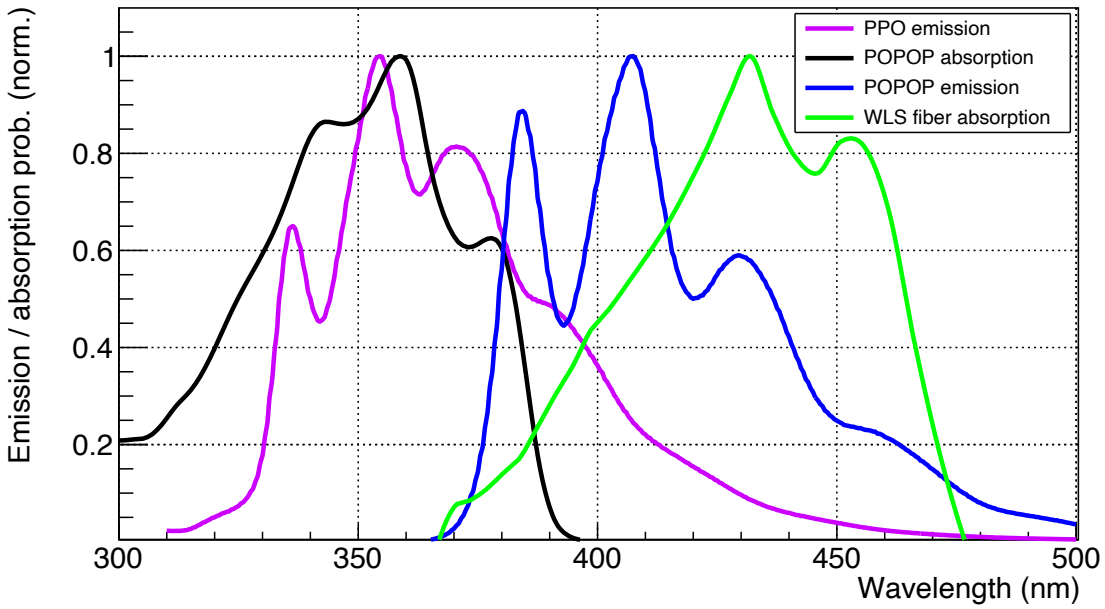

Figure 5.10: The emission and absorption spectrum for several components in the NoWASH-20 blend. The PPO and POPOP emission and absorption spectra are taken from Ref [101], and the WLS absorption spectrum is for Kuraray Y-11(200) fiber and is taken from Ref. [69].

that "the light below 400 nm is mainly absorbed by the fluorescent PPO or LAB and re-emitted with high probability", but our measurement suggests that UV light may not be repeatedly shifted until it is sufficiently well matched to the Y-11(200) WLS fibers.

5.3.3 Addition of POPOP

Following the experiment detailed above, the detector body was warmed directly on the hotplate, which allowed the re-liquefied contents to be emptied into a beaker. 10 mg of POPOP was then added. This concentration is typical for similar scintillators based on LAB/PPO mixtures [104].

The POPOP was, unlike the PPO, very difficult to dissolve into the NoWASH-20, requiring about 90 minutes of vigorous stirring at 60° C Similar issues with POPOP solubility were previously reported in Ref. [105]. The process of the addition is

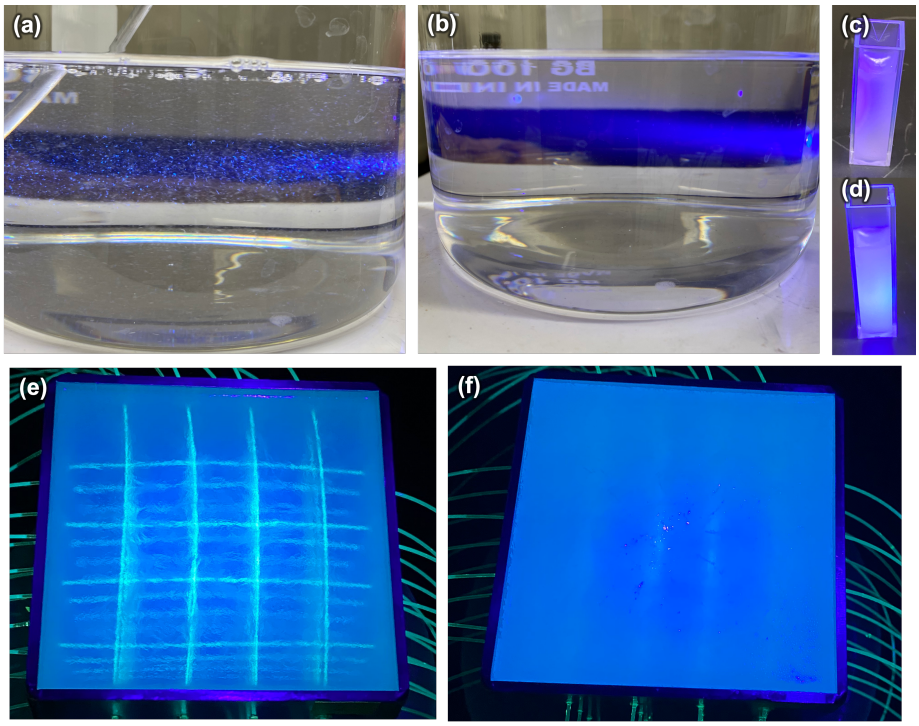

Figure 5.11: The process of adding POPOP to NoWASH-20. (a) The POPOP can be seen as undissolved flakes in the heated (60° C) NoWASH-20. (b) After 90 minutes of vigorous stirring, the POPOP was fully dissolved. (c) The appearance of the NoWASH-20 under UV illumination before and (d) after the addition of POPOP. The color has changed from violet to blue. (e) The NoWASH-20 with POPOP under UV illumination after being cooling in the cube to 33° C and (f) 18° C. The change in opacity is apparent.

shown in Fig. 5.11. Another candidate for use as a secondary wavelength shifter is 1,4-Bis(2-methylstyryl)benzene (bis-MSB), which has similar properties but may be more readily dissolved.

5.3.4 Response with PPO and POPOP

The emission spectrum of NoWASH-20 after the addition of POPOP was directly measured with a PTI Quanta Master Fluorimeter, using an excitation wavelength of 350 nm. The excitation wavelength was chosen to be close to the peak emission of PPO. The measured emission spectrum is shown in Fig. 5.12 and closely matches the literature values of the emission spectrum of POPOP (shown in Fig. 5.10), except that the shortest-wavelength peak (around 390 nm) is suppressed, probably due to

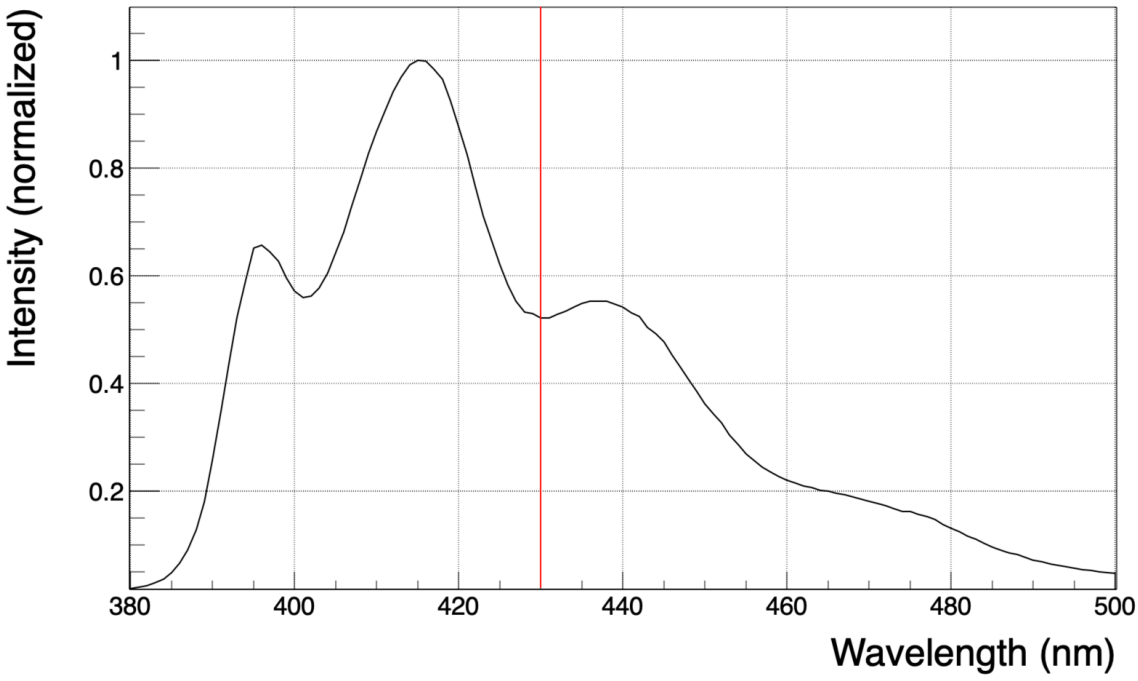

Figure 5.12: The measured emission spectrum of NoWASH-20 after the addition of 10 mg/L of the wavelength shifter POPOP. The peak absorption wavelength of the Y-11 fibers is shown as a vertical red line.

repeated wavelength-shifting. Following the addition of POPOP, the NoWASH-20 was reloaded into the aluminum cube and again cooled, as shown in Fig. 5.11. The changes in opacity were qualitatively the same as before the addition of POPOP. During this iteration, the liquid was allowed to cool in the beaker to 41° C prior to pouring, which seemed to mitigate the volume collapse and resulting dimpling of the surface as discussed and shown in Fig. 5.8.

A comparison of the NoWASH-20 response to gamma rays from two radioisotopes before and after the addition of POPOP is shown in Fig. 5.13.

5.3.4.1 Source localization via event topology

To demonstrate source localization using event topology from light confinement, a 1 µCi ^{60}Co gamma-ray source was placed on the top of the cube in two positions. The first position was approximately $(-45, 45, 55)$ mm, and the second position

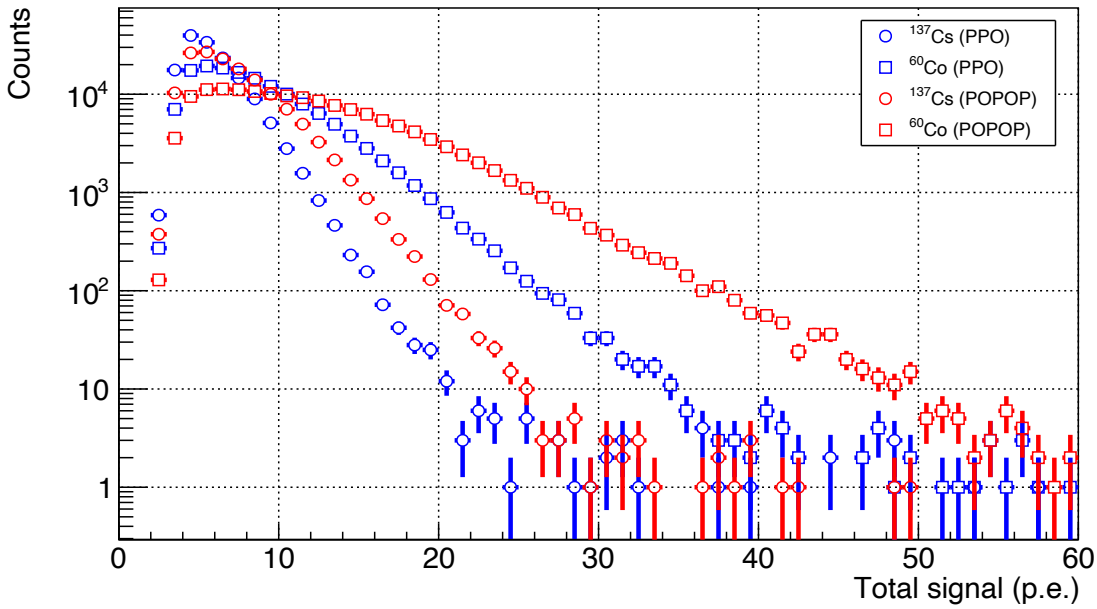

Figure 5.13: The measured integral gamma-ray spectra from the decays of ^{137}Cs and ^{60}Co before and after the addition of POPOP to the NoWASH-20. The first 1.5×10^5 events are shown for each dataset. As expected, the addition of POPOP resulted in a larger integral signal for both radioisotopes. However, Compton features are still difficult to discern, probably due to the high opacity of the NoWASH-20.

was approximately $(45, -45, 55)$ mm, where (0,0,0) is the center of the detector volume. 100 seconds of data was taken in each position, and events were built as described above. A 2D histogram was then created, in which bins corresponded to the normalized number of photoelectrons detected in each fiber. The results, along with 2D Gaussian fits to guide the eye, are shown in Fig. 5.14.

While not meant to be quantitative, the plots clearly show a difference in response that corresponds to the source location. This effect is primarily due to the $1/r^2$ dependence of intensity from an isotropic source. This means that more events occur near the source, and because the resulting scintillation photons are stochastically confined, the channels corresponding to fibers near the source receive more signal. In principle, by comparing the relative signal across all channels, this detector should be able to reconstruct the direction of a source even if the source is far away. The

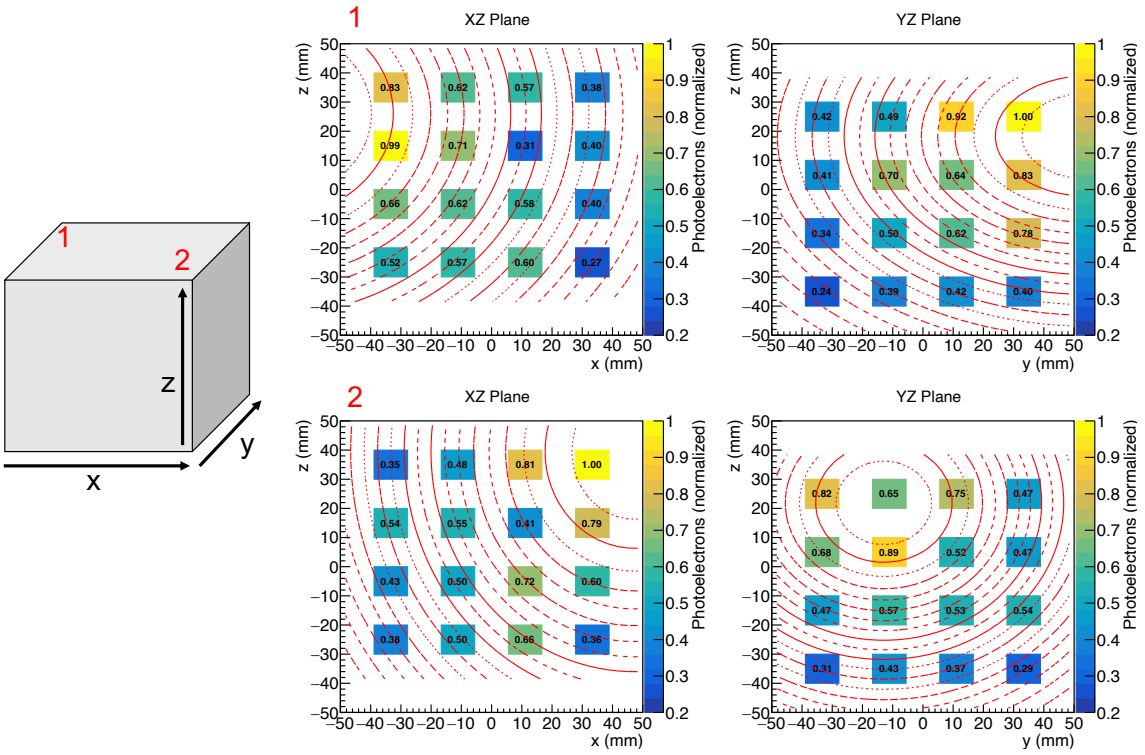

Figure 5.14: A demonstration of source localization from average event topology. The top row of histograms corresponds to a 100 sec. measurement of a 1 µCi ^{60}Co gamma-ray position 1 (as annotated on the sketch to the right), and the bottom row of histograms corresponds to the measurement with the source at position 2. The cells indicate the normalized number of photoelectrons generated in that channel, and 2D Gaussian fits are included as eye guides. The approximate location of the source in the xy plane is readily discernible in each case.

dominant cause of the relative difference in signal across different channels in this case would not be a $1/r^2$ intensity mapping, but rather a result of self-shielding. This effect would be clearest for incident radiation with a mean free path of less than the dimensions of the cube.

This measurement gave confidence that the prototype achieved light confinement and reasonable light collection, and was capable of leveraging the resulting event topology to address source localization, a real-world problem in radiation detection.

5.4 Conclusion

This chapter described the design, construction, and initial characterization of the first prototype gamma-ray detector based on opaque scintillation. The following chapter will provide a more quantitative characterization of the second iteration of the prototype, using an acrylic cube and several different formulations of oWbLS.

CHAPTER VI

Characterization of an Opaque Scintillator Prototype Detector Based on oWbLS

6.1 Introduction

Most scintillation-based radiation detectors collect the light generated by an interacting particle at the scintillator boundary and direct it to a photosensor such as a photomultiplier tube (PMT) or a silicon photomultiplier (SIPM). To maximize the light collection, scintillation materials are chosen to be as transparent as possible to their fluorescence. Scintillation light is emitted isotropically, so much of the light collected at the photosensor may arrive after reflection or scatter at non-sensing boundaries, such as detector walls. The photosensors used are generally not position-sensitive, and even for position-sensitive photosensors, the distribution of detected light has only limited correlation to the location of its emission. For these reasons, detectors of this type generally do not provide high-fidelity information on where in the detector volume an event occurred.

The two main categories of methods for obtaining event topological information in a traditional scintillation detector are imaging the interior of the detector, usually by using multiple photosensors distributed along the detector surface [106, 107, 108, 109, 110, 111], and physically segmenting the detector into voxels [19, 20, 77, 111].

By contrast, opaque scintillators, which are designed to have a short scattering

length, seek to constrain the scintillation photons by repeated scattering. The light produced by an event is *stochastically confined* about its origin, and information about the event topology is thus retained [24, 112]. The scintillation photons are collected via a lattice of wavelength-shifting (WLS) fibers and read out by channel, such that the signal amplitude in multiple fibers provides information about where in the volume the light was collected. This information can then be used to reconstruct the event topology.

This pioneering technology, known as LiquidO, is currently being developed by the international LiquidO Consortium [25]. The LiquidO concept was originally conceived to enhance particle-type identification and increase the signal-to-noise ratio in large antineutrino detectors through analysis of event topology. LiquidO is also being considered for positron emission tomography (PET) [113], improving energy resolution for photons in calorimeters for use with high-energy e^+e^- colliders [114], and the detection of geoneutrinos [115].

This chapter describes the characterization of a prototype radiation detector capable of providing spectroscopic and event topological information. Such a detector could potentially be used for certain applications currently served by traditional optically segmented detectors, such as gamma-ray and neutron-scatter cameras, or for muon scatter tomography. Specifically, the detector gamma-ray response is shown, and the reconstruction quality for point-like events is quantified.

6.2 Apparatus and material

The efficiency of light collection, transport, and conversion to signal for the experimental apparatus that shares most components with the one in this work was characterized in Ref. [74]. The type of fiber, multianode photomultiplier tube (MAPMT),

and digitizers were the same for this experiment as in that previous work. An opaque formulation of water-based liquid scintillator (discussed in Sec. 6.2.3) was chosen due to its promising optical characteristics and material compatibility and is referred to as opaque Water-based Liquid Scintillator (oWbLS).

6.2.1 Detector design and construction

Figure 6.1 shows the experimental apparatus. The body of the detector was made from an additively manufactured material (VeroWhite), which is similar to acrylic. The detector volume was a 1 L cube, 10 cm on a side. There were 16 WLS fibers arranged in a grid in each vertical plane. The fibers in the xz plane were offset 1 cm higher than the yz plane to avoid collision and provide additional information for the z direction. The fibers were glued in place with a fast-curing epoxy (5-minute Z-POXY), which was found to be compatible with WLS fibers and to cause less light loss than other glues tested [116].

The fiber pitch in the x- and y-directions was 2 cm, and 1 cm in the z-direction. Each fiber was approximately 1 m long. The detector was designed and constructed before receiving any oWbLS samples, so the fiber pitch was not optimized for the optical properties of a particular formulation of oWbLS. The length of the fibers was chosen to ensure that the minimum bending radius met the manufacturer's recommendations for minimizing light loss. The detector, fibers, and MAPMT were housed in a dark box to minimize background light during experiments and to protect light-sensitive components.

6.2.2 WLS fibers and MAPMT

The WLS fibers were Kuraray Y-11(200) (non S-type) blue-to-green shifters, 1 mm in diameter [69]. The fibers were cut with a precision cleaver and then polished with

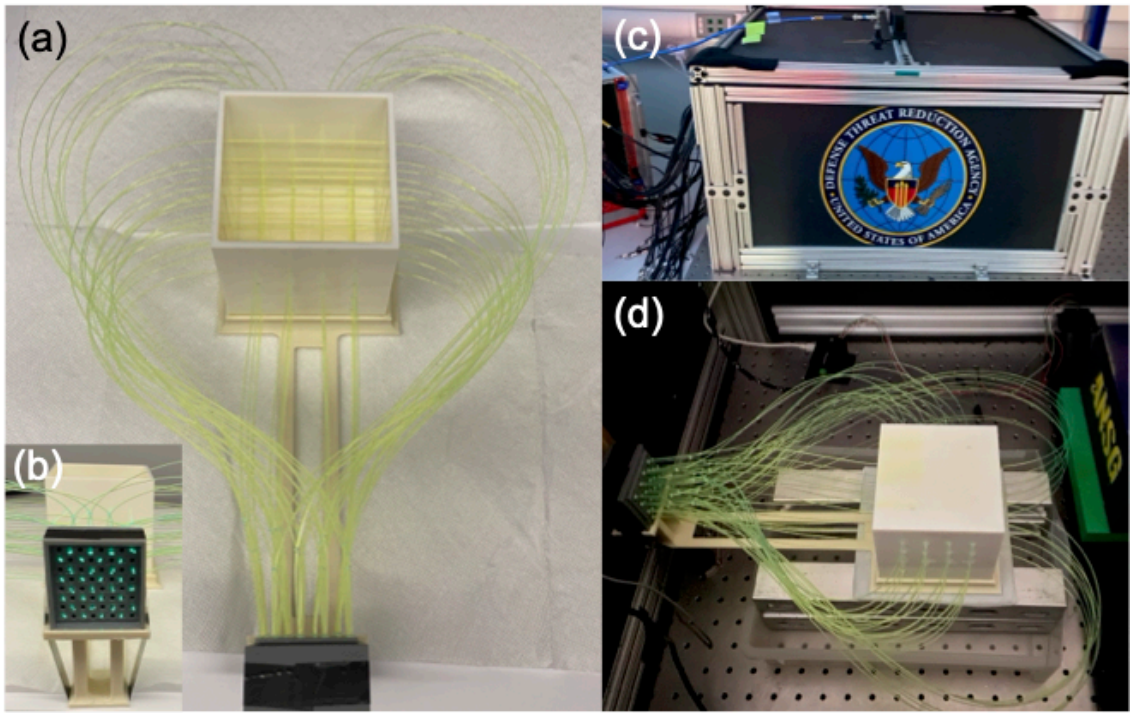

Figure 6.1: (a) Detector body made of VeroWhite with 32 WLS fibers glued in place. The fibers terminate at the MAPMT interface, shown from the front in (b). (c) Exterior of the dark box, with a pulsed LED mounted on top for calibration. The readout electronics are on the left. (d) Interior of the dark box with the detector mounted to the MAPMT. The top of the detector body is closed with a lid, also made of VeroWhite.

fine-grit sandpaper. Both ends of each fiber terminated at a single pixel of the Hamamatsu H12700A MAPMT and were held in place by a printed interface and silicone optical grease. The pixel size of the MAPMT is 36 mm^2, so the two fiber ends fit comfortably in the center of the pixel. The channels were chosen in a checkerboard pattern on the MAPMT to minimize crosstalk, as shown in Fig. 6.1(b).

6.2.3 Opaque water-based liquid scintillator

Water-based liquid scintillators have been under development at Brookhaven National Laboratory since 2011 [80]. They were originally conceived as a method to tune the relative levels of scintillation and Cherenkov light so that both could be readily detected in large antineutrino detectors. A stable emulsion is produced by the introduction of a surfactant that encapsulates the water into micelles. Transparent WbLS is manufactured in such a way as to minimize scattering. For this application, in which measuring the directional Cherenkov light separately from scintillation light is not an immediate objective, the loading of water was minimized to maximize total light yield.

In traditional WbLS, the function of water is to reduce the light yield, whereas in oWbLS the water introduces opacity. The micelles constitute scattering centers, and the appearance of the liquid becomes like soapy water. The base solvent was di-isopropylnaphthalene (DIN), chosen for its high light yield. To further maximize light yield, 2,5-diphenyloxazole (PPO) was added. Lastly, the wavelength shifter 1,4-Bis(2-methylstyryl)benzene (bis-MSB) was included to match the emission spectrum with the absorption spectrum of the WLS fibers.

As a basis for comparison, a batch of NoWASH-20 was also prepared [27]. NoWASH-20 is comprised of 80% linear alkylbenzene (LAB), 20% paraffin wax, and 3 g/L PPO. The wax is melted into the LAB such that when the mixture cools it becomes

Figure 6.2: From left to right: oWbLS1, oWbLS2, oWbLS3, and NoWASH-20. oWbLS1 has the longest scattering length of the three oWbLS samples and appears relatively transparent, and oWbLS2 has the shortest scattering length. The waxy consistency of NoWASH-20 at room temperature (∼18° C) can be observed.

highly scattering for the scintillation light. In this formulation, a 0.0025% weight fraction of the wavelength shifter 1,4-bis(5-phenyloxazol-2-yl)benzene (POPOP) was also added so that the emission spectrum better matched the absorption spectrum of the WLS fibers. NoWASH-20 can be poured while still warm but becomes viscous when at room temperature. Images of three formulations of oWbLS (oWbLS 1–3) and NoWASH-20 are shown in Fig. 6.2.

The initial batch of oWbLS2 showed some separation after shipment but was re-stabilized by bubbling nitrogen through the sample for 1 hour. This separation may have been caused by exposure to heat during transport. A lab-retained sample of the same batch did not show separation. The sample of oWbLS3 became gradually less opaque over a period of a month, potentially due to the agglomeration of micelles. A second batch of oWbLS2, used for the event reconstruction portion of this work, has shown good stability over approximately two months of data taking.

6.2.4 Data acquisition and analysis

Each channel of the MAPMT was read out into a channel of one of two CAEN V1730 digitizers. Before an experimental run, the response of each channel of the MAPMT was calibrated using a pulsed light-emitting diode (LED) mounted on the top of the dark box. The single photoelectron (s.p.e) response of each channel was found using the procedure outlined in Ref. [74]. During an experimental run, the clocks of the two digitizers were synchronized to facilitate the compilation of events using event timestamps. A voltage pulse that met the trigger threshold in a single channel was propagated to all channels on that board, but only pulses that met a pulse-integral threshold of approximately 0.5 photoelectrons were kept. The pulse-integral window was 100 ns, and integration was carried out onboard by the CAEN DPP-PSD firmware. In post-processing, events were constructed by identifying pulses that fell within a 100 ns coincidence window. This was necessary to correlate events between boards. The output of the data analysis pipeline was a list of events, for which the number of photoelectrons generated in each channel per event was known. This method of triggering and filtering was likely superfluous for this detector system because the background rate was very low. However, in future detector designs that use silicon photomultipliers, this style of event selection will be required to reduce the dark count rate, so it was implemented here. Figure 6.3 shows the data acquisition and event-building process as a flowchart.

6.3 Results

6.3.1 oWbLS light yield

The light yield of oWbLS was measured using the method described in Ref. [117], in which a large photomultiplier tube views a cuvette of liquid scintillator exposed

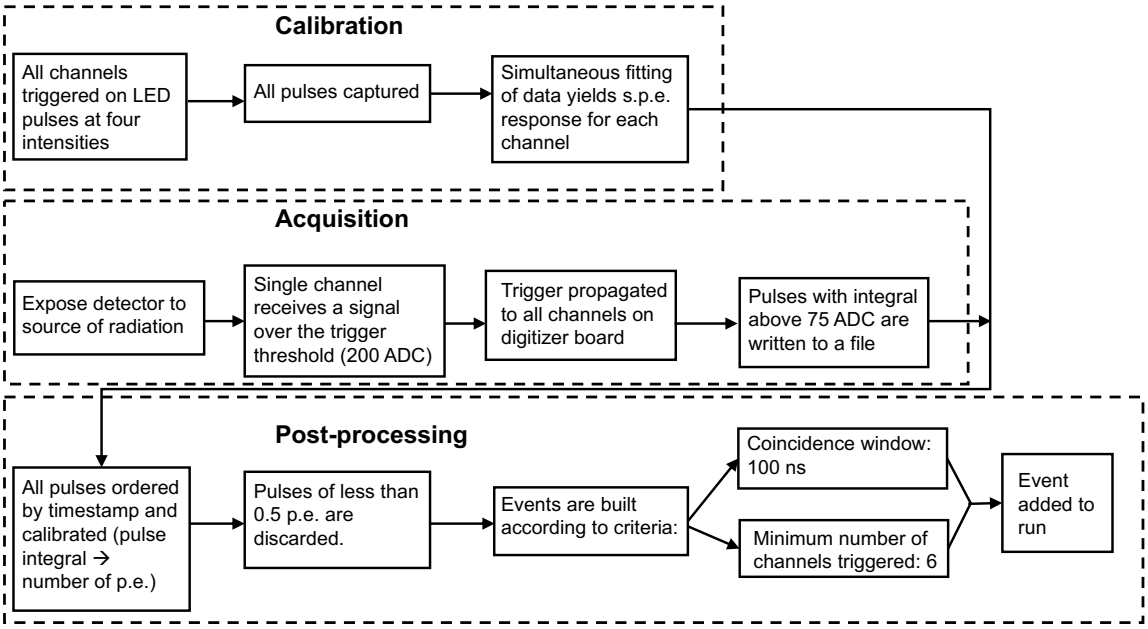

Figure 6.3: A flowchart of the data acquisition and analysis process. The primary input for a data run is the s.p.e response for each channel, and the output is a list of events, each of which contains pulses from multiple channels that have been correlated by their timestamps and calibrated to be in units of p.e.

to gamma rays from ^{137}Cs. The light yield of an unknown scintillator is determined by comparison to a characterized reference. The reference scintillator was linear alkylbenzene (LAB) with 3 g/L of PPO, which has a light yield between 8700 [118] and 11100 [81] photons/MeV. The NoWASH-20 sample was found to have a light yield of $\sim$ 90% of LAB+PPO, which is consistent with prior findings in a different experimental setup [27, 119]. Using the average of the two LAB+PPO light yields above as a reference, the light yield of oWbLS was determined to be 12150$\pm$1470 photons/MeV. This value is consistent with other scintillators based on DIN, such as EJ-309, which has a light yield of 12300 photons/MeV [120]. The uncertainty is dominated by the range of light yields reported in the literature for the reference scintillator. These results are summarized in Table 6.1.

Material	Measured light yield	% LAB+PPO
LAB+PPO	9890±1200	100
NoWASH-20	8850±1070	89
oWbLS1	10900±1320	110
oWbLS2	12150±1470	123
oWbLS3	12150±1470	123

Table 6.1: Measured light yields of opaque scintillation liquids used in experiments

6.3.2 oWbLS absorption and scattering length

The degree of light confinement in an opaque scintillator depends on its scattering and absorption lengths. An increase in either the scattering or absorption length increases the mean distance a photon travels from its origin before being absorbed, and thus increases the size of the *light ball* [24]. One way to compare the relative size of the light ball among different oWbLS formulations is to observe the number of channels triggered as a function of the total signal collected in an event. For a highly confining formulation, the number of channels increases slowly as the total signal increases, whereas, for a transparent scintillator, the number of channels triggered increases more quickly. This relationship is apparent in Fig. 6.4. To determine the absorption and scattering length of oWbLS3, a pulsed fiber-coupled laser was used to inject a known number of photons into the detector volume, as shown in Fig. 6.5. The measured distribution of signal over WLS fiber channels was compared to a Geant4 simulation in which six parameters were allowed to vary: the x, y, and z position of the fiber tip, the absorption and scattering length of the oWbLS, and the reflectivity of the detector walls. The estimated position of the fiber tip before fitting the data was $(0 \pm 5, 0 \pm 5, 0 \pm 5)$ mm.

The reflectivity of the walls was estimated from Ref. [121], which quantified the optical parameters of several colors of printed plastics. The wavelength of the laser (407 nm) lies in the transition region for the spectral reflectance of VeroWhite plas-

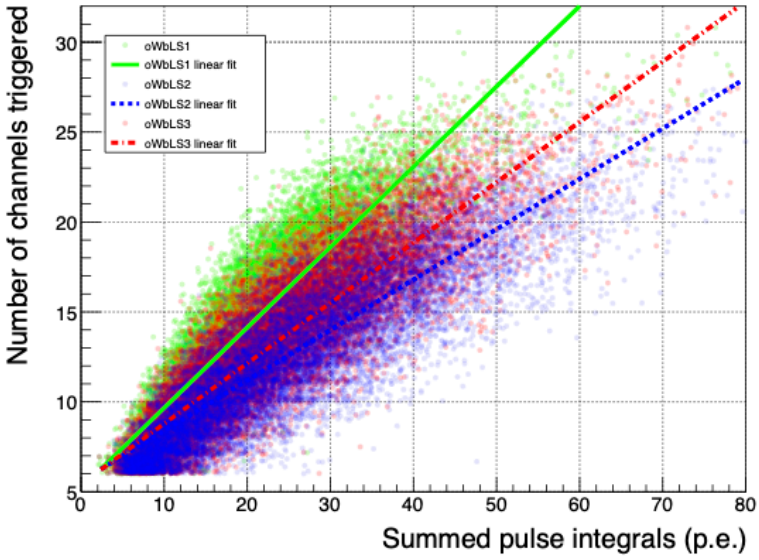

Figure 6.4: Relationship between the number of triggered channels and total event signal for the three formulations of oWbLS. The data shown is from the ^{60}Co datasets. Linear fits are shown to guide the eye and highlight the difference in confinement for scintillation photons in each liquid.

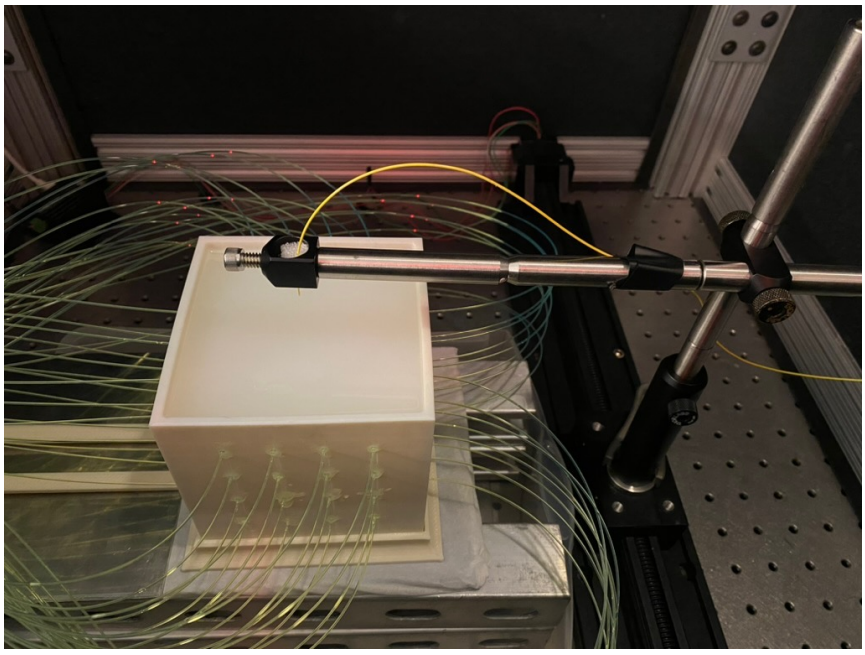

Figure 6.5: An image of the measurement described in Sec. 6.3.2. A fiber-coupled laser is used to inject photons into the center of the detector, and the response for each channel is measured. The laser fiber is held by an apparatus mounted on a linear translation stage so that the measurement can be repeated at various distances from the center of the detector.

tics. The indices of refraction of liquid scintillation cocktails based on DIN were found to be between 1.55 and 1.6 at 404.7 nm, with most around 1.56 [122]. The index of refraction of oWbLS is likely to be slightly smaller as a result of the addition of water. The index of refraction of VeroClear, a transparent but similar material to VeroWhite, was reported to be about 1.48 at 400 nm [123], so the specular reflection at the oWbLS-VeroWhite boundary is expected to be less than in the measurement of Ref. [121], which was done in air.

The optimal parameter combination was found with a genetic algorithm [124]. For each individual in a generation, a Geant4 simulation was run with the corresponding parameter values. The fitness of an individual was calculated as the value of χ^2 between the simulated and experimental data. A comparison of the experimental and simulated signal distributions is shown in Fig. 6.6. To investigate the compatibility of the experimental and simulated distributions with the optimized parameters, a χ^2 test was applied to each laser pulse measurement, with the simulated distribution as a reference. The mean χ^2/NDF value was 0.6 ± 0.2, where uncertainty is the standard deviation of the distribution. The absorption length of DIN is known to

Parameter	Estimated Value	Optimized Value
x	0 ± 5 mm	-0.09 mm
y	0 ± 5 mm	2.62 mm
z	0 ± 5 mm	4.42 mm
Scattering length	5 ± 3 mm	5.7 mm
Absorption length	1 ± 1 m	0.169 m
Reflectivity	0.3 ± 0.1	0.48

Table 6.2: The parameters found by genetic algorithm and comparison to simulation for oWbLS3. The experimental dataset was generated by pulsed light from a 407 nm fiber-coupled laser near the center of the detector.

be shorter than LAB but could nevertheless be desirable for its higher light yield. The measured absorption lengths of pure DIN at 430 nm range from 1 m [104] to 4.2 m [125] and are expected to be lower at shorter wavelengths. The value of 0.169 m

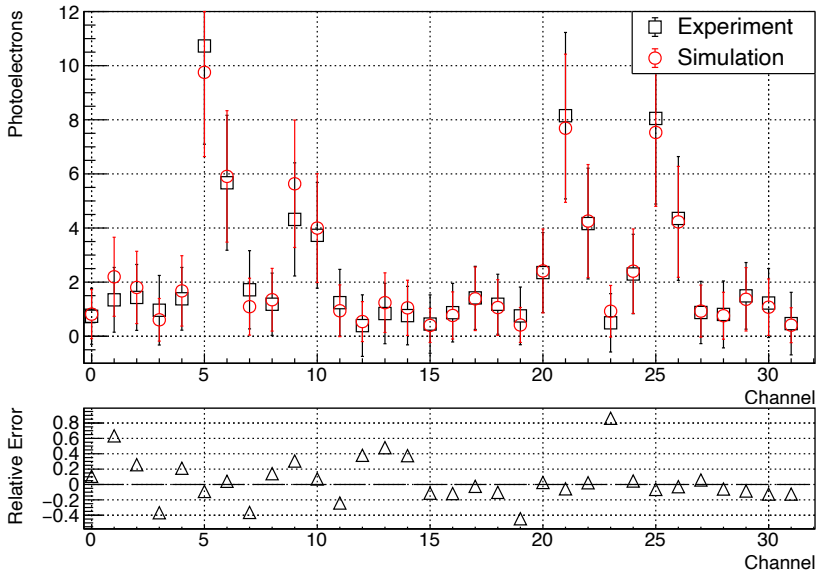

Figure 6.6: A comparison of the average signal in each channel for laser pulses with 20000 ± 2000 photons at a location near the center of the detector. A genetic algorithm was used to find optimal values for six unknown parameters.

found here is therefore lower than expected. There are several possible explanations for this discrepancy. First, the light attenuation during transport in WLS fibers may be greater than modeled. While the model of light transport in the fibers used here was previously validated [74], there are several differences in this iteration from prior experiments. One is that the fibers were occasionally exposed to ambient fluorescent room lighting for a period of about a year, and may have degraded. Secondly, while the fiber bending radius is within the manufacturer's recommendation, the bending necessary to route the fibers to the MAPMT may nevertheless introduce unaccounted losses. Additionally, the oWbLS is not pure DIN and may have a shorter absorption length due to the addition of the surfactant. Additional experiments are planned to directly measure the optical properties of oWbLS.

6.3.3 Gamma-ray response

To a good approximation, the energy deposited in the detector by electrons is linearly proportional to the amount of emitted light. In a traditional scintillator, it is generally desirable for the signal measured to be proportional to the amount of light created. In an opaque scintillator, the amount of light collected in a channel also strongly depends on the proximity of the event to the fiber corresponding to that channel. The summed signal from all channels carries the information on the total energy deposited; however, that information is convolved with the position-dependent light collection efficiency. Figure 6.7 shows the integral detector response for gamma rays from three radioisotopes, for each of the formulations of oWbLS. The general trend is that increased scattering in the liquid increases light collection because fewer photons are absorbed at the walls of the detector.

6.3.4 Comparison to simulation

The experimental and simulated gamma-ray response for the detector filled with oWbLS2 is shown in Fig. 6.8. The parameters used in the simulation were based on those found in Sec. 6.3.2. The absorption length was extrapolated from the measurement at 407 nm to the range of wavelengths 345–455 nm using the shape of the DIN absorption spectrum in Ref. [125]. The value of the scattering length measured at 407 nm was extrapolated to the 342–457 nm range using the $1/\lambda^4$ dependence of the Rayleigh scattering cross-section [126]. The χ^2/NDF values are 1.45 for ^{60}Co, 1.13 for ^{137}Cs, and 1.23 for ^{22}Na.

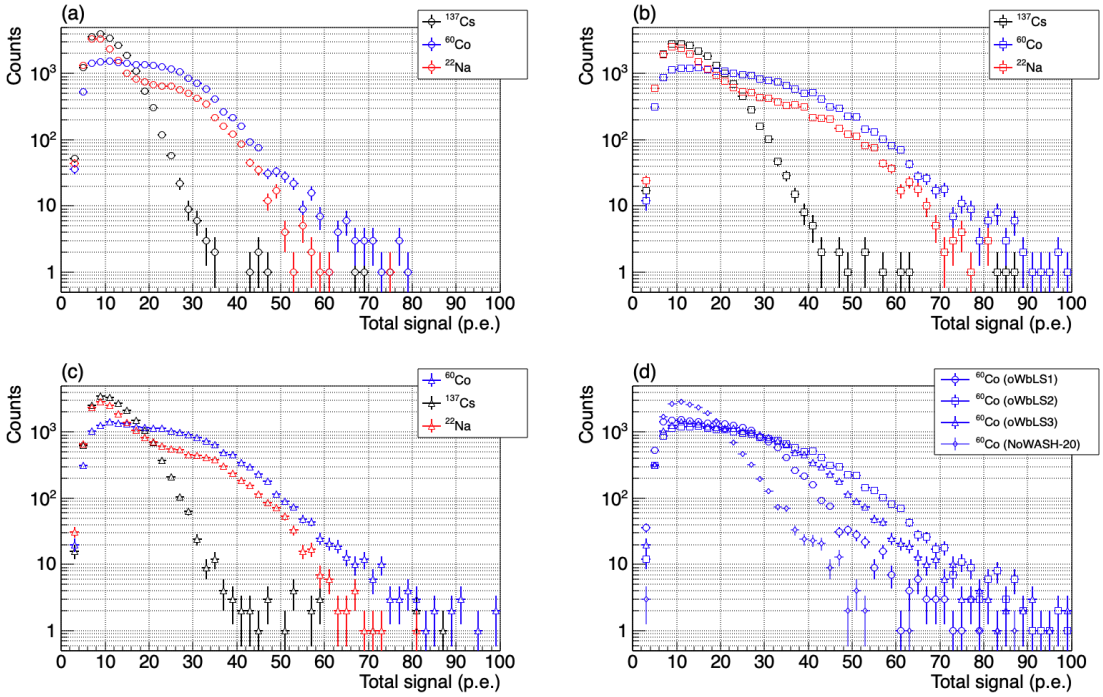

Figure 6.7: Response to gamma rays from three radioisotopes for (a) oWbLS1, (b) oWbLS2, and (c) oWbLS3. Among these, oWbLS1 had the longest scattering length, leading to the sharpest Compton features, while oWbLS2, with the shortest scattering length, provided optimal light collection. (d) Response of the three formulations of oWbLS to gamma rays from ^{60}Co for ease of comparison. It is evident that the light collection efficiency increases as the scattering length decreases. The response of NoWASH-20 is shown for reference; however, a different detector body and set of fibers were used to make this measurement, making it a point of interest rather than a direct comparison.

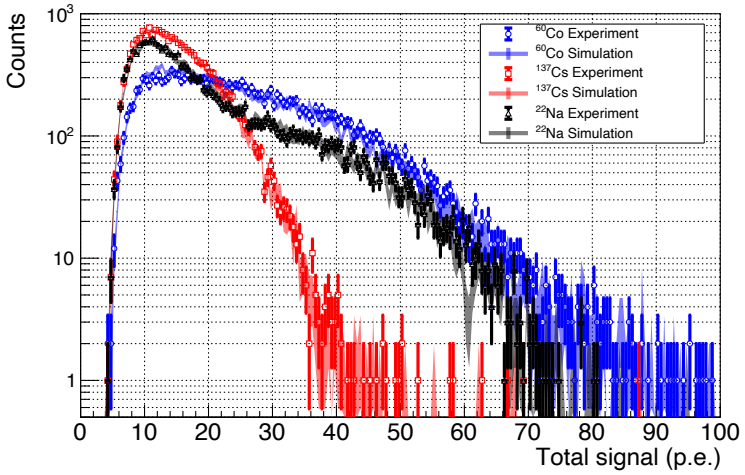

Figure 6.8: The comparison of experimental and simulated detector response for gamma rays from three radioisotopes. The simulation results are shown as a shaded region. The simulation parameters are those described in Table 6.2. More details about the simulation methodology are available in Ref. [74].

6.3.5 Topological reconstruction

6.3.5.1 Center of mass

We investigated the use of channel-by-channel signals for an event to reconstruct event topology. The simplest method to reconstruct the position of the event is to calculate a quantity analogous to the center of mass (CoM) for all channels. For instance, in the z direction:

$$\mathrm{CoM}_z = \frac{\sum_{i=0}^{32} s_i p_{i,z}}{\sum_{j=0}^{32} s_j}, \tag{6.1}$$

where s_j is the signal in the jth fiber, and $p_{j,z}$ is the position of the jth fiber in the z direction. The center of the detector is taken as the origin. As noted in Sec. 6.2.1, while all 32 channels give information about the position of the event in the z direction, only 16 provide information in the x and y directions.

This method has several shortcomings. First, it implicitly assumes that light is created isotropically, which is not the case with this laser injection calibration experiment. Secondly, it does not inherently allow for multiple light centers (though

in principle it could be extended to account for *e.g.* two Compton scatters if the light balls from the two events did not overlap in any dimension and CoM calculations could be done for each region of interest).

The first shortcoming can be partially addressed by systematic correction, *i.e.*, mapping the true source positions in each dimension as a function of the solved CoM positions. This relationship was calculated by simulating 3×10^6 events and creating 2D histograms of the true and apparent positions for each dimension. Then, for each slice of vertical bins (representing a small range of true positions along an axis), a Gaussian distribution was fit to the resulting CoM positions. Lastly, a polynomial (9^{th} order for x and y, and 3^{rd} order for z) function was fit to the Gaussian centroids, and this function was used to transform experimental CoM values to true values. The histograms and fits are shown in Fig. 6.9, illuminating an additional shortcoming of the CoM reconstruction approach: events that take place near the edges of the detector do not result in unique CoM values. This reduces the fraction of the detector volume for which this technique is applicable. The ranges of suitable values (shown as the range of the red fit lines in the plot) are approximately -27 to 27 mm in x and y, and -30 to 40 mm in z. This fiducial region corresponds to a volume of 0.20 L, or about 20% of the overall detector volume. Figure 6.10 shows the results of the CoM reconstruction approach for the 10000 laser pulses obtained from the experiment shown in Fig. 6.5. The number of photons injected corresponds to an event depositing approximately 1.7 MeV in the detector. The bias values are $x = -0.48$ mm, $y = 0.48$ mm, and $z = 4.43$ mm. These shifts arise from a combination of the offset of the true initial position of photon injection and variations in the responses of each channel.

The standard deviations for the three distributions are x: 2.82 mm, y: 2.96 mm,

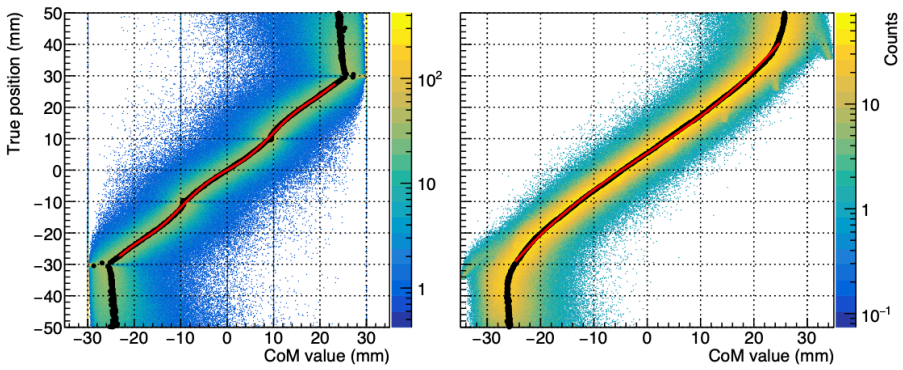

Figure 6.9: Mapping of CoM and true positions of events for the (left) x and y dimensions and (right) the z dimension. The histogram shows true and reconstructed positions for 3×10^6 simulated events that varied in the range of 5000–30000 photons/pulse. The black dots show the centroids of Gaussian distributions fit to slices of the histogram. The red line shows the polynomial fit (9^{th} order for x and y, and 3^{rd} order for z) to the Gaussian centroids.

and z: 2.22 mm. The superior performance in the z direction is due to the increased fiber density and indicates the potential precision of a detector with a fiber pitch of 1 cm. While the distributions of the CoM errors have a Gaussian shape, the transformation from CoM to true positions using the mapping function shown in Fig. 6.9 skews the distributions. The distribution of total position reconstruction error is found by shifting the individual dimensional distributions such that their mean value vanishes (to remove bias originating from uncertainty in the true position of the laser) and calculating the Euclidean distance for each event from the origin. The distribution of total errors for the dataset shown in Fig. 6.12 is shown in Fig. 6.11. The distribution has a mean value of 4.35 mm and a standard deviation of 2.15 mm. This experiment was repeated for four positions in the detector with two pulse intensities. The large pulses had an intensity of 20000 ± 2000 photons/pulse, which correlates to approximately 1.65 MeV of energy deposition in oWbLS. The small pulses had an intensity of 10000 ± 1000 photons/pulse, which is equivalent to 0.82 MeV of energy deposited in the detector. The four positions, along with their nominal offsets from the center of the detector, are listed in Table 6.3. The results

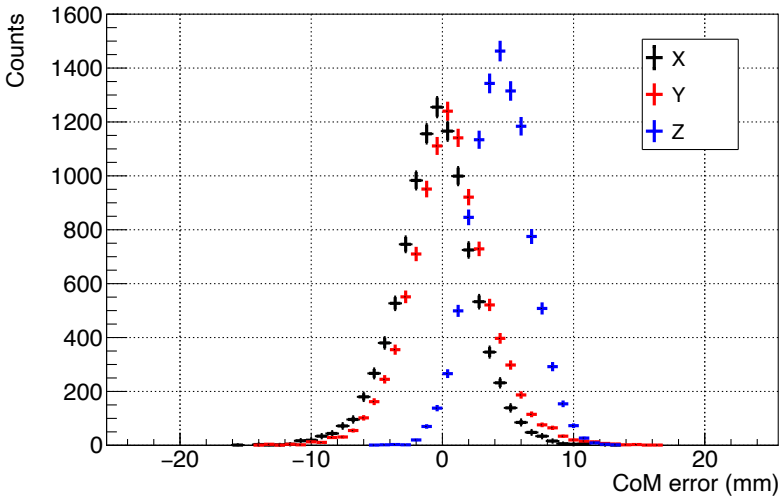

Figure 6.10: Distribution of position reconstruction errors from the CoM method in each dimension for pulses of approximately 20000 photons/pulse at a nominal position of $(0, 0, 0)$. As expected, the distributions of errors in x and y have similar widths, and the distribution of errors in z is narrower due to the increased fiber density in this direction.

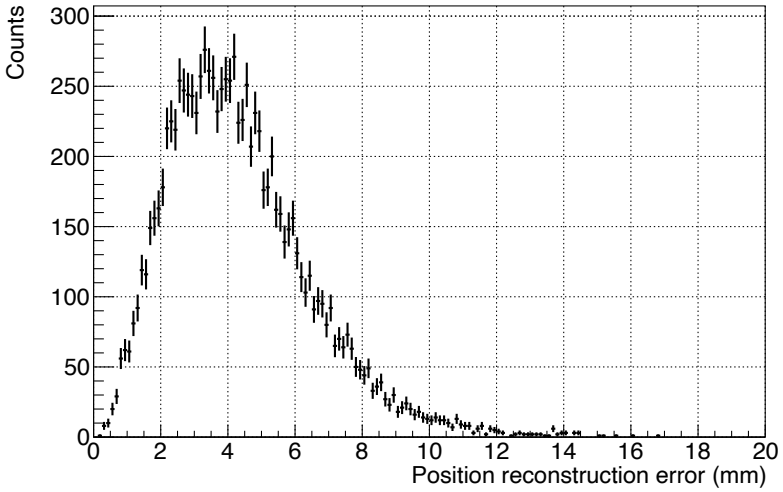

Figure 6.11: Distribution of position reconstruction errors using the CoM method for a point-like event comprising approximately 20000 initial photons near the center of the detector, with a mean of 4.35 mm and a standard deviation of 2.15 mm.

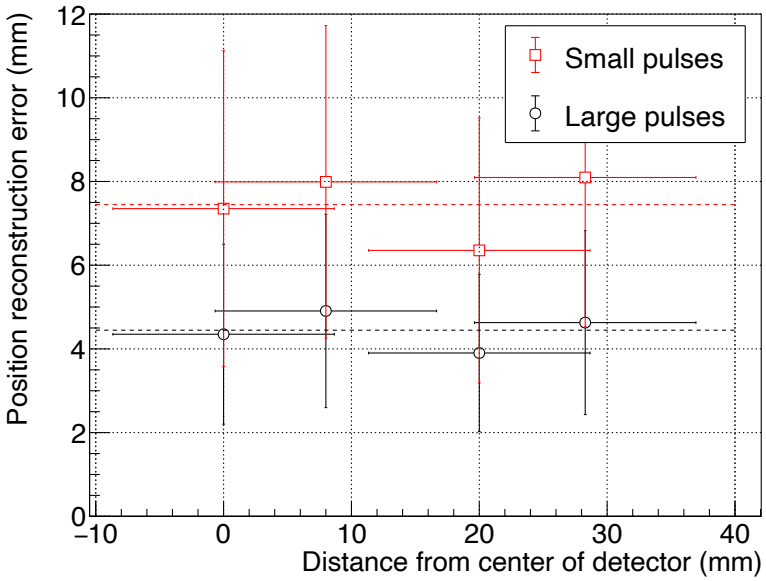

Figure 6.12: Position reconstruction errors for the detector positions listed in Table 6.3. The large pulses had an intensity of 20000 ± 2000 photons/pulse, and the small pulses were 10000 ± 1000 photons/pulse. The average reconstruction error (shown as dotted horizontal lines) for the large pulses was 4.4 mm and for the small pulses was 7.4 mm. The horizontal error bars represent the uncertainty in offset from the center of the detector, and the vertical error bars show the standard deviation of the reconstruction position errors.

of CoM analysis are shown in Fig. 6.12.

Position	x (mm)	y (mm)	z (mm)	Nominal offset (mm)
1	0 ± 5	0 ± 5	0 ± 5	0 ± 9
2	0 ± 5	-8 ± 5	0 ± 5	8 ± 9
3	0 ± 5	-20 ± 5	0 ± 5	20 ± 9
4	20 ± 5	-20 ± 5	0 ± 5	28 ± 9

Table 6.3: Positions used for light injection experiments to assess variations in reconstruction precision.

6.3.5.2 Machine learning

In an attempt to improve upon the precision of event position reconstruction achieved using the CoM method, extend the fiducial region of the detector, and allow for the reconstruction of event intensity, a machine learning algorithm, called HITMAN, was investigated. The method chosen is based on Ref. [127], in which a neural network is trained by simulated data to recognize event characteristics given

a series of observables (in this case, the number of photoelectrons in each channel). This method differs from traditional neural networks in that the algorithm generates not simply reconstructed parameter values, but a probability density estimation of the likelihood function for each desired output.

The Geant4 model described in Sec. 6.3.4 was used to generate a dataset comprising 4×10^6 events. The events had photon intensities between 5000–30000 photons/pulse and had randomized positions throughout the interior of the detector. To be compatible with our fiber-coupled laser experimental dataset, all photons were given an initial momentum in the $-z$ direction.

Two methods of reconstruction were considered. The first is a maximum likelihood approach, in which the reconstructed value is the maximum value of the likelihood function produced by HITMAN. This method is referred to as the MLE (maximum likelihood estimation) method. The second method relied on Bayesian inference. The posterior mean of each parameter value was calculated by assuming a uniform prior. This implies the use of the mean squared error as the loss function, and the set of reconstructed values constitutes a minimum mean squared error value. The expected value of the position of the event in the x dimension given a set of observables θ is calculated as

$$E[x|\theta] = \int x \left[\int p(x,y,z,I)\, L(x,y,z,I|\theta)\, dy\, dz\, dI \right] dx, \tag{6.2}$$

where $p(x,y,z,I)$ is the uniform prior distribution for x, y, and z dimensions, as well as the event intensity I, and $L(x,y,z,E|\theta)$ is the likelihood function generated by HITMAN given observables θ.

The process is repeated for each reconstructed parameter. This method, henceforth referred to as MMSE, was intended to address the presence of artifacts in the reconstruction space, which will be further discussed below.

To assess the behavior of the HITMAN, 10^5 events with an intensity of 20000 photons were simulated with randomized positions in the detector volume. Reconstructions of x, y, and z positions were then calculated, along with a reconstruction of the event intensity. The results for the MLE approach are shown in Fig. 6.13 and the results for the MMSE approach are shown in Fig. 6.14.

The reconstructions from the MLE method show a good correlation with the true values of the spatial dimensions within the boundaries of the fibers (-30 to 30 mm in x and y, and -35 to 35 mm in z), but beyond that region the distribution of reconstructed values for a given true value become complex. Artifacts in the reconstruction space are visible as streaking, especially near the fiber locations. The mean and standard deviation for the intensity reconstructions were 18900 ± 7000 photons. The large number of intensity reconstructions with 5000 or 30000 photons is an artifact of the cutoff intensities in the training dataset.

The distribution of reconstructions from the MMSE estimator calculated with Eq. (6.2) resembles the results for the CoM analysis shown in Fig. 6.9. Similarly to the maximum likelihood and CoM method, reconstructions outside of the boundaries of the fiber lattice are not feasible. While the spatial reconstructions are qualitatively poorer, the intensity reconstructions are much better than those achieved with the maximum likelihood method: the mean and standard deviation for the intensity reconstructions were 19300 ± 4000 photons.

Again using the spatially uniform simulated dataset, a comparison of performance between the corrected CoM and HITMAN (MLE method) reconstructions can be made in the fiducial region (-27 to 27 mm in x and y, and -30 to 40 mm in z). The results are shown in Fig. 6.15. HITMAN MLE provided more accurate reconstructions, with a mean reconstruction error of 4.9 ± 3.3 mm, whereas the

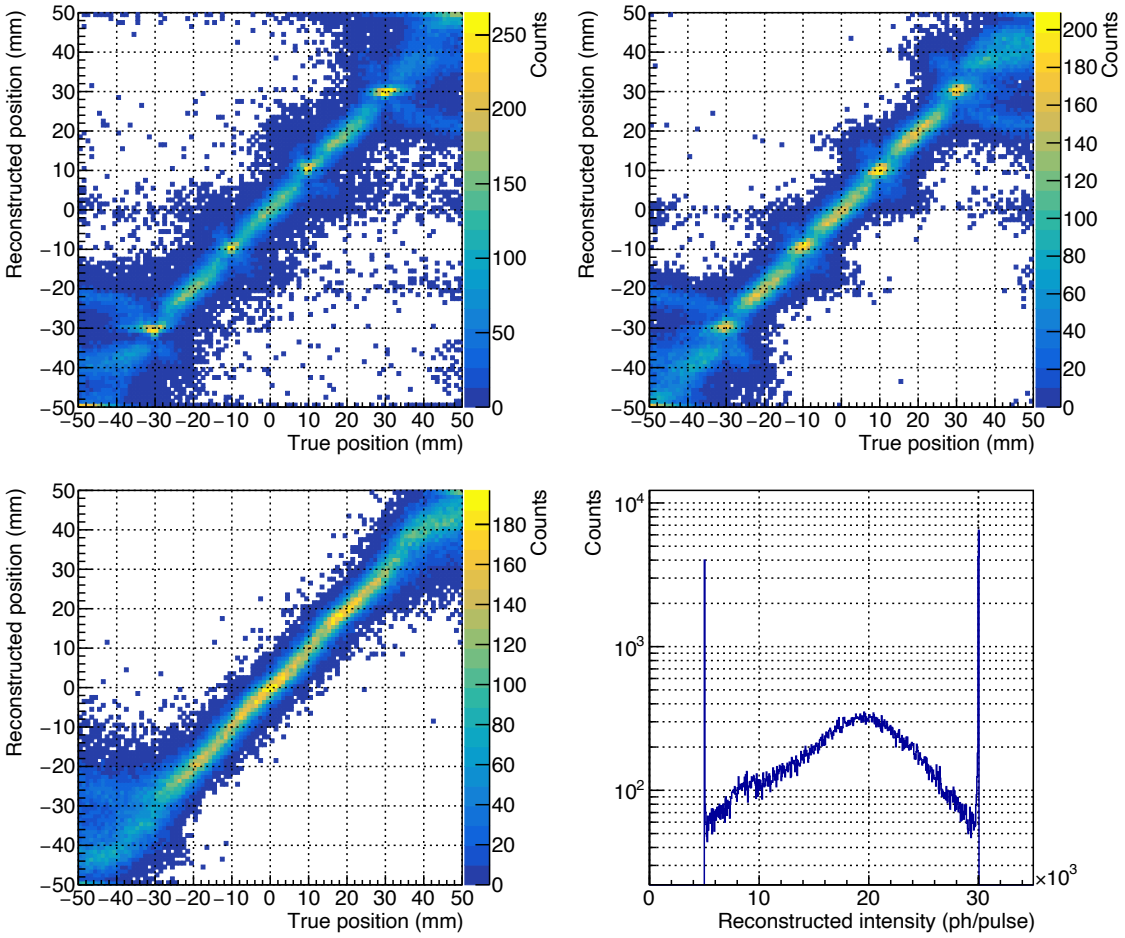

Figure 6.13: The reconstruction results from HITMAN. The reconstructions are of 10^5 spatially homogenous simulated events with 20000 photons using the MLE method. The top left panel shows the reconstructions in the x dimension, the top right shows the y dimension, and the bottom left shows the z dimension. A perfect set of reconstructions would show a horizontal line, corresponding to a perfect correlation between the true and reconstructed values. The bottom right panel shows reconstructions of intensity.

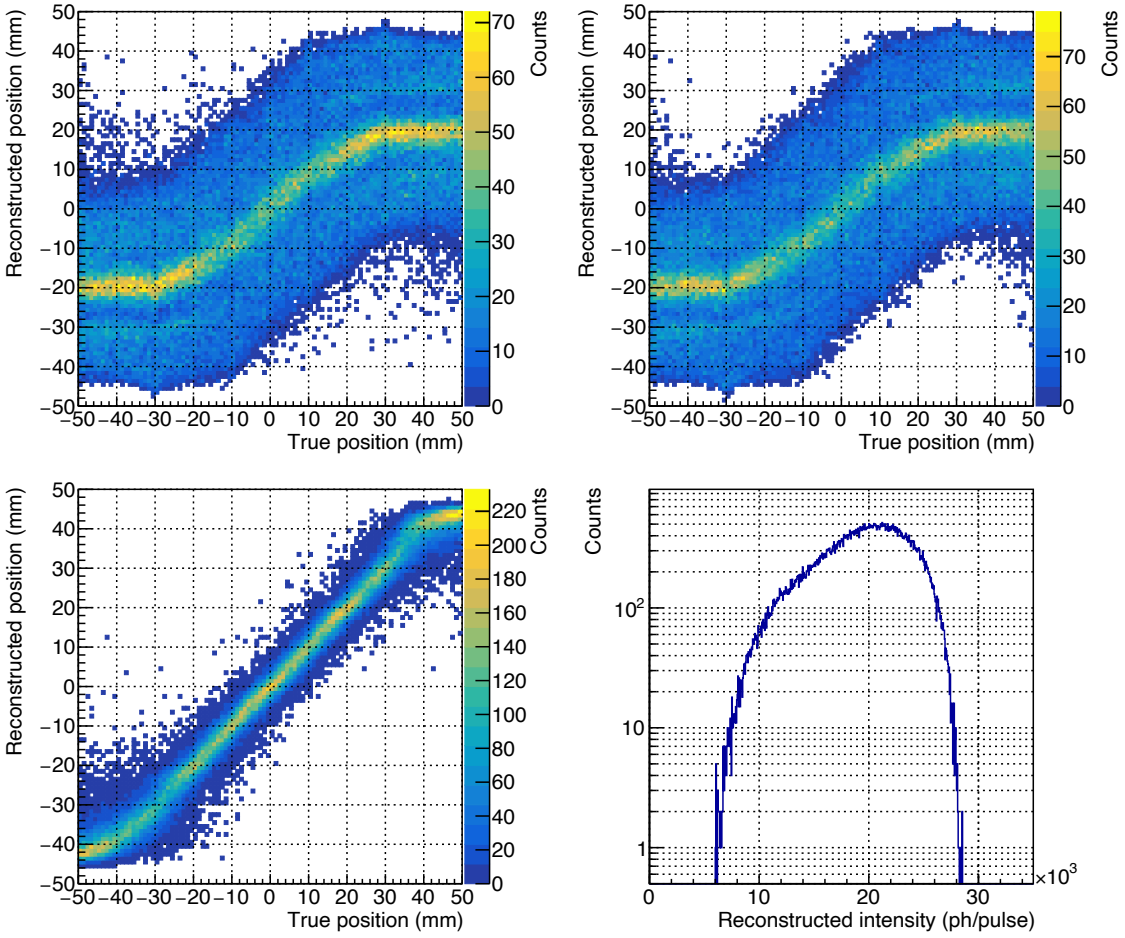

Figure 6.14: Additional reconstruction results from HITMAN. The reconstructions are of 10^5 spatially homogenous simulated events with 20000 photons using the MMSE. Similarly to Fig. 6.13, the top left panel shows the reconstructions in the x dimension, the top right shows the y dimension, and the bottom left shows the z dimension. The bottom right panel shows reconstructions of intensity.

corrected CoM method mean error was 5.5 ± 2.9 mm.

While HITMAN (MLE) performs better on average in the fiducial region than corrected CoM on simulated data, the comparison is more complicated for the experimental datasets. For some locations, HITMAN (MLE) outperforms the corrected CoM analysis, as expected from the simulated data. However, for other positions, artifacts distort the reconstruction distributions sufficiently that the corrected CoM method provides superior results. Figures 6.16 and 6.17 provide illustrations of the machine learning algorithm over-performing and under-performing corrected CoM for experimental data, respectively.

The origin of the bimodality of the y dimension reconstructions in Fig. 6.17 is unclear. The events in each group are not obviously different from one another. There are several possible explanations. First, the reconstruction algorithm may be sensitive to differences in channel response, which are not included in the training data, but are likely present in the experimental apparatus as a result of variations in fiber condition, coupling quality, and local inhomogeneities in oWbLS optical properties. Secondly, the source of the bimodality may be artifacts in the likelihood functions generated by HITMAN. These could be indicative of an insufficiently large training dataset, among other potential factors. The effects of these artifacts on reconstructions are visible as streaks in Fig. 6.13. While the MMSE method shown in Fig. 6.14 removes the artifacts, it also results in a larger average reconstruction error.

While HITMAN failed to improve the precision of the corrected CoM method for events from experimental data in some of the fiducial volume, it has several advantages that make it attractive to continue to pursue. First, it has the ability to incorporate time-of-arrival information for each detected photon. That information

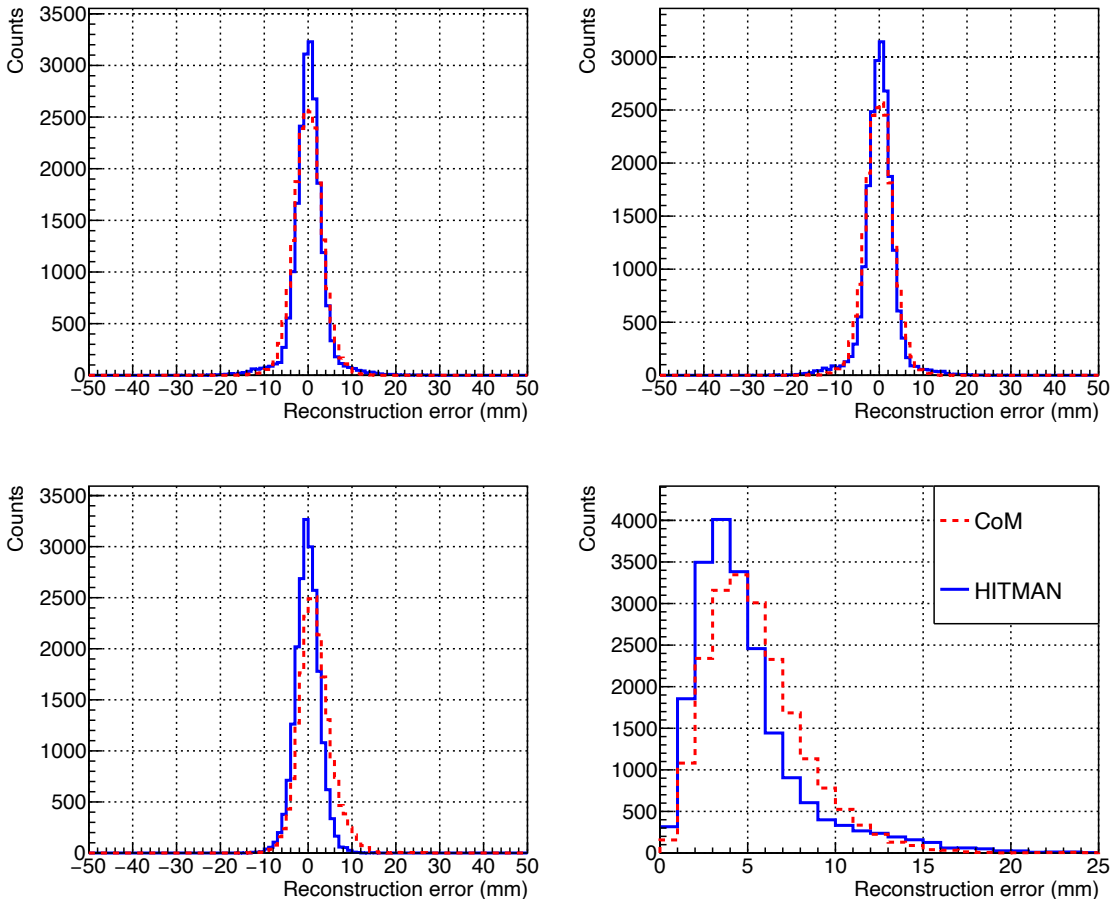

Figure 6.15: A comparison of the reconstruction quality within the fiducial region of the detector using simulated events comprising 20000 photons. The top left panel shows the x direction, the top right panel shows y, and the bottom left shows z. The bottom right panel shows the total reconstruction error. The mean reconstruction error of the corrected CoM method was 5.5 ± 2.9 mm whereas the HITMAN MLE method had a mean error of 4.9 ± 3.3 mm.

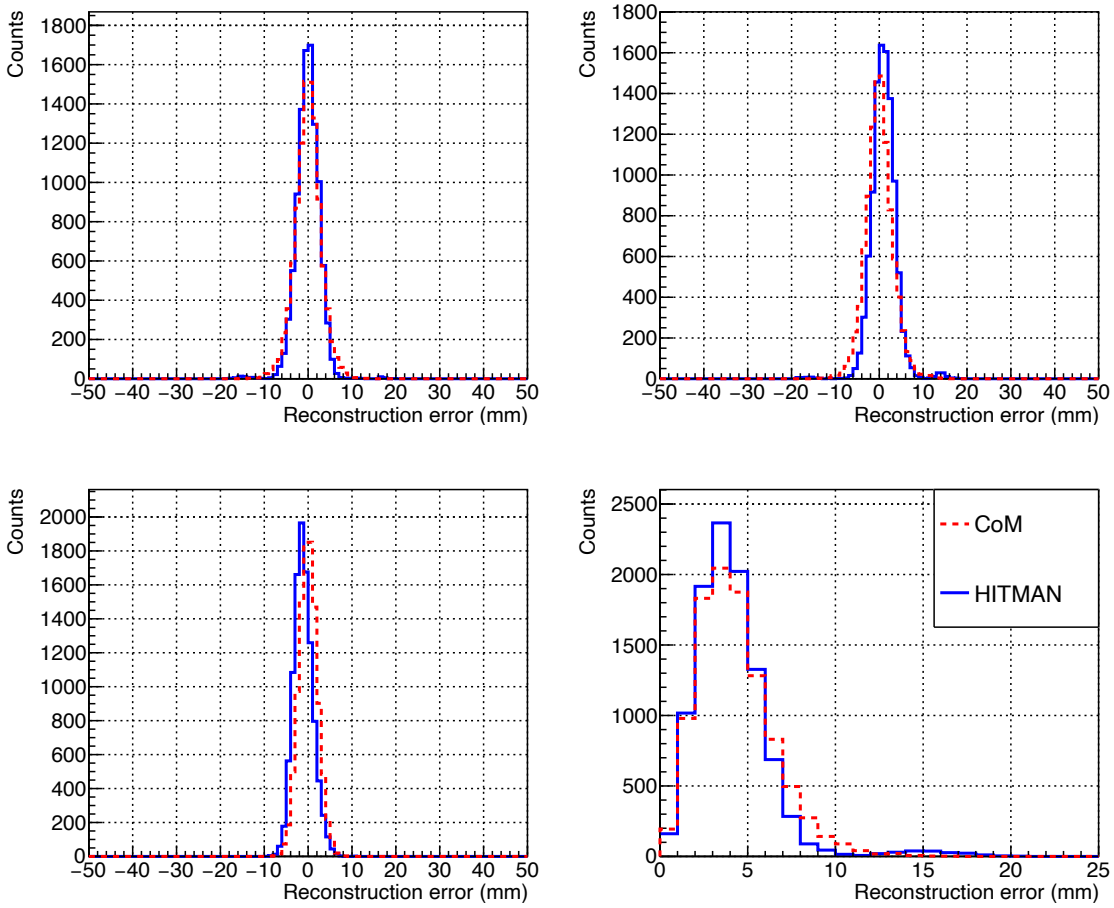

Figure 6.16: Machine learning (HITMAN) and CoM reconstructions on experimental data from pulses of 20000 ± 2000 photons. The nominal true event positions were $(0, 0, 0)$ mm, with a 5 mm uncertainty in each direction. The top left panel shows the x direction, the top right panel shows y, and the bottom left shows z. The bottom right panel shows the total reconstruction error. The mean error for HITMAN was 4.1 ± 2.3 mm and 4.3 ± 2.1 mm for the corrected CoM method. The machine learning algorithm outperformed the CoM analysis.

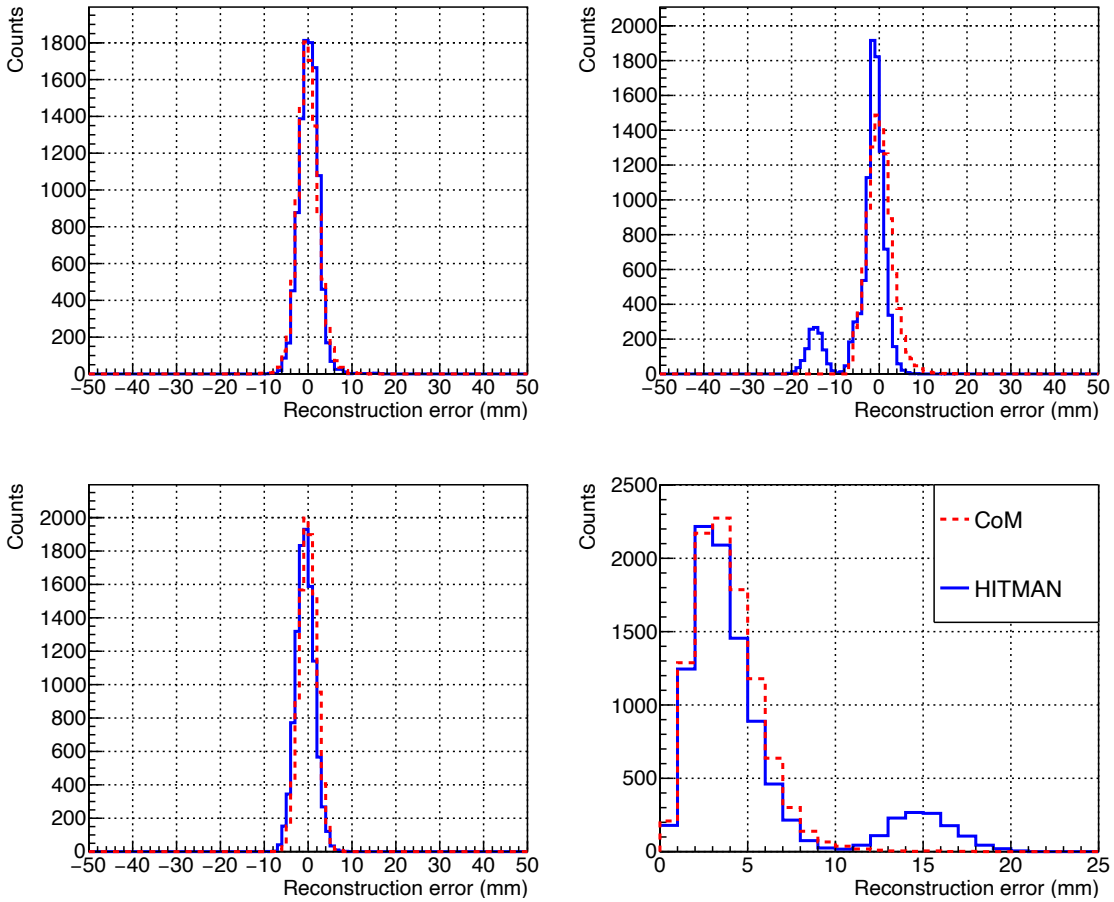

Figure 6.17: Machine learning (HITMAN) and CoM reconstructions on experimental data from pulses of 20000 ± 2000 photons. The nominal true event positions were $(0, -20, 0)$ mm, with a 5 mm uncertainty in each direction. The top left panel shows the x direction, the top right panel shows y, and the bottom left shows z. The bottom right panel shows the total reconstruction error. The mean error for HITMAN was 5.0 ± 4.1 mm and 3.9 ± 1.9 mm for the corrected CoM method. The machine learning algorithm failed to outperform the CoM analysis, primarily due to the bimodality of reconstructions in the y direction.

was not used here, because it was not accessible from the data acquisition system. However, future designs using SiPMs may allow for the recovery and usage of this granular timing information. Secondly, HITMAN allows for the direct inference of other characteristics of an event, such as particle type and incident direction, if such information is coded into the event topology. Lastly, it can natively discern between single and multi-interaction events, which would confound the CoM method. Additionally, given the superior performance of HITMAN on simulated data, it is possible that by improving the modeling of the detector, for instance by including channel response variations, reconstructions could be generally improved beyond what is possible with CoM analysis. Further improvements to the algorithm are ongoing.

6.3.6 Energy Resolution

The position-dependent energy resolution was calculated from the same datasets that were used for the CoM analysis. In addition, two positions outside the fiducial region were also included. These positions were $(20, -40, 0)$ mm and $(-40, -40, 0)$ mm. To determine the energy resolution, the total signal spectra for pulses of two different heights at each position were fit to a Gaussian shape, with mean μ and standard deviation σ. The energy resolution is then

$$\frac{\Delta E}{E} = \frac{\text{FWHM}}{\mu}, \tag{6.3}$$

where

$$\text{FWHM} = 2.35\sigma \tag{6.4}$$

is the full width at half maximum of the Gaussian fit. An example of the total signal spectra for one position and energy resolutions for all six positions are shown

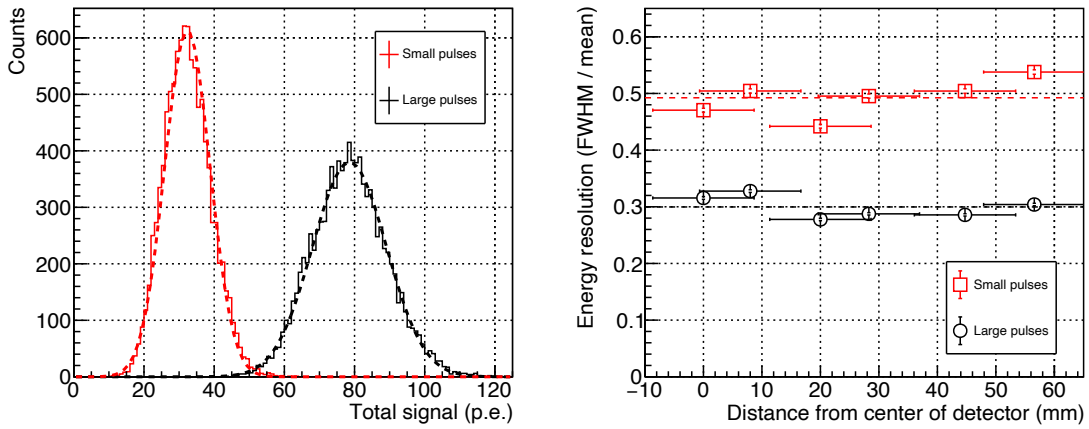

Figure 6.18: (Left) Distribution of p.e. per pulse for light injected into the center of the detector. Each distribution is fit with a Gaussian, shown as a dotted line. (Right) Energy resolution as a function of distance from the center of the detector. The energy resolution values are calculated from the Gaussian fitting of the individual total signal distributions. The mean energy resolution values for large (20000 ± 2000 photons/pulse) and small (10000 ± 1000 photons/pulse) pulses are shown as a dotted line.

in Fig. 6.18. The energy resolution for large pulses (corresponding to 1.6 MeV) was 30 ± 2 %, whereas for the small pulses (corresponding to 0.8 MeV) was 49 ± 3 %. The uncertainties are the standard deviations of the set of energy resolutions reconstructed from all positions.

This measurement does not account for the intrinsic energy resolution of the scintillation liquid, which arises from the statistical fluctuation in the number of scintillation photons produced at a given energy deposition. The intrinsic energy resolutions for various scintillation liquids based on LAB and pseudocumene were found to vary in the range of 1.3–3.3% [128]. While a similar measurement has not been done for oWbLS, the contribution of oWbLS to the obtained energy resolution is likely in the same range. Using laser pulses to determine energy resolution also introduces broadening as a result in the variance in intensity of the laser pulses The laser used in this experiment has a pulse-to-pulse stability of < 5 % [129], which partially offsets the error related to the intrinsic energy resolution of oWbLS.

6.4 Conclusion

A 32-channel, 1 L organic gamma-ray detector capable of spectroscopy and topological reconstruction for point-like events was demonstrated. The position reconstruction precision was 4.4 mm for events of an intensity corresponding to 1.7 MeV and 7.4 mm for events of 0.8 MeV.

6.4.1 Discussion

A useful comparison with this performance is to a hypothetical detector volume with cubical, physically segmented voxels. If the events are homogeneously distributed and all reconstructed to the center of the voxel in which they took place, the mean reconstruction error is

$$\bar{e} = \frac{1}{L^3} \int_{L/2}^{L/2} \int_{L/2}^{L/2} \int_{L/2}^{L/2} \sqrt{x^2 + y^2 + z^2}\, dx\, dy\, dz, \tag{6.5}$$

which evaluates to approximately $0.48L$, where L is the side length of the cubical voxel. The number of voxels required to achieve a mean position reconstruction error of 4.4 mm can therefore be calculated by

$$L = 4.4 \text{ mm}/0.48 = 9.17 \text{ mm}. \tag{6.6}$$

Segmenting the fiducial region of the cube with voxels of this size would require approximately 265 voxels. The 7.4 mm position reconstruction error obtained with events corresponding to 0.8 MeV could be achieved with approximately 56 voxels, or about double the number of channels used in this prototype. Moreover, this technique allows an enormous advantage when scaling up the detector volume. For example, adding another ring of fibers, (*i.e.*, a 6×6 grid as opposed to the current 4×4 per side) to create a fiducial volume of approximately 1 L would require an

additional 40 channels, but approximately another 1000 physically segmented voxels of side length 9.17 mm.

3D reconstruction can also be achieved with a detector that employs 2D voxels (rods). The position reconstruction in the third dimension may be accomplished by comparing the time of flight for the scintillation photons [20] at each end of the rods. Since the readout array is laid out in two planes, the number of channels scales similarly with volume to the detector described in this study. Furthermore, the energy resolution of such a system can reach 18-22% at the ^{137}Cs Compton edge, which is superior to the results shown in Sec. 6.3.6. However, there are two disadvantages of the rod technique compared to an opaque scintillator. Firstly, sub-voxel position resolution is generally not achievable in the dimensions orthogonal to the rods, whereas sub-fiber pitch resolution has been demonstrated here for opaque scintillators. Secondly, fast-timing electronics are necessary to reconstruct the position along the rods. While timing information may be useful in other opaque scintillator designs, it was not used here beyond the correlation of pulses into events.

6.4.2 Future work

Several improvements can be made to the design presented here. The locations of the fibers could be optimized to maximize the fiducial region while minimizing reconstruction error. An analysis of the variations in individual channel response could help identify the source of bimodality in HITMAN reconstructions and could inform improved simulations for better training datasets. The optical properties of oWbLS could be improved to have a longer absorption length and shorter scattering length, as well as greater long-term stability. Lastly, better spectral matching for the scintillation cocktail, fibers, and photosensors would increase the detected signal, and increase the detector performance both in energy resolution and the quality of

event topological reconstruction.

CHAPTER VII

Conclusion

This chapter provides an overview and context for the major results discussed in this thesis. Following that summary, several opportunities for extensions and applications of virtually segmented detectors are examined.

7.1 Review of objectives

Segmented scintillation radiation detector systems can solve problems that are difficult to address with traditional single-volume scintillators. The key piece of information available in segmented detector systems is event topology, or the spatial distribution of energy deposition in the active volume.

Reconstruction of event topology is seldom an end in and of itself, but is rather a means to determining information about the measured event, potentially including source direction, particle type, and whether multiple interactions took place, which could be an indication of pileup. One method to achieve segmentation is to separate a scintillation volume into physical voxels, usually through the insertion of reflective boundaries at voxel edges. This approach is effective but can be difficult to instrument, especially as the detector volume grows in size. Another approach is to virtually segment the detector by introducing scattering into the bulk medium. In this paradigm, the number of channels required may be reduced by achieving

sub-voxel topological reconstruction precision.

This thesis investigated several novel approaches and applications of both physically and virtually segmented detector systems. The results provide new avenues to the radiation detection community in solving problems that require event topological reconstruction.

7.2 Major results

Chapter II presented a new method for measuring the spectral characteristics of an extremely short pulses of high-energy gamma rays. The method was modeled and prototyped in an experiment. By requiring the gamma rays to first Compton scatter, the Klein-Nishina differential cross section could be sampled by an array of detectors, which together function as a single, physically segmented detector system. The total energy deposited in each detector was used to surmise the energy characteristics of a gamma-ray pulse. The following chapters all focused on opaque scintillators, a type of virtually segmented detector. Chapter III explored the theory of light transport of collection germane to opaque scintillator detectors. In addition to informing the modeling process used in later chapters, the main sources of signal loss in a detector of this type were quantified, with the trapping efficiency of the fibers chief among them. Chapter IV describes an experimental study of light collection efficiency from opaque liquids using WLS fibers. In addition to providing the first experimental evidence that a measurable quantity of scintillation light could be extracted from such a system, a Monte Carlo particle transport model was constructed and experimentally validated, which proved critical to the experimental work in the following chapters. Chapter V detailed the design, fabrication, and characterization of the first aluminum 1 L cube prototype, using NoWASH-20 as a fill liquid. The prototype had

32 WLS fibers in two orthogonal directions for three-dimensional event topological reconstructions. It was capable of distinguishing between gamma-ray spectra from two radioisotopes and demonstrated source localization via event topology. The final chapter described the production and characterization of the second prototype detector, which had the same geometry as the first prototype but was constructed using additive manufacturing techniques from an acrylic-like material. The detector exhibited superior light production and collection compared to the first prototype and was capable of reconstruction of the event topology for point-like events with a precision of less than 5 mm.

7.3 Future work

A hallmark of the unexplored research landscape is that for every problem solved, new ideas and opportunities rapidly present themselves. Virtually segmented detectors based on scattering, a technology currently in its infancy, are a perfect example of this phenomenon. This thesis presents work that validates the feasibility of opaque scintillators and demonstrates their power in event topological reconstruction, but there are many more possibilities to improve their performance and deploy them in applications.

First, an apparatus to optically characterize opaque liquid scintillators should be developed, potentially by imaging the diffuse reflectance pattern on the surface of the liquid in response to an incident pencil beam of light, as is done in Refs. [130, 131].

The detectors presented in Chs. V and VI were not optimized for a particular application. The quality of the topological reconstruction could almost certainly be improved by tuning the positioning and pitch of the WLS fibers. A detector of a larger size would naturally have less fractional volume close to the walls, and thus

a larger fiducial region. Detectors with mixed fiber types should be investigated to optimize the light trapping in the fibers. For example, the presence of both UV-blue shifting fibers and blue-green shifting fibers would allow photons that had been shifted once and escaped a fiber another chance at being detected. This could greatly increase the efficiency of a detector based on opaque scintillation if the bulk absorption length of the fill liquid is long enough such that most photons are absorbed in a fiber before being absorbed by the bulk medium.

Using silicon photomultipliers (SiPMs) instead of a single MAPMT could have at least two benefits, including a higher quantum efficiency and the ability to place the photosensors right on the outside of the detector volume, which would reduce the length and bending of the WLS fibers. This would, in turn, reduce light loss, and lead to greater efficiency. Between this upgrade and the more complex fiber types discussed above, an approximately threefold increase in efficiency may be achievable using today's technology.

Many materials can be investigated for opaque scintillation applications. For example, plastics and pressed organic polycrystals can be made highly scattering [132]. Additionally, the reduction in the transparency requirements for detectors that use this technology raises exciting possibilities for detector doping at unprecedented levels with, for example, nanoparticles that include material with a high atomic number to increase both light scattering and the photoelectric absorption of gamma rays [133, 134].

Lastly, the base solvent used in oWbLS (DIN) has been shown to have the ability to discriminate between neutron and gamma-ray scatters based on the difference in the resulting pulse shape. The feasibility of this approach in the opaque regime should be investigated.

7.4 Summary

In summary, segmented detector systems provide a rich tapestry of information about the way in which incident radiation interacts with matter. This information, along with calorimetry, can provide insights germane to many problems in radiation detection. The work presented here helps to advance the understanding of some of the fundamental processes that govern such systems, as well as sheds light on potential next steps and promising applications.

BIBLIOGRAPHY

BIBLIOGRAPHY

[1] K. Hoedt-Rasmussen, E. Sveinsdottir, and N. Lassen, "Regional Cerebral flow in Man Determined by Inral-artrial Injection of Radioactive Intert Gas," *Circulation Research*, vol. 18, no. 3, pp. 237–247, 1966.

[2] M. P. Belousov, M. V. Gromyko, and O. V. Ignatyev, "Scintillation γ spectrometers for use at nuclear power plants (review)," 1 2017.

[3] M. L. McConnell, "Scintillation Detectors for X-ray and gamma-ray Astronomy," in *The WSPC Handbook of Astronomical Instrumentation*, 6 2021, pp. 27–50.

[4] P. Kerr, M. Rowland, D. Dietrich, W. Stoeffl, B. Wheeler, L. Nakae, D. Howard, C. Hagmann, J. Newby, and R. Porter, "Active detection of small quantities of shielded highly-enriched uranium using low-dose 60-kev neutron interrogation," *Nuclear Instruments and Methods in Physics Research, Section B: Beam Interactions with Materials and Atoms*, vol. 261, no. 1-2 SPEC. ISS., pp. 347–350, 8 2007.

[5] W. K. Röntgen, "Über eine neue Art von Strahlen: vorläufige Mitteilung," *Sitzungsber. Phys. Med. Gesell.*, 1895.

[6] C. Britt, X. Wen, H. Qi, and J. P. Hayward, "Directionality for wearable, closely packed radiation detector arrays," *Nuclear Instruments and Methods in Physics Research, Section A: Accelerators, Spectrometers, Detectors and Associated Equipment*, vol. 986, 1 2021.

[7] O. Gal, C. Izac, F. Lainé, and A. Nguyen, "CARTOGAM: a portable gamma camera," *Nuclear Instruments and Methods in Physics Research Section A: Accelerators, Spectrometers, Detectors and Associated Equipment*, vol. 387, no. 1-2, pp. 297–303, 3 1997.

[8] H. O. Anger, "Scintillation camera," *Review of Scientific Instruments*, vol. 29, no. 1, pp. 27–33, 1958.

[9] E. Caroli, J. B. Stephen, G. Di Cocco, L. Natalucci, and A. Spizzichino, "Coded aperture imaging in X- and gamma-ray astronomy," *Space Science Reviews*, vol. 45, no. 3-4, pp. 349–403, 9 1987.

[10] D. B. Everett, J. S. Fleming, R. W. Todd, and J. M. Nightingale, "Gamma-radiation imaging system based on the Compton effect," *Proceedings of the Institution of Electrical Engineers*, vol. 124, no. 11, pp. 995–1000, 1977.

[11] G. W. Phillips, "Gamma-ray imaging with Compton cameras," *Nuclear Instruments and Methods in Physics Research Section B: Beam Interactions with Materials and Atoms*, vol. 99, no. 1-4, pp. 674–677, 5 1995.

[12] N. Mascarenhas, J. Brennan, K. Krenz, P. Marleau, and S. Mrowka, "Results with the neutron scatter camera," *IEEE Transactions on Nuclear Science*, vol. 56, no. 3, pp. 1269–1273, 6 2009.

[13] R. A. Winyard, J. E. Lutkin, and G. W. McBeth, "Pulse shape discrimination in inorganic and organic scintillators. I," *Nuclear Instruments and Methods*, vol. 95, no. 1, pp. 141–153, 8 1971.

[14] D. L. Horrocks, "Pulse Shape Discrimination with Organic Liquid Scintillator Solutions," *Applied Spectroscopy*, vol. 24, no. 4, pp. 397–404, 7 1970.

[15] H. Rebber, "Event Discrimination with Topological 3D Reconstruction at MeV Energies in the JUNO Experiment," Ph.D. dissertation, Staats-und Universitätsbibliothek Hamburg Carl von Ossietzky, Hamburg, 2019.

[16] H. Miyadera, H. Miyadera, and C. L. Morris, "Muon scattering tomography: review," *Applied Optics, Vol. 61, Issue 6, pp. C154-C161*, vol. 61, no. 6, pp. C154–C161, 2 2022. [Online]. Available: https://opg.optica.org/viewmedia.cfm?uri=ao-61-6-C154&seq=0&html=truehttps://opg.optica.org/abstract.cfm?uri=ao-61-6-C154https://opg.optica.org/ao/abstract.cfm?uri=ao-61-6-C154

[17] S. W. Tang, Y. H. Yu, Y. Zhou, Z. Y. Sun, X. H. Zhang, S. T. Wang, K. Yue, L. X. Liu, F. Fang, D. Yan, Y. Sun, and Z. M. Wang, "A large area plastic scintillation detector with 4-corner-readout," *Chinese Physics C*, vol. 40, no. 5, 5 2016.

[18] J. Balajthy, J. Brown, E. Brubaker, B. Cabrera-Palmer, J. Cates, B. L. Goldblum, M. Folsom, P. Hausladen, K. Keefe, J. Nattress, V. Negut, K. Nishimura, J. Steele, and K. Ziock, "Characterization of a SiPM-based monolithic neutron scatter camera using dark counts," *arXiv*, 9 2023. [Online]. Available: http://arxiv.org/abs/2309.15280

[19] V. A. Li, T. M. Classen, S. A. Dazeley, M. J. Duvall, I. Jovanovic, A. N. Mabe, E. T. Reedy, and F. Sutanto, "A prototype for SANDD: A highly-segmented pulse-shape-sensitive plastic scintillator detector incorporating silicon photomultiplier arrays," *Nuclear Instruments and Methods in Physics Research, Section A: Accelerators, Spectrometers, Detectors and Associated Equipment*, vol. 942, 10 2019.

[20] F. Sutanto, T. M. Classen, S. A. Dazeley, M. J. Duvall, I. Jovanovic, V. A. Li, A. N. Mabe, E. T. Reedy, and T. Wu, "SANDD: A directional antineutrino detector with segmented 6Li-doped pulse-shape-sensitive plastic scintillator," *Nuclear Instruments and Methods in Physics Research, Section A: Accelerators, Spectrometers, Detectors and Associated Equipment*, vol. 1006, 8 2021.

[21] K. Keefe, H. Alhajaji, E. Brubaker, A. Druetzler, A. Galindo-Tellez, J. Learned, P. Maggi, J. J. Manfredi, K. Nishimura, B. P. Souza, J. Steele, M. Sweany, and E. Takahashi, "Design and Characterization of an Optically Segmented Single Volume Scatter Camera Module," *IEEE Transactions on Nuclear Science*, vol. 69, no. 6, pp. 1267–1279, 6 2022.

[22] H. Song, Z. Wu, H. Zhang, J. Li, and R. Qiu, "A simulation optimization design of the filter stack spectrometer for laser-plasma interaction experiment," *Journal of Instrumentation*, vol. 18, no. 3, 3 2023.

[23] D. R. Rusby, C. D. Armstrong, C. M. Brenner, R. J. Clarke, P. McKenna, and D. Neely, "Novel scintillator-based x-ray spectrometer for use on high repetition laser plasma interaction experiments," *Review of Scientific Instruments*, vol. 89, no. 7, 7 2018.

[24] A. Cabrera, A. Abusleme, J. dos Anjos, T. J. Bezerra, M. Bongrand, C. Bourgeois, D. Breton, C. Buck, J. Busto, E. Calvo, E. Chauveau, M. Chen, P. Chimenti, F. Dal Corso, G. De Conto, S. Dusini, G. Fiorentini, C. F. Martins, A. Givaudan, P. Govoni, B. Gramlich, M. Grassi, Y. Han, J. Hartnell, C. Hugon, S. Jiménez, H. de Kerret, A. Le Nevé, P. Loaiza, J. Maalmi, F. Mantovani, L. Manzanillas, C. Marquet, J. Martino, D. Navas-Nicolás, H. Nunokawa, M. Obolensky, J. P. Ochoa-Ricoux, G. Ortona, C. Palomares, F. Pessina, A. Pin, J. C. Porter, M. S. Pravikoff, M. Roche, B. Roskovec, N. Roy, C. Santos, S. Schoppmann, A. Serafini, L. Simard, M. Sisti, L. Stanco, V. Strati, J. S. Stutzmann, F. Suekane, A. Verdugo, B. Viaud, C. Volpe, C. Vrignon, S. Wagner, and F. Yermia, "Neutrino physics with an opaque detector," *Communications Physics*, vol. 4, no. 1, pp. 1–9, 2021.

[25] "LiquidO Collaboration," 2023. [Online]. Available: https://liquido.ijclab.in2p3.fr/

[26] A. Cabrera, A. Abusleme, J. dos Anjosy, T. J. Bezerra, M. Bongrand, C. Bourgeois, D. Breton, C. Buck, J. Busto, E. Calvo, E. Chauveau, M. Chen, P. Chimenti, F. Dal Corso, G. De Conto, S. Dusini, G. Fiorentini, C. Frigerio Martins, A. Givaudan, P. Govoni, B. Gramlich, M. Grassi, Y. Han, J. Hartnell, C. Hugon, S. Jimenez, H. de Kerretz, A. Le Neve, P. Loaiza, J. Maalmi, F. Mantovani, L. Manzanillas, C. Marquet, J. Martino, D. Navas, H. Nunokawa, M. Obolensky, J. P. Ochoa-Ricoux, G. Ortona, C. Palomares, F. Pessina, A. Pin, M. S. Pravikoff, M. Roche, B. Roskovec, N. Roy, C. Santos, A. Serani, L. Simard, M. Sisti, L. Stanco, V. Strati, J. S. Stutzmann, F. Suekane, A. Verdugo, B. Viaud, C. Volpe, C. Vrignon, S. Wagner, and F. Yermia, "Neutrino physics with an opaque detector," *arXiv*, 2019.

[27] C. Buck, B. Gramlich, and S. Schoppmann, "Novel opaque scintillator for neutrino detection," *Journal of Instrumentation*, vol. 14, no. 11, 2019.

[28] A. S. Wilhelm and I. Jovanovic, "Gamma-ray spectroscopy using angular distribution of Compton scattering," *Nuclear Instruments and Methods in Physics Research, Section A: Accelerators, Spectrometers, Detectors and Associated Equipment*, vol. 1031, 5 2022.

[29] E. Esarey, C. B. Schroeder, and W. P. Leemans, "Physics of laser-driven plasma-based electron accelerators," *Reviews of Modern Physics*, vol. 81, no. 3, pp. 1229–1285, 2009.

[30] F. Albert and A. G. Thomas, "Applications of laser wakefield accelerator-based light sources," *Plasma Physics and Controlled Fusion*, vol. 58, no. 10, 2016.

[31] F. V. Hartemann, D. J. Gibson, W. J. Brown, A. Rousse, K. T. Phuoc, V. Mallka, J. Faure, and A. Pukhov, "Compton scattering x-ray sources driven by laser wakefield acceleration," *Physical Review Special Topics - Accelerators and Beams*, vol. 10, no. 1, p. 11301, 1 2007. [Online]. Available: https://link.aps.org/doi/10.1103/PhysRevSTAB.10.011301

[32] S. Banerjee, S. Chen, N. Powers, D. Haden, C. Liu, G. Golovin, J. Zhang, B. Zhao, S. Clarke, S. Pozzi, J. Silano, H. Karwowski, and D. Umstadter, "Compact source of narrowband and tunable X-rays for radiography," *Nuclear Instruments and Methods in Physics Research, Section B: Beam Interactions with Materials and Atoms*, vol. 350, pp. 106–111, 2015. [Online]. Available: http://www.sciencedirect.com/science/article/pii/S0168583X15000282

[33] S. Chen, G. Golovin, C. Miller, D. Haden, S. Banerjee, P. Zhang, C. Liu, J. Zhang, B. Zhao, S. Clarke, S. Pozzi, and D. Umstadter, "Shielded radiography with a laser-driven MeV-energy X-ray source," *Nuclear Instruments and Methods in Physics Research, Section B: Beam Interactions with Materials and Atoms*, vol. 366, pp. 217–223, 2016. [Online]. Available: http://www.sciencedirect.com/science/article/pii/S0168583X15011258

[34] A. Hannasch, A. Laso Garcia, M. LaBerge, R. Zgadzaj, A. Köhler, J. P. Couperus Cabadağ, O. Zarini, T. Kurz, A. Ferrari, M. Molodtsova, L. Naumann, T. E. Cowan, U. Schramm, A. Irman, and M. C. Downer, "Compact spectroscopy of keV to MeV X-rays from a laser wakefield accelerator," *Scientific Reports*, vol. 11, no. 1, pp. 1–17, 2021. [Online]. Available: https://doi.org/10.1038/s41598-021-93689-5

[35] D. J. Corvan, G. Sarri, and M. Zepf, "Design of a compact spectrometer for high-flux MeV gamma-ray beams," *Review of Scientific Instruments*, vol. 85, no. 6, p. 65119, 2014. [Online]. Available: http://dx.doi.org/10.1063/1.4884643

[36] J. M. Cole, K. T. Behm, E. Gerstmayr, T. G. Blackburn, J. C. Wood, C. D. Baird, M. J. Duff, C. Harvey, A. Ilderton, A. S. Joglekar, K. Krushelnick, S. Kuschel, M. Marklund, P. McKenna, C. D. Murphy, K. Poder, C. P. Ridgers, G. M. Samarin, G. Sarri, D. R. Symes, A. G. Thomas, J. Warwick, M. Zepf, Z. Najmudin, and S. P. Mangles, "Experimental Evidence of Radiation Reaction in the Collision of a High-Intensity Laser Pulse with a Laser-Wakefield Accelerated Electron Beam," *Physical Review X*, vol. 8, no. 1, p. 011020, 2 2018. [Online]. Available: https://link.aps.org/doi/10.1103/PhysRevX.8.011020

[37] K. T. Behm, J. M. Cole, A. S. Joglekar, E. Gerstmayr, J. C. Wood, C. D. Baird, T. G. Blackburn, M. Duff, C. Harvey, A. Ilderton, S. Kuschel, S. P. Mangles, M. Marklund, P. McKenna, C. D. Murphy, Z. Najmudin, K. Poder, C. P. Ridgers, G. Sarri, G. M. Samarin, D. Symes, J. Warwick, M. Zepf, K. Krushelnick, and A. G. Thomas, "A spectrometer for ultrashort gamma-ray pulses with photon energies greater than 10 MeV," *Review of Scientific Instruments*, vol. 89, no. 11, 2018. [Online]. Available: http://dx.doi.org/10.1063/1.5056248

[38] S. Cipiccia, S. M. Wiggins, D. Maneuski, E. Brunetti, G. Vieux, X. Yang, R. C. Issac, G. H. Welsh, M. Anania, M. R. Islam, B. Ersfeld, R. Montgomery, G. Smith, M. Hoek, D. J. Hamilton, N. R. Lemos, D. R. Symes, P. P. Rajeev, V. O. Shea, J. M. Dias, and D. A. Jaroszynski, "Compton scattering for spectroscopic detection of ultra-fast, high flux, broad energy range X-rays," *Review of Scientific Instruments*, vol. 84, no. 11, 2013.

[39] O. Klein and T. Nishina, "Über die Streuung von Strahlung durch freie Elektronen nach der neuen relativistischen Quantendynamik von Dirac," *Zeitschrift für Physik*, vol. 52, no. 11-12, pp. 853–868, 11 1929.

[40] P. C. Hansen, "The discrete picard condition for discrete ill-posed problems," *BIT*, 1990.

[41] ——, "Regularization Tools version 4.0 for Matlab 7.3," *Numerical Algorithms*, vol. 46, no. 2, pp. 189–194, 10 2007. [Online]. Available: https://doi.org/10.1007/s11075-007-9136-9

[42] ——, "Truncated Singular Value Decomposition Solutions to Discrete Ill-Posed Problems with Ill-Determined Numerical Rank," *SIAM Journal on Scientific and Statistical Computing*, vol. 11, no. 3, pp. 503–518, 1990. [Online]. Available: http://proxy.lib.umich.edu/login?url=https://search.proquest.com/docview/921803045?accountid=14667

[43] G. H. Golub, P. C. Hansen, and D. P. O'Leary, "Tikhonov regularization and total least squares," *SIAM Journal on Matrix Analysis and Applications*, vol. 21, no. 1, pp. 185–194, 1999. [Online]. Available: http://proxy.lib.umich.edu/login?url=https://search.proquest.com/docview/923739981?accountid=14667

[44] A. P. Dempster, N. M. Laird, and D. B. Rubin, " Maximum Likelihood from Incomplete Data Via the EM Algorithm ," *Journal of the Royal Statistical Society: Series B (Methodological)*, vol. 39, no. 1, pp. 1–22, 1977. [Online]. Available: http://www.jstor.org/stable/2984875

[45] H. Q. Zhu, H. Z. Shu, J. Zhou, and L. M. Luo, "Maximum likelihood algorithm for PET image reconstruction based on fuzzy random variable," in *Annual International Conference of the IEEE Engineering in Medicine and Biology - Proceedings*, vol. 26 II, 9 2004, pp. 1361–1364.

[46] S. Agostinelli, J. Allison, K. Amako, J. Apostolakis, H. Araujo, P. Arce, M. Asai, D. Axen, S. Banerjee, G. Barrand, F. Behner, L. Bellagamba, J. Boudreau, L. Broglia, A. Brunengo, H. Burkhardt, S. Chauvie, J. Chuma, R. Chytracek, G. Cooperman, G. Cosmo, P. Degtyarenko, A. Dell'Acqua, G. Depaola, D. Dietrich, R. Enami, A. Feliciello, C. Ferguson, H. Fesefeldt, G. Folger, F. Foppiano, A. Forti, S. Garelli, S. Giani, R. Giannitrapani, D. Gibin, J. J. Gomez Cadenas, I. Gonzalez, G. Gracia Abril, G. Greeniaus, W. Greiner, V. Grichine, A. Grossheim, S. Guatelli, P. Gumplinger, R. Hamatsu, K. Hashimoto, H. Hasui, A. Heikkinen, A. Howard, V. Ivanchenko, A. Johnson, F. W. Jones, J. Kallenbach, N. Kanaya, M. Kawabata, Y. Kawabata, M. Kawaguti, S. Kelner, P. Kent, A. Kimura, T. Kodama, R. Kokoulin, M. Kossov, H. Kurashige, E. Lamanna, T. Lampen, V. Lara, V. Lefebure, F. Lei, M. Liendl, W. Lockman, F. Longo, S. Magni, M. Maire, E. Medernach, K. Minamimoto, P. Mora de Freitas, Y. Morita, K. Murakami, M. Nagamatu, R. Nartallo, P. Nieminen, T. Nishimura, K. Ohtsubo, M. Okamura, S. O'Neale, Y. Oohata, K. Paech, J. Perl, A. Pfeiffer, M. G. Pia, F. Ranjard, A. Rybin, S. Sadilov, E. di Salvo, G. Santin, T. Sasaki, N. Savvas, Y. Sawada, S. Scherer, S. Sei, V. Sirotenko, D. Smith, N. Starkov, H. Stoecker, J. Sulkimo, M. Takahata, S. Tanaka, E. Tcherniaev, E. Safai Tehrani, M. Tropeano, P. Truscott, H. Uno, L. Urban,

P. Urban, M. Verderi, A. Walkden, W. Wander, H. Weber, J. P. Wellisch, T. Wenaus, D. C. Williams, D. Wright, T. Yamada, H. Yoshida, and D. Zschiesche, "GEANT4 - A simulation toolkit," *Nuclear Instruments and Methods in Physics Research, Section A: Accelerators, Spectrometers, Detectors and Associated Equipment*, vol. 506, no. 3, pp. 250–303, 7 2003. [Online]. Available: http://www.sciencedirect.com/science/article/pii/S0168900203013688https://linkinghub.elsevier.com/retrieve/pii/S0168900203013688

[47] P. L. Reeder and D. C. Stromswold, "Performance of Large NaI(Tl) Gamma-Ray Detectors Over Temperature -50°C to +60°C," *Pacific Northwest National Laboratory*, vol. 14735, no. June, pp. 1–46, 2004.

[48] F. Pino, L. Stevanato, D. Cester, G. Nebbia, L. Sajo-Bohus, and G. Viesti, "The light output and the detection efficiency of the liquid scintillator EJ-309," *Applied Radiation and Isotopes*, vol. 89, pp. 79–84, 2014. [Online]. Available: http://www.sciencedirect.com/science/article/pii/S0969804314000682

[49] R. Kuroda, H. Toyokawa, M. Yasumoto, H. Ikeura-Sekiguchi, M. Koike, K. Yamada, T. Yanagida, T. Nakajyo, F. Sakai, and K. Mori, "Quasi-monochromatic hard X-ray source via laser Compton scattering and its application," *Nuclear Instruments and Methods in Physics Research, Section A: Accelerators, Spectrometers, Detectors and Associated Equipment*, vol. 637, no. 1 SUPPL., pp. S183–S186, 2011. [Online]. Available: http://dx.doi.org/10.1016/j.nima.2010.04.001

[50] K. Ta Phuoc, S. Corde, C. Thaury, V. Malka, A. Tafzi, J. P. Goddet, R. C. Shah, S. Sebban, and A. Rousse, "All-optical Compton gamma-ray source," *Nature Photonics*, vol. 6, no. 5, pp. 308–311, 2012.

[51] F. Chollet and others, "Keras," 2015. [Online]. Available: https://github.com/fchollet/keras

[52] F. V. Hartemann, W. J. Brown, D. J. Gibson, S. G. Anderson, A. M. Tremaine, P. T. Springer, A. J. Wootton, E. P. Hartouni, and C. P. Barty, "High-energy scaling of Compton scattering light sources," *Physical Review Special Topics - Accelerators and Beams*, vol. 8, no. 10, pp. 1–28, 10 2005. [Online]. Available: https://link.aps.org/doi/10.1103/PhysRevSTAB.8.100702

[53] C. Knappe, J. Lindén, F. Abou Nada, M. Richter, and M. Aldén, "Investigation and compensation of the nonlinear response in photomultiplier tubes for quantitative single-shot measurements," *Review of Scientific Instruments*, vol. 83, no. 3, p. 34901, 2012. [Online]. Available: http://dx.doi.org/10.1063/1.3693618

[54] P. R. Menge, G. Gautier, A. Iltis, C. Rozsa, and V. Solovyev, "Performance of large lanthanum bromide scintillators," *Nuclear Instruments and Methods in Physics Research, Section A: Accelerators, Spectrometers, Detectors and Associated Equipment*, vol. 579, no. 1, pp. 6–10, 2007. [Online]. Available: http://www.sciencedirect.com/science/article/pii/S0168900207005591

[55] F. G. Quarati, A. Owens, P. Dorenbos, J. T. De Haas, G. Benzoni, N. Blasi, C. Boiano, S. Brambilla, F. Camera, R. Alba, G. Bellia, C. Maiolino, D. Santonocito, M. Ahmed, N. Brown, S. Stave, H. R. Weller, and Y. K. Wu, "High energy gamma-ray spectroscopy with LaBr3 scintillation detectors," *Nuclear Instruments and Methods in Physics Research, Section A: Accelerators, Spectrometers, Detectors and Associated Equipment*, vol. 629, no. 1, pp. 157–169, 2011. [Online]. Available: http://www.sciencedirect.com/science/article/pii/S0168900210024976

[56] D. B. Cassidy and A. P. Mills, "A fast detector for single-shot positron annihilation lifetime spectroscopy," *Nuclear Instruments and Methods in Physics Research, Section A: Accelerators, Spectrometers, Detectors and Associated Equipment*, vol. 580, no. 3, pp. 1338–1343, 10 2007. [Online]. Available: http://www.sciencedirect.com/science/article/pii/S0168900207013691https://linkinghub.elsevier.com/retrieve/pii/S0168900207013691

[57] F. Albert, S. G. Anderson, D. J. Gibson, C. A. Hagmann, M. S. Johnson, M. Messerly, V. Semenov, M. Y. Shverdin, B. Rusnak, A. M. Tremaine, F. V. Hartemann, C. W. Siders, D. P. McNabb, and C. P. Barty, "Characterization and applications of a tunable, laser-based, MeV-class Compton-scattering γ-ray source," *Physical Review Special Topics - Accelerators and Beams*, vol. 13, no. 7, pp. 1–13, 2010.

[58] S. L. Jacques and B. W. Pogue, "Tutorial on diffuse light transport," *Journal of Biomedical Optics*, vol. 13, no. 4, p. 041302, 2008.

[59] P. W. Anderson, "Absence of Diffusion in Certain Random Lattices," *Physical Review*, vol. 109, no. 5, pp. 1492–1505, 3 1958.

[60] F. Cottier, A. Cipris, R. Bachelard, and R. Kaiser, "Microscopic and Macroscopic Signatures of 3D Anderson Localization of Light," *Physical Review Letters*, vol. 123, no. 8, 8 2019.

[61] I. S. Saidi, S. L. Jacques, and F. K. Tittel, "Mie and Rayleigh modeling of visible-light scattering in neonatal skin," *Applied Optics*, vol. 34, no. 31, p. 7410, 11 1995.

[62] C. A. Bunge, R. Kruglov, and H. Poisel, "Rayleigh and Mie Scattering in polymer optical fibers," *Journal of Lightwave Technology*, vol. 24, no. 8, pp. 3137–3146, 8 2006.

[63] M. Li, Z. Guo, M. Yeh, Z. Wang, and S. Chen, "Separation of scintillation and Cherenkov lights in linear alkyl benzene," *Nuclear Instruments and Methods in Physics Research, Section A: Accelerators, Spectrometers, Detectors and Associated Equipment*, vol. 830, pp. 303–308, 9 2016.

[64] X. F. Ding, L. J. Wen, X. Zhou, Y. Y. Ding, X. C. Ye, L. Zhou, M. C. Liu, H. Cai, and J. Cao, "Measurement of the fluorescence quantum yield of bis-MSB," *Chinese Physics C*, vol. 39, no. 12, 12 2015.

[65] S. Dönmez, *Radiation Detection and Measurement*, 4th ed. Ann Arbor: John Wiley and Sons, Inc., 2017, vol. 3, no. 3.

[66] A. Artikov, V. Baranov, J. Budagov, M. Bulavin, D. Chokheli, Y. I. Davydov, V. Glagolev, Y. Kharzheev, V. Kolomoets, A. Simonenko, Z. Usubov, and I. Vasilyev, "Light yield and radiation hardness studies of scintillator strips with a filler," *Nuclear Instruments and Methods in Physics Research, Section A: Accelerators, Spectrometers, Detectors and Associated Equipment*, vol. 930, no. March, pp. 87–94, 2019. [Online]. Available: https://doi.org/10.1016/j.nima.2019.03.087

[67] "Neutron/Gamma PSD Liquid Scintillator EJ-301, EJ-309 Datasheet," p. 1, 2018. [Online]. Available: https://eljentechnology.com/images/products/data_sheets/EJ-301_EJ-309.pdf

[68] "Plastic Scintillating Fibers Datasheets," p. 3. [Online]. Available: http://kuraraypsf.jp/pdf/all.pdf

[69] "Kuraray Plastic Scintillating Fibers Datasheet," pp. 7–9, 2022. [Online]. Available: http://kuraraypsf.jp/pdf/all.pdf

[70] M. Herzkamp, "Simulation and Optimization of a Position Sensitive Scintillation Detector with Wavelength Shifting Fibers for Thermal Neutrons," Ph.D. dissertation, Aachen University, 9 2016. [Online]. Available: www.fz-juelich.de/zb

[71] A. P. Ivashkina, Y. G. Kudenko, O. V. Mineeva, and J. Imazatob, "Scintillation ring hodoscope with WLS fiber readout," *Nuclear Inst. and Methods in Physics Research, A*, vol. 394, pp. 321–331, 1997.

[72] S. Aota, T. Asakawa, K. Hara, E. Hayashi, S. Kim, K. Kondo, T. Kuwabara, S. Miyashita, H. Nakada, I. Nakano, Y. Seiya, K. Takikawa, H. Toyoda, T. Uchida, K. Yasuoka, M. Mishina, J. Iwai, M. Albrow, J. Freeman, and P. J. Limon, "A scintillating tile/fiber system for the CDF plug upgrade EM calorimeter," *Nuclear Inst. and Methods in Physics Research, A*, vol. 352, no. 3, pp. 557–568, 1995.

[73] J. D. Weiss, "Trapping efficiency of fluorescent optical fibers," *Optical Engineering*, vol. 54, no. 2, p. 027101, 2 2015.

[74] A. S. Wilhelm, G. Wendel, B. Collins, D. Cowen, and I. Jovanovic, "Evaluation of light collection from highly scattering media using wavelength-shifting fibers," *Nuclear Instruments and Methods in Physics Research Section A: Accelerators, Spectrometers, Detectors and Associated Equipment*, vol. 1049, p. 168085, 4 2023.

[75] N. Dogan, D. K. Wehe, and G. F. Knoll, "Multiple Compton scattering gamma ray imaging camera," *Nuclear Inst. and Methods in Physics Research, A*, vol. 299, no. 1-3, pp. 501–506, 12 1990.

[76] S. R. Klein, "IceCube: A cubic kilometer radiation detector," *IEEE Transactions on Nuclear Science*, vol. 56, no. 3, pp. 1141–1147, 6 2009.

[77] K. Weinfurther, J. Mattingly, E. Brubaker, J. Steele, M. Sweany, and J. Braverman, "Low light event reconstruction simulations for an optically segmented single volume scatter camera," in *2015 IEEE Nuclear Science Symposium and Medical Imaging Conference (NSS/MIC)*. IEEE, 10 2015, pp. 1–3.

[78] B. S. Wonsak, C. I. Hagner, D. A. Hellgartner, K. Loo, S. Lorenz, D. J. Meyhöfer, L. Oberauer, H. Rebber, W. H. Trzaska, and M. Wurm, "Topological track reconstruction in unsegmented, large-volume liquid scintillator detectors," *Journal of Instrumentation*, vol. 13, no. 07, p. P07005, 7 2018. [Online]. Available: https://iopscience.iop.org/article/10.1088/1748-0221/13/07/P07005https://iopscience.iop.org/article/10.1088/1748-0221/13/07/P07005/meta

[79] E. Kim, K. J. Hong, J. Y. Yeom, P. D. Olcott, and C. S. Levin, "Trends of data path topologies for data acquisition systems in positron emission tomography," *IEEE Transactions on Nuclear Science*, vol. 60, no. 5, pp. 3746–3757, 2013.

[80] M. Yeh, S. Hans, W. Beriguete, R. Rosero, L. Hu, R. L. Hahn, M. V. Diwan, D. E. Jaffe, S. H. Kettell, and L. Littenberg, "A new water-based liquid scintillator and potential applications," *Nuclear Instruments and Methods in Physics Research, Section A: Accelerators, Spectrometers, Detectors and Associated Equipment*, vol. 660, no. 1, pp. 51–56, 12 2011.

[81] J. Caravaca, B. J. Land, M. Yeh, and G. D. Orebi Gann, "Characterization of water-based liquid scintillator for Cherenkov and scintillation separation," *European Physical Journal C*, vol. 80, no. 9, 9 2020.

[82] S. Stocker, F. Foschum, P. Krauter, F. Bergmann, A. Hohmann, C. Scalfi Happ, and A. Kienle, "Broadband Optical Properties of Milk," *Applied Spectroscopy*, vol. 71, no. 5, pp. 951–962, 5 2017.

[83] A. Brunelli, G. Pojana, S. Callegaro, and A. Marcomini, "Agglomeration and sedimentation of titanium dioxide nanoparticles (n-TiO2) in synthetic and real waters," *Journal of Nanoparticle Research*, vol. 15, no. 6, 6 2013.

[84] P. D. Ninni, F. Martelli, and G. Zaccanti, "Intralipid: Towards a diffusive reference standard for optical tissue phantoms," *Physics in Medicine and Biology*, vol. 56, no. 2, 1 2011.

[85] I. Alekseev, M. Danilov, V. Rusinov, E. Samigullin, D. Svirida, and E. Tarkovsy, "The performance of a new Kuraray wavelength shifting fiber YS-2," *Journal of Instrumentation*, vol. 17, no. 1, pp. 2–10, 2022.

[86] E. H. Bellamy, G. Bellettini, J. Budagov, F. Cervelli, I. Chirikov-Zorin, M. Incagli, D. Lucchesi, C. Pagliarone, S. Tokar, and F. Zetti, "Absolute calibration and monitoring of a spectrometric channel using a photomultiplier," *Nuclear Inst. and Methods in Physics Research, A*, vol. 339, no. 3, pp. 468–476, 1994.

[87] P. Schober, C. Boer, and L. A. Schwarte, "Correlation Coefficients: Appropriate Use and Interpretation," *Anesthesia & Analgesia*, vol. 126, no. 5, pp. 1763–1768, 5 2018.

[88] R. B. Pahlka, G. Elpers, J. Huang, K. Lang, and M. Proga, "Spectral Characterization and Modeling of Wavelength-shifting Fibers," *arXiv*, 11 2019. [Online]. Available: http://arxiv.org/abs/1911.03790

[89] J. Cooper, R. Ray, and N. Grossman, "NOνA NuMI Off-Axis ν e Appearance Experiment Technical Design Report," Fermi National Accelerator Laboratory, Tech. Rep., 10 2007.

[90] "Hamamatsu H12700A Datasheet," 2019. [Online]. Available: https://www.hamamatsu.com/content/dam/hamamatsu-photonics/sites/documents/99_SALES_LIBRARY/etd/H12700_H14220_TPMH1379E.pdf

[91] T. Meinhold, J. P. Richters, L. Damerow, and M. M. Blanke, "Optical properties of reflection ground covers with potential for enhancing fruit colouration," *Biosystems Engineering*, vol. 107, no. 2, pp. 155–160, 2010.

[92] C. Urban and P. Schurtenberger, "Application of a new light scattering technique to avoid the inÑuence of dilution in light scattering experiments with milk," *Physical Chemistry Chemical Physics*, vol. 1, no. 17, pp. 3911–3915, 1999.

[93] S. D. Campbell, S. Menon, G. H. Rutherford, Q. Su, and R. Grobe, "Scaling of light scattering with density of scatterers," *Laser Physics*, vol. 17, no. 2, pp. 117–123, 2 2007.

[94] J. Qin and R. Lu, "Hyperspectral diffuse reflectance for determination of the optical properties of milk and fruit and vegetable juices," in *Optical Sensors and Sensing Systems for Natural Resources and Food Safety and Quality*, vol. 5996. SPIE, 11 2005, p. 59960Q.

[95] J. J. Duderstadt and L. J. Hamilton, *Nuclear Reactor Analysis*. New York: Wiley, 1976.

[96] D. Zwicker, "py-pde: A Python package for solving partial differential equations," *Journal of Open Source Software*, vol. 5, no. 48, p. 2158, 4 2020.

[97] J. G. Charney, R. FjÖrtoft, and J. V. Neumann, "Numerical Integration of the Barotropic Vorticity Equation," *Tellus*, vol. 2, no. 4, pp. 237–254, 1 1950.

[98] L. J. Bignell, D. Beznosko, M. V. Diwan, S. Hans, D. E. Jaffe, S. Kettell, R. Rosero, H. W. Themann, B. Viren, E. Worcester, M. Yeh, and C. Zhang, "Characterization and modeling of a Water-based Liquid Scintillator," *Journal of Instrumentation*, vol. 10, no. 12, 2015.

[99] M. Chung and S. Margulies, "Effects of light on scintillating fibers," in *Proceedings Volume 2007, Scintillating Fiber Technology and Applications*, E. J. Fenyves, Ed., 10 1993, pp. 41–48.

[100] X.-C. Ye, B.-X. Yu, X. Zhou, L. Zhao, Y.-Y. Ding, M.-C. Liu, X.-F. Ding, X. Zhang, Q.-L. Jie, L. Zhou, J. Fang, H.-T. Chen, W. Hu, S.-L. Niu, J.-Q. Yan, H. Zhao, and D.-J. Hong, "Preliminary study of light yield dependence on LAB liquid scintillator composition," *Chinese Physics C*, vol. 39, no. 9, p. 096003, 9 2015.

[101] M. Taniguchi and J. S. Lindsey, "Database of Absorption and Fluorescence Spectra of >300 Common Compounds for use in PhotochemCAD," *Photochemistry and Photobiology*, vol. 94, no. 2, pp. 290–327, 3 2018.

[102] E. Toson, M. Kobald, E. Cavanna, L. T. De Luca, G. Consolati, and H. K. Ciezki, "Feasibility Study of Paraffin-based Fuels for Hybrid Rocket Engine Applications," *International Journal of Energetic Materials and Chemical Propulsion*, vol. 13, no. 6, pp. 559–572, 2014.

[103] M. A. M. Neto and J. R. Barbosa, "Solubility, density and viscosity of mixtures of isobutane (R-600a) and a linear alkylbenzene lubricant oil," *Fluid Phase Equilibria*, vol. 292, no. 1-2, pp. 7–12, 5 2010.

[104] A. Bonhomme, C. Buck, B. Gramlich, and M. Raab, "Safe liquid scintillators for large scale detectors," *Journal of Instrumentation*, vol. 17, no. 11, p. P11025, 11 2022.

[105] T. Kesete, A. Storm, R. L. Hahn, and S. Seleem, "Solvent purification and fluor selection for gadolinium-loaded liquid scintillators," *U.S. Department of Energy Journal of Undergraduate Research*, vol. 7, pp. 43–47, 2007. [Online]. Available: https://www.osti.gov/biblio/1051825

[106] Y. Suzuki, "The Super-Kamiokande experiment," *European Physical Journal C*, vol. 79, no. 4, 4 2019.

[107] A. Li, "KamLAND-Zen 800 Status and Prospect with the Artificial Intelligence Powered Analysis," *Journal of Physics: Conference Series*, vol. 2156, no. 1, 12 2021.

[108] F. P. An, J. Z. Bai, A. B. Balantekin, H. R. Band, D. Beavis, W. Beriguete, M. Bishai, S. Blyth, R. L. Brown, I. Butorov, D. Cao, G. F. Cao, J. Cao, R. Carr, W. R. Cen, W. T. Chan, Y. L. Chan, J. F. Chang, L. C. Chang, Y. Chang, C. Chasman, H. Y. Chen, H. S. Chen, M. J. Chen, Q. Y. Chen, S. J. Chen, S. M. Chen, X. C. Chen, X. H. Chen, X. S. Chen, Y. X. Chen, Y. Chen, J. H. Cheng, J. Cheng, Y. P. Cheng, J. J. Cherwinka, S. Chidzik, K. Chow, M. C. Chu, J. P. Cummings, J. De Arcos, Z. Y. Deng, X. F. Ding, Y. Y. Ding, M. V. Diwan, L. Dong, J. Dove, E. Draeger, X. F. Du, D. A. Dwyer, W. R. Edwards, S. R. Ely, S. D. Fang, J. Y. Fu, Z. W. Fu, L. Q. Ge, V. Ghazikhanian, R. Gill, J. Goett, M. Gonchar, G. H. Gong, H. Gong, Y. A. Gornushkin, M. Grassi, L. S. Greenler, W. Q. Gu, M. Y. Guan, R. P. Guo, X. H. Guo, R. W. Hackenburg, R. L. Hahn, R. Han, S. Hans, M. He, Q. He, W. S. He, K. M. Heeger, Y. K. Heng, A. Higuera, P. Hinrichs, T. H. Ho, M. Hoff, Y. K. Hor, Y. B. Hsiung, B. Z. Hu, L. M. Hu, L. J. Hu, T. Hu, W. Hu, E. C. Huang, H. Z. Huang, H. X. Huang, P. W. Huang, X. Huang, X. T. Huang, P. Huber, G. Hussain, Z. Isvan, D. E. Jaffe, P. Jaffke, K. L. Jen, S. Jetter, X. P. Ji, X. L. Ji, H. J. Jiang, W. Q. Jiang, J. B. Jiao, R. A. Johnson, J. Joseph, L. Kang, S. H. Kettell, S. Kohn, M. Kramer, K. K. Kwan, M. W. Kwok, T. Kwok, C. Y. Lai, W. C. Lai, W. H. Lai, T. J. Langford, K. Lau, L. Lebanowski, J. Lee, M. K. Lee, R. T. Lei, R. Leitner, J. K. Leung, C. A. Lewis, B. Li, C. Li, D. J. Li, F. Li, G. S. Li, J. Li, N. Y. Li, Q. J. Li, S. F. Li, S. C. Li, W. D. Li, X. B. Li, X. N. Li, X. Q. Li, Y. Li, Y. F. Li, Z. B. Li, H. Liang, J. Liang, C. J. Lin, G. L. Lin, P. Y. Lin, S. X. Lin, S. K. Lin, Y. C. Lin, J. J. Ling, J. M. Link, L. Littenberg, B. R. Littlejohn, B. J. Liu, C. Liu, D. W. Liu, H. Liu, J. L. Liu, J. C. Liu, S. Liu, S. S. Liu, X. Liu, Y. B. Liu, C. Lu, H. Q. Lu, J. S. Lu, A. Luk, K. B. Luk, T. Luo, X. L. Luo, L. H. Ma, Q. M. Ma, X. Y. Ma, X. B. Ma, Y. Q. Ma, B. Mayes, K. T. McDonald, M. C. McFarlane, R. D. McKeown, Y. Meng, I. Mitchell, D. Mohapatra, J. Monari Kebwaro, J. E. Morgan, Y. Nakajima, J. Napolitano, D. Naumov, E. Naumova, C. Newsom, H. Y. Ngai, W. K. Ngai, Y. B. Nie, Z. Ning, J. P. Ochoa-Ricoux, A. Olshevskiy, A. Pagac, H. R. Pan, S. Patton, C. Pearson, V. Pec, J. C. Peng, L. E. Piilonen, L. Pinsky, C. S. Pun, F. Z. Qi, M. Qi, X. Qian, N. Raper, B. Ren, J. Ren, R. Rosero, B. Roskovec, X. C. Ruan, W. R. Sands, B. Seilhan, B. B. Shao, K. Shih, W. Y. Song, H. Steiner, P. Stoler, M. Stuart, G. X. Sun, J. L. Sun, N. Tagg, Y. H. Tam, H. K. Tanaka, W. Tang, X. Tang, D. Taychenachev, H. Themann, Y. Torun, S. Trentalange, O. Tsai, K. V. Tsang, R. H. Tsang, C. E. Tull, Y. C. Tung, N. Viaux, B. Viren, S. Virostek, V. Vorobel, C. H. Wang, L. S. Wang, L. Y. Wang, L. Z. Wang, M. Wang, N. Y. Wang, R. G. Wang, T. Wang, W. Wang, W. W. Wang, X. T. Wang, X. Wang, Y. F. Wang, Z. Wang, Z. Wang, Z. M. Wang, D. M. Webber, H. Y. Wei, Y. D. Wei, L. J. Wen, D. L. Wenman, K. Whisnant, C. G. White, L. Whitehead, C. A. Whitten, J. Wilhelmi, T. Wise, H. C. Wong,

H. L. Wong, J. Wong, S. C. Wong, E. Worcester, F. F. Wu, Q. Wu, D. M. Xia, J. K. Xia, S. T. Xiang, Q. Xiao, Z. Z. Xing, G. Xu, J. Y. Xu, J. L. Xu, J. Xu, W. Xu, Y. Xu, T. Xue, J. Yan, C. G. Yang, L. Yang, M. S. Yang, M. T. Yang, M. Ye, M. Yeh, Y. S. Yeh, K. Yip, B. L. Young, G. Y. Yu, Z. Y. Yu, S. Zeng, L. Zhan, C. Zhang, F. H. Zhang, H. H. Zhang, J. W. Zhang, K. Zhang, Q. X. Zhang, Q. M. Zhang, S. H. Zhang, X. T. Zhang, Y. C. Zhang, Y. H. Zhang, Y. M. Zhang, Y. X. Zhang, Y. M. Zhang, Z. J. Zhang, Z. Y. Zhang, Z. P. Zhang, J. Zhao, Q. W. Zhao, Y. F. Zhao, Y. B. Zhao, L. Zheng, W. L. Zhong, L. Zhou, N. Zhou, Z. Y. Zhou, H. L. Zhuang, S. Zimmerman, and J. H. Zou, "The detector system of the Daya Bay reactor neutrino experiment," *Nuclear Instruments and Methods in Physics Research, Section A: Accelerators, Spectrometers, Detectors and Associated Equipment*, vol. 811, pp. 133–161, 3 2016.

[109] M. Askins, Z. Bagdasarian, N. Barros, E. W. Beier, E. Blucher, R. Bonventre, E. Bourret, E. J. Callaghan, J. Caravaca, M. Diwan, S. T. Dye, J. Eisch, A. Elagin, T. Enqvist, V. Fischer, K. Frankiewicz, C. Grant, D. Guffanti, C. Hagner, A. Hallin, C. M. Jackson, R. Jiang, T. Kaptanoglu, J. R. Klein, Y. G. Kolomensky, C. Kraus, F. Krennrich, T. Kutter, T. Lachenmaier, B. Land, K. Lande, J. G. Learned, V. Lozza, L. Ludhova, M. Malek, S. Manecki, J. Maneira, J. Maricic, J. Martyn, A. Mastbaum, C. Mauger, F. Moretti, J. Napolitano, B. Naranjo, M. Nieslony, L. Oberauer, G. D. Orebi Gann, J. Ouellet, T. Pershing, S. T. Petcov, L. Pickard, R. Rosero, M. C. Sanchez, J. Sawatzki, S. H. Seo, M. Smiley, M. Smy, A. Stahl, H. Steiger, M. R. Stock, H. Sunej, R. Svoboda, E. Tiras, W. H. Trzaska, M. Tzanov, M. Vagins, C. Vilela, Z. Wang, J. Wang, M. Wetstein, M. J. Wilking, L. Winslow, P. Wittich, B. Wonsak, E. Worcester, M. Wurm, G. Yang, M. Yeh, E. D. Zimmerman, S. Zsoldos, and K. Zuber, "Theia: an advanced optical neutrino detector," *European Physical Journal C*, vol. 80, no. 5, 5 2020.

[110] T. Harvey and A. Enqvist, "Development of Prototype Simplified Neutron Scatter Camera for Nuclear Safeguards Applications," *EPJ Web of Conferences*, vol. 253, p. 07008, 11 2021.

[111] J. Manfredi, E. Adamek, J. A. Brown, E. Brubaker, B. Cabrera-Palmer, J. W. Cates, R. Dorrill, A. Druetzler, J. Elam, P. L. Feng, M. Folsom, A. Galindo-Tellez, B. L. Goldblum, P. Hausladen, N. Kaneshige, K. Keefe, T. A. Laplace, J. Learned, A. Mane, P. Marleau, J. Mattingly, M. Mishra, A. Moustafa, J. Nattress, K. Nishimura, J. Steele, M. Sweany, K. Weinfurther, and K.-P. Ziock, "The Single-Volume Scatter Camera," *Hard X-Ray, Gamma-Ray, and Neutron Detector Physics XXII*, p. 29, 8 2020.

[112] A. Cabrera, "LiquidO Opaque Neutrino Detection: New Results & Status," in *Neutrino 2022*. Neutrino 2022, 6 2022. [Online]. Available: https://doi.org/10.5281/zenodo.6697273

[113] A. Cabrera and LPET-OTech Collaboration, "Novel Positron Emission Tomography with Opaque Liquid Scintillator Detection Technology," in *IEEE Nuclear Science Symposium, Medical Imaging Conference and Room Temperature Semiconductor Detector Conference*, Milan, 11 2022.

[114] G. Hull, J. Lefrancois, N. Semkiv, A. Kotenko, S. Barsuk, M. H. Schune, D. Breton, and A. Cabrera, "Proof of Concept for a Scintillator Powder Calorimeter," in *2021 IEEE Nuclear Science Symposium and Medical Imaging Conference Record, NSS/MIC 2021 and 28th International Symposium on Room-Temperature Semiconductor Detectors, RTSD 2022*. Institute of Electrical and Electronics Engineers Inc., 2021.

[115] A. Cabrera, M. Chen, F. Mantovani, A. Serafini, V. Strati, J. Apilluelo, L. Asquith, J. Beney, T. Bezerra, M. Bongrand, C. Bourgeois, D. Breton, M. Briere, J. Busto, A. Cadiou, E. Calvo, V. Chaumat, E. Chauveau, B. Cattermole, P. Chimenti, C. Delafosse, H. de Kerret, S. Dusini, A. Earle, C. Frigerio-Martins, J. Galán, J. A. García, R. Gazzini, A. Gibson-Foster, A. Gallas, C. Girard-Carillo, W. Griffith, F. Haddad, J. Hartnell, A. Hourlier, G. Hull, I. G. Irastorza, L. Koch, P. Laniéce, J. Le Du, C. Lefebvre, F. Lefevre, F. Legrand, P. Loaiza, J. A.

Lock, G. Luzón, J. Maalmi, C. Marquet, M. Martínez, B. Mathon, L. Ménard, D. Navas-Nicolás, H. Nunokawa, J. Ochoa-Ricoux, M. Obolensky, C. Palomares, P. Pillot, J. Porter, M. Pravikoff, H. Ramarijaona, M. Roche, P. Rosier, B. Roskovec, M. Sarsa, S. Schoppmann, W. Shorrock, L. Simard, H. Steiger, D. Stocco, J. Stutzmann, F. Suekane, A. Tunc, M.-a. Verdier, A. Verdugo, B. Viaud, S. M. Wakely, A. Weber, and F. Yermia, "Probing Earth's Missing Potassium using the Unique Antimatter Signature of Geoneutrinos," *arXiv*, 2023.

[116] E. Bannister, "Investigating Light Losses in LiquidO Detectors: Understanding the Effect of Adhesives on Optical Fibres," Ph.D. dissertation, University of Sussex, Brighton and Hove, England, 5 2023.

[117] J. B. Cumming, S. Hans, and M. Yeh, "Improving light yield measurements for low-yield scintillators," *Nuclear Instruments and Methods in Physics Research, Section A: Accelerators, Spectrometers, Detectors and Associated Equipment*, vol. 925, pp. 1–5, 5 2019.

[118] C. Buck, B. Gramlich, M. Lindner, C. Roca, and S. Schoppmann, "Production and properties of the liquid scintillators used in the STEREO reactor neutrino experiment," *Journal of Instrumentation*, vol. 14, no. 1, 1 2019.

[119] S. Schoppman, "Review of Novel Approaches to Organic Liquid Scintillators in Neutrino Physics," *Symmetry 2023, Vol. 15, Page 11*, vol. 15, no. 1, p. 11, 12 2022.

[120] "EJ-309 Product Page - Eljen Technology." [Online]. Available: https://eljentechnology.com/products/liquid-scintillators

[121] A. P. Golhin and A. Strandlie, "Appearance evaluation of digital materials in material jetting," *Optics and Lasers in Engineering*, vol. 168, 9 2023.

[122] K. Kossert, "Measurement of wavelength-dependent refractive indices of liquid scintillation cocktails," *Applied Radiation and Isotopes*, vol. 82, pp. 382–388, 12 2013.

[123] M. S. Song, H. Y. Choi, J. H. Seong, and E. S. Kim, "Matching-index-of-refraction of transparent 3D printing models for flow visualization," *Nuclear Engineering and Design*, vol. 284, pp. 185–191, 4 2015.

[124] A. Lambora, K. Gupta, and K. Chopra, "Genetic Algorithm- A Literature Review," in *2019 International Conference on Machine Learning, Big Data, Cloud and Parallel Computing (COMITCon)*. IEEE, 2 2019, pp. 380–384.

[125] S. H. Song, K. K. Joo, S. H. So, and I. S. Yeo, "Feasibility study of a gadolinium-loaded DIN-based liquid scintillator," *Journal of the Korean Physical Society*, vol. 63, no. 5, pp. 970–974, 2013.

[126] L. Rayleigh, "On the transmission of light through an atmosphere containing small particles in suspension, and on the origin of the blue of the sky," *The London, Edinburgh, and Dublin Philosophical Magazine and Journal of Science*, vol. 47, no. 287, pp. 375–384, 4 1899.

[127] P. Eller, A. T. Fienberg, J. Weldert, G. Wendel, S. Böser, and D. Cowen, "A flexible event reconstruction based on machine learning and likelihood principles," *Nuclear Instruments and Methods in Physics Research Section A: Accelerators, Spectrometers, Detectors and Associated Equipment*, vol. 1048, p. 168011, 3 2023.

[128] O. Smirnov, "Note on intrinsic resolution in liquid organic scintillators," *Journal of Instrumentation*, vol. 18, no. 10, p. P10026, 10 2023.

[129] Boris Khoury (NKT Photonics), "Private correspondence," 2 2024.

[130] A. Kienle and M. S. Patterson, "Improved solutions of the steady-state and the time-resolved diffusion equations for reflectance from a semi-infinite turbid medium," *Journal of the Optical Society of America A*, vol. 14, no. 1, p. 246, 1 1997.

[131] H. J. Juttula, T. P. Kananen, and A. J. Mäkynen, "Instrument for measurement of optical parameters of turbid media by using diffuse reflectance of laser with oblique incidence angle," *IEEE Transactions on Instrumentation and Measurement*, vol. 63, no. 5, pp. 1301–1309, 2014.

[132] Y. I. Polupan, I. V. Lazarev, E. V. Martynenko, S. S. Minenko, O. A. Tarasenko, and V. A. Tarasov, "Peculiarities of the formation of scintillation response in organic materials with stochastic character of light propagation," *Problems of Atomic Science and Technology*, vol. 2023, no. 3, pp. 38–42, 2023.

[133] R. A. Taylor, P. E. Phelan, T. P. Otanicar, R. Adrian, and R. Prasher, "Nanofluid optical property characterization: towards efficient direct absorption solar collectors," *Nanoscale Research Letters*, vol. 6, no. 1, p. 225, 3 2011.

[134] I. Mutreja, N. Maalej, A. Kaushik, D. Kumar, and A. Raja, "High atomic number nanoparticles to enhance spectral CT imaging aspects," *Materials Advances*, vol. 4, no. 18, pp. 3967–3988, 2023.